UNIVERSITY OF OKLAHOMA

GRADUATE COLLEGE

Driving Mechanisms of Very Rapid Sea Ice Loss Events

A DISSERTATION

SUBMITTED TO THE GRADUATE FACULTY

in partial fulfillment of the requirements for the

Degree of

DOCTOR OF PHILOSOPHY

By

MADELINE CLARK FRANK
Norman, Oklahoma
2024

Downloaded from SHAREOK. Persistent Handle URL: https://hdl.handle.net/11244/340422

Driving Mechanisms of Very Rapid Sea Ice Loss Events

A DISSERTATION APPROVED FOR THE
SCHOOL OF METEOROLOGY

BY THE COMMITTEE CONSISTING OF

Dr. Steven Cavallo, Chair

Dr. David Parsons

Dr. Jason C. Furtado

Dr. Nikola Petrov

© Copyright by MADELINE CLARK FRANK2024
All Rights Reserved.

Acknowledgments

First I would like to thank my advisor, Dr. Steven Cavallo, for his years of mentorship and support throughout my graduate education. I would also like to thank the other members of my committee, Dr. Parsons, Dr. Furtado, and Dr. Petrov, for their time and feedback on my research. Additionally, thanks go to the Office of Naval Research for support of this research under ONR grant N00014-18-1-2223. Finally I would like to thank my friends and family for their continued support over the years, especially my husband, Liam, and daughter, Hanna, who have listened to me talk about sea ice more than any lawyer or toddler should ever have to. I love you both so much.

Table of Contents

Acknowledgments iv

List of Tables vii

List of Figures ix

Abstract xxvi

1 Introduction 1
- 1.1 Motivation . . . 1
- 1.2 Background . . . 2
  - 1.2.1 Sea Ice . . . 2
    - 1.2.1.1 Sea Ice Trends . . . 6
    - 1.2.1.2 Sea Ice In Global Climate Models . . . 7
    - 1.2.1.3 Observations . . . 8
  - 1.2.2 Arctic Cyclones . . . 9
  - 1.2.3 Tropopause Polar Vortices . . . 13
  - 1.2.4 Atmospheric and Ocean Drivers of Sea Ice Loss . . . 14
    - 1.2.4.1 Cyclone Interactions . . . 14

2 Data and Methods 17
- 2.1 Comparison of Arctic sea ice and cyclone properties between CESM2 LENS, observations, and ERA5 . . . 17
  - 2.1.1 CESM2 LENS Ensemble Member . . . 17
  - 2.1.2 Identifying VRILEs . . . 18
  - 2.1.3 CESM2 Reforecasts . . . 20
  - 2.1.4 Cyclone Tracker . . . 22
- 2.2 Statistical Analysis of Proposed VRILE Drivers . . . 22
  - 2.2.1 Multivariate Empirical Orthogonal Functions . . . 24
- 2.3 Finite Element Analysis Model . . . 26

3 Comparison of Arctic sea ice and cyclone properties between CESM2 LENS, observations, and ERA5 34
- 3.1 Sea ice properties . . . 34
- 3.2 VRILEs . . . 37
- 3.3 CESM2 Reforecast VRILE Case Studies . . . 39
  - 3.3.1 3 July 2007 VRILE . . . 40
  - 3.3.2 11 December 2011 VRILE . . . 41
  - 3.3.3 9 August 2012 VRILE . . . 42

3.3.4 23 December 2016 VRILE 43
3.4 Cyclone Properties 45
3.5 Summary 47

4 Statistical Analysis of Proposed VRILE Drivers 68
4.1 Root Mean Square Covariance 68
4.2 Multivariate EOF Analysis of Individual Atmospheric and Ocean Fields . . 69
4.2.0.1 Pacific Region JJA 71
4.2.0.2 Atlantic Region JJA 73
4.2.0.3 Pacific Region DJF 75
4.2.0.4 Atlantic Region DJF 78
4.3 Combined Analysis 80
4.4 Conclusions 82

5 One Dimensional Model 106

6 Conclusions 119

Reference List 123

List of Tables

2.1 Date and region of VRILE cases and initialization date for CESM2 S2S reforecasts. 21

2.2 Standard values used in one dimensional FEA model along with citations. These are the values used in each experiment unless explicitly stated otherwise. 31

2.3 Table of values for each variable in sea ice-ocean wave experiments. Experiment one is the baseline. 32

3.1 Correlation between seasonal mean NAO indices and sea ice extent between NSIDC and CESM2 LENS. For the first two rows, the NAO index is from NOAA's Climate Prediction Center (Van den Dool et al. 2000) and for the bottom two rows the NAO index is calculated from CESM2 LENS (Phillips et al. 2014). Indicated time offsets are for sea ice extent relative to the NAO. 37

4.1 Table of RMSC values for significant height of wind waves, surface mean latent heat flux, and 2-m temperature. 70

5.1 Values used to calculate $F_{drag}/F_{buoyancy}$ for different sea ice and ocean wave properties. The far right column shows the calculated ratio and is shaded in red if the ratio indicates that the sea ice will not fracture, green if the sea ice will fracture, and light green if the ratio is indeterminate but the corresponding experiment in Table 2.3 indicates sea ice fracture. There were no cases where the ratio is indeterminate but the corresponding experiment indicated no fracture. 111

List of Figures

1.1 Winter surface pressure anomalies associated with the strong positive and negative Arctic Oscillation) AO indices. Image comes NOAA Climate.gov and is based on data from the Physical Sciences Lab (Lindsey 2009). 4

1.2 Schematic of the positive and negative phases of the North Atlantic Oscillation (NAO). Image is from NOAA Climate.gov (Lindsey and Dahlman 2009). 5

1.3 Figure 2 from Valkonen et al. (2021). The seasonal average cyclone count for 1979–2015 calculated over 150 × 150 km grid boxes. Panels (a–c) show results for the cold season, and (d–f) for the warm season. The last row shows the difference between cold and the warm seasons. First column (a, d, and g) shows results for ERA-I data, the second column (b, e, and h) for ERA5 data, and the last column (c, f, and i) for CFSR. Statistically significant differences are shown by the stippling. 11

2.1 September (a) and March (b) average sea ice extent for CESM2 LENS (pink) and NSIDC (blue). CESM2 LENS data is from 1900-2020 and NSIDC data from 1980-2020. 19

2.2 Simplified diagram of a one dimensional, dynamic sea ice and ocean wave model. This shows three ice floes of length L and depth h. Point A represents the boundary between the MIZ and solid ice pack, modeled as a fixed boundary. Points B and C are the boundaries between the floes. Point D is the location where the MIZ gives way to open ocean. Each floe is supported at its center and edges by a spring mimicking the buoyancy force, with the exception of the fixed boundary at A. 33

3.1 Monthly average sea ice extent for CESM2 LENS (pink) and NSIDC (blue). Mean values are plotted with a solid line. The year with the minimum September extent are plotted as the dotted lines. Shading indicates the inner quartile range. The NSIDC data in a and b is from 1980-2022 while a uses CESM2 LENS data from 1960-2000 and b shows 1910-1950. 48

3.2 September minimum and March maximum sea ice extent for CESM2 LENS (blue) and NSIDC (pink). In a and b, CESM2 LENS data is from 1910-1950 and from 1960-2000 in b and d. NSIDC data is from 1980-2020 in both and CESM2 LENS data has been plotted against the same date range as the NSIDC data for ease of comparison. The black lines show the linear trend in each dataset with their associated r value and slope displayed inline. 49

3.3 Normalized power as a function of period of the daily change in sea ice extent in NSIDC (a-b) and CESM2 LENS (c-d). The power spectrum is plotted in black, the red noise spectrum in red, and the 95% significance level in green. Panels (a) and (c) show the power spectrum out to 365 days while panels (b) and (d) are limited to shorter timescales. 50

3.4 Composite mean of seasonal mean mslp of the five highest and lowest September sea ice minima with respect to the climate trend in CESM2 LENS. The top panel uses data from model years 1910-1950 and the bottom is for model years 1960-2000. In both panels, the left most column is January, February, and March (JFM), the middle column March, April, and May (MAM) and the right column for June, July, and August (JJA). 51

3.5 Standard deviation of monthly average sea ice concentration in CESM2 LENS and NSIDC. Panels (a-c) are the June, July, and August monthly sea ice concentration standard deviations in CESM2 LENS data from 1960-2000 respectively. Panels (d-f) show the June, July, and August sea ice concentration standard deviations in NSIDC data. 52

3.6 VRILE size by year in NSIDC (pinks) and CESM2 (blues) for summer (jja) in a and c and winter (djf) in b and d. In years with multiple VRILEs, the sea ice losses are vertically stacked and each color represents a unique VRILE. Figures a and b use CESM2 data from 1960-2000 while c and d use 1910-1950. 53

3.7 Location of VRILEs in NSIDC and CESM2 LENS datasets. Panels (a) and (d) respectively show the location of summer (jja) and winter (djf) VRILEs in NSIDC data. Panels (b) and (e) respectively show the locations of summer (jja) and winter (djf) VRILES in CESM2 LENS data from 1960-2000. Panels (c) and (f) respectively show the locations of summer (jja) and winter (djf) VRILEs in CESM2 LENS data from 1910-1950. 54

3.8 Composite mean of mslp for summer (jja) VRILEs centered on VRILE location (a-c) and closest local minimum in mslp to the VRILE location (d-f). Panels (a) and (d) utilize ERA5 data and are based on VRILEs found in NSIDC sea ice extent. Additionally, in these panels potential temperature on the dynamic tropopause (2 PVU surface) is shown by the colorfill and stippling indicates statistical significance at $> 99\%$ in the mslp field. In panels b, c, e, and f, only mslp is shown in both the contours and colorfill. Units for all fields are standardized anomalies. Panels (b) and (e) are generated from CESM2 LENS data from 1960-2000 and panels (c) and (f) are generated from CESM2 LENS years 1910-1950. 55

3.9 Composite mean of mslp for winter (djf) VRILEs centered on VRILE location (a-c) and closest local minimum in mslp to the VRILE location (d-f). Panels (a) and (d) utilize ERA5 data and are based on VRILEs found in NSIDC sea ice extent. Additionally, in these panels potential temperature on the dynamic tropopause (2 PVU surface) is shown by the colorfill and stippling indicates statistical significance at $> 99\%$ in the mslp field. In panels b, c, e, and f, only mslp is shown in both the contours and colorfill. Units for all fields are standardized anomalies. Panels (b) and (e) are generated from CESM2 LENS data from 1960-2000 and panels (c) and (f) are generated from CESM2 LENS years 1910-1950. 56

3.10 Daily sea ice extent change of the ten member reforecasts used to analyze four VRILE cases. The day of the VRILE and the sea ice loss associated with it it marked on each plot with a black line. Panel (a) is for the VRILE that occurred on 3 July, 2007 and the reforecast initialized on 25 June, 2007. Panel (b) is for the VRILE that occurred on 11 December, 2011 and the reforecast initialized on 5 December, 2011. Panel (c) is for the VRILE that occurred on 9 August, 2012 and the reforecast initialized on 30 July, 2012. Panel (d) is for the VRILE that occurred on 23 December, 2016 and the reforecast initialized on 19 December, 2016. 57

3.11 Five day change in sea ice concentration (a, c) and five day mean in mslp and 10 meter winds (b, d) for the 3 July 2007 VRILE. The location of the VRILE is circled on each panel. Panel (a) shows the difference in NSIDC sea ice concentration between 3 July 2007 and 28 June 2007. Panel (b) is the average mslp and 10 m winds for the same time period as (a) using ERA5 data. Panel (c) shows the difference in CESM2 S2S sea ice concentration between 3 July 2007 and 28 June 2007 from the reforecast initialized on 25 June 2007. Panel (d) is the average mslp and 10-m wind from the same reforecast and time period as in (c). 58

3.12 Difference in sea ice concentration in CESM2 S2S and NSIDC for the 3 July 2007 VRILE. The VRILE location is circled in green in both panels. Positive (Negative) values, shown in red (blue), indicate too much (little) sea ice in CESM2 in comparison to NSIDC. Panel (a) shows the difference in sea ice concentration on the day the CESM2 S2S reforecast was initialized, 25 June 2007, and panel (b) shows the difference on the day of the VRILE, 3 July 2007. 59

3.13 Five day change in sea ice concentration (a, c) and five day mean in mslp and 10 meter winds (b, d) for the 11 December 2011 VRILE. The location of the VRILE is circled on each panel. Panel (a) shows the difference in NSIDC sea ice concentration between 11 December 2011 and 6 December 2011. Panel (b) is the average mslp and 10 m winds for the same time period as (a) using ERA5 data. Panel (c) shows the difference in CESM2 S2S sea ice concentration between 11 December 2011 and 6 December 2011 from the reforecast initialized on 5 December 2011. Panel (d) is the average mslp and 10-m wind from the same reforecast and time period as in (c). Panels (e) and (f) are as (c) and (d) except WACCM6 was used at the atmospheric component in CESM2. 60

3.14 Difference in sea ice concentration in CESM2 S2S and NSIDC for the 11 December 2011 VRILE. The VRILE location is circled in green in both panels. Positive (Negative) values, shown in red (blue), indicate too much (little) sea ice in CESM2 in comparison to NSIDC. Panel (a) shows the difference in sea ice concentration on the day the CESM2 S2S reforecast was initialized, 5 December 2011, and panel (b) shows the difference on the day of the VRILE, 11 December 2011. Panels (c) and (d) are as (a) and (b) except WACCM6 was used at the atmospheric component in CESM2. . 61

3.15 Five day change in sea ice concentration (a, c) and five day mean in mslp and 10 meter winds (b, d) for the 9 August 2012 VRILE. The location of the VRILE is circled on each panel. Panel (a) shows the difference in NSIDC sea ice concentration between 9 August 2012 and 4 August 2012. Panel (b) is the average mslp and 10 m winds for the same time period as (a) using ERA5 data. Panel (c) shows the difference in CESM2 S2S sea ice concentration between 9 August 2012 and 9 August 2012 from the reforecast initialized on 30 July 2012. Panel (d) is the average mslp and 10-m wind from the same reforecast and time period as in (c). Panels (e) and (f) are as (c) and (d) for the reforecast initialted on 6 August 2012. . . . 62

3.16 Difference in sea ice concentration in CESM2 S2S and NSIDC for the 9 August 2012 VRILE from the reforecasts initialized on 30 July 2012 and 6 August 2012. The VRILE location is circled in green in all four panels. Positive (Negative) values, shown in red (blue), indicate too much (little) sea ice in CESM2 in comparison to NSIDC. Panel (a) shows the difference in sea ice concentration on the day the CESM2 S2S reforecast was initialized, 30 July 2012, and panel (b) shows the difference on the day of the VRILE, 9 August 2012. Panel (c) shows the difference in sea ice concentration on the day the 6 August 2012 reforecast was initialized and panel (d) shows the difference on the day of the VRILE for that reforecast. 63

3.17 Five day change in sea ice concentration (a, c) and five day mean in mslp and 10 meter winds (b, d) for the 23 December 2016 VRILE. The location of the VRILE is circled on each panel. Panel (a) shows the difference in NSIDC sea ice concentration between 23 December 2016 and 18 December 2016. Panel (b) is the average mslp and 10 m winds for the same time period as (a) using ERA5 data. Panel (c) shows the difference in CESM2 S2S sea ice concentration between 23 December 2016 and 19 December 2016 from the reforecast initialized on 19 December 2016. Panel (d) is the average mslp and 10-m wind from the same reforecast and time period as in (c). Panels (e) and (f) are as (c) and (d) except WACCM6 was used at the atmospheric component in CESM2. 64

3.18 Difference in sea ice concentration in CESM2 S2S and NSIDC for the 23 December 2016 VRILE. The VRILE location is circled in green in both panels.Positive (Negative) values, shown in red (blue), indicate too much (little) sea ice in CESM2 in comparison to NSIDC. Panel (a) shows the difference in sea ice concentration on the day the CESM2 S2S reforecast was initialized, 19 December 2016, and panel (b) shows the difference on the day of the VRILE, 23 December 2016. Panels (c) and (d) are as (a) and (b) except WACCM6 was used at the atmospheric component in CESM2. . 65

3.19 Probability density functions (PDF) of surface cyclones in CESM2 LENS and ERA5 of cyclone lifetime (a), minimum mslp (b) and average radius (c). CESM2 LENS data is plotted in blue and ERA5 in red. Solid lines correspond to the PDF of all cyclones while dashed lines correspond to summer cyclones (jja) only. Per the KS test, all CESM2 LENS distributions are significantly different from their ERA5 counterparts with greater than 99.9% confidence. 66

3.20 Density map of normalized cyclone location counts in CESM2 LENS (a) and ERA5 (b) and the difference, CESM2 LENS - ERA5, between them (c). 66

3.21 Density maps of normalized cyclogenesis location counts in CESM2 LENS (a) and ERA5 (b) and the difference, CESM2 LENS - ERA5, between them (c). 67

3.22 Density maps of normalized cyclolysis counts in CESM2 LENS (a) and ERA5 (b) and the difference, CESM2 LENS - ERA5, between them (c). . . 67

4.1 Percent variance explained of each EOF for the Atlantic region. The top row (a-c) is for summer (jja) and the bottom row (d-f) is for the winter (djf). Panels a and d are for significant height of wind waves, b and e for surface mean latent heat flux, and c and f are for 2-m temperature. 75

4.2 Percent variance explained of each EOF for the Pacific region. The top row (a-c) is for summer (jja) and the bottom row (d-f) is for the winter (djf). Panels a and d are for significant height of wind waves, b and e for surface mean latent heat flux, and c and f are for 2-m temperature. 76

4.3 Normalized principal component timeseries 1-4 (a-d) projected onto daily change in sea ice concentration anomalies. The PCs are taken from the multivariate EOF of summer daily change in sea ice concentration and daily mean significant height of wind wave anomalies in the Pacific region. Reds indicate that the sea ice directly varies with sea ice and blues indicate indirect variation. 83

4.4 Diagram depicting an Arctic cyclone interacting with the Beaufort High and the resulting winds. The area of the winds would have higher than average ocean waves with sea ice gain at the arrow tip and loss behind it. . . 84

4.5 Schematic depicting the proposed mechanism for sea ice loss associated with negative latent heat fluxes in summer. Strong solar radiation from clear sky conditions leading to upward LH flux from melt ponds on sea ice. 85

4.6 Normalized principal component timeseries 1-4 (a-d) projected onto daily change in sea ice concentration anomalies. The PCs are taken from the multivariate EOF of summer daily change in sea ice concentration and daily mean surface latent heat flux anomalies in the Pacific region. Reds indicate that the sea ice directly varies with sea ice and blues indicate indirect variation. 86

4.7 Normalized principal component timeseries 1-4 (a-d) projected onto daily change in sea ice concentration anomalies. The PCs are taken from the multivariate EOF of summer daily change in sea ice concentration and daily mean 2-m temperature anomalies in the Pacific region. Reds indicate that the sea ice directly varies with sea ice and blues indicate indirect variation. . 87

4.8 Diagram depicting a proposed mechanism for how warm temperatures could be associated with sea ice gain via transport. The warm temperatures in the Bering Sea could be the warm sector of a surface cyclone. The winds associated with this cyclone then draws sea ice into the Bering Sea. 88

4.9 Normalized principal component timeseries 1-4 (a-d) projected onto daily change in sea ice concentration anomalies. The PCs are taken from the multivariate EOF of summer daily change in sea ice concentration and daily mean significant height of wind wave anomalies in the Atlantic region. Reds indicate that the sea ice directly varies with sea ice and blues indicate indirect variation. 89

4.10 Normalized principal component timeseries 1-4 (a-d) projected onto daily change in sea ice concentration anomalies. The PCs are taken from the multivariate EOF of summer daily change in sea ice concentration and daily mean surface latent heat flux anomalies in the Atlantic region. Reds indicate that the sea ice directly varies with sea ice and blues indicate indirect variation. 90

4.11 Normalized principal component timeseries 1-4 (a-d) projected onto daily change in sea ice concentration anomalies. The PCs are taken from the multivariate EOF of summer daily change in sea ice concentration and daily mean 2-m temperature anomalies in the Atlantic region. Reds indicate that the sea ice directly varies with sea ice and blues indicate indirect variation. . 91

4.12 Normalized principal component timeseries 1-4 (a-d) projected onto daily change in sea ice concentration anomalies. The PCs are taken from the multivariate EOF of winter daily change in sea ice concentration and daily mean significant height of wind wave anomalies in the pacific region. Reds indicate that the sea ice directly varies with sea ice and blues indicate indirect variation. 92

4.13 Normalized principal component timeseries 1-4 (a-d) projected onto daily change in sea ice concentration anomalies. The PCs are taken from the multivariate EOF of winter daily change in sea ice concentration and daily mean of mean surface latent heat flux anomalies in the pacific region. Reds indicate that the sea ice directly varies with sea ice and blues indicate indirect variation. 93

4.14 Normalized principal component timeseries 1-4 (a-d) projected onto daily change in sea ice concentration anomalies. The PCs are taken from the multivariate EOF of winter daily change in sea ice concentration and daily mean 2-m temperature anomalies in the pacific region. Reds indicate that the sea ice directly varies with sea ice and blues indicate indirect variation. . 94

4.15 Schematic depicting the proposed mechanism for sea ice loss associated with negative latent heat fluxes in winter. In the winter, clear skies are not associated with increased solar radiation but there are still upward LH fluxes over regions of open ocean. The difference in temperature between the open ocean and sea ice is a baroclinic zone that can lead to increased storminess. Those storms can then further break up the sea ice through both winds and LH. 95

4.16 Composite difference of winter (djf) sea ice concentration for high versus low sea ice years (a). Standard deviation of winter (djf) sea ice concentration (b). 96

4.17 Normalized principal component timeseries 1-4 (a-d) projected onto daily change in sea ice concentration anomalies. The PCs are taken from the multivariate EOF of winter daily change in sea ice concentration and daily mean significant height of wind wave anomalies in the Atlantic region. Reds indicate that the sea ice directly varies with sea ice and blues indicate indirect variation. 97

4.18 Normalized principal component timeseries 1-4 (a-d) projected onto daily change in sea ice concentration anomalies. The PCs are taken from the multivariate EOF of winter daily change in sea ice concentration and daily mean of mean surface latent heat flux anomalies in the Atlantic region. Reds indicate that the sea ice directly varies with sea ice and blues indicate indirect variation. 98

4.19 Normalized principal component timeseries 1-4 (a-d) projected onto daily change in sea ice concentration anomalies. The PCs are taken from the multivariate EOF of winter daily change in sea ice concentration and daily mean 2-m temperature anomalies in the Atlantic region. Reds indicate that the sea ice directly varies with sea ice and blues indicate indirect variation. . 99

4.20 Normalized principal component timeseries 1-4 (a-d) projected onto daily change in sea ice concentration anomalies. The PCs are taken from the multivariate EOF of summer daily change in sea ice concentration, daily mean 2-m temperature anomalies, daily mean significant height of wind wave anomalies, and daily mean surface latent heat flux in the Pacific region. Reds indicate that the sea ice directly varies with sea ice and blues indicate indirect variation. 100

4.21 Normalized principal component timeseries 1-4 (a-d) projected onto daily change in sea ice concentration anomalies. The PCs are taken from the multivariate EOF of summer daily change in sea ice concentration, daily mean 2-m temperature anomalies, daily mean significant height of wind wave anomalies, and daily mean surface latent heat flux in the Atlantic region. Reds indicate that the sea ice directly varies with sea ice and blues indicate indirect variation. 101

4.22 Normalized principal component timeseries 1-4 (a-d) projected onto daily change in sea ice concentration anomalies. The PCs are taken from the multivariate EOF of winter daily change in sea ice concentration, daily mean 2-m temperature anomalies, daily mean significant height of wind wave anomalies, and daily mean surface latent heat flux in the Pacific region. Reds indicate that the sea ice directly varies with sea ice and blues indicate indirect variation. 102

4.23 Normalized principal component timeseries 1-4 (a-d) projected onto daily change in sea ice concentration anomalies. The PCs are taken from the multivariate EOF of winter daily change in sea ice concentration, daily mean 2-m temperature anomalies, daily mean significant height of wind wave anomalies, and daily mean surface latent heat flux in the Atlantic region. Reds indicate that the sea ice directly varies with sea ice and blues indicate indirect variation. 103

4.24 Percent variance explained versus mode of variability for combined multivariate EOFs by season and region. Error bars are calculated as North et al. (1982) 104

4.25 Normalized principal component timeseries 1 and 2 projected onto daily change in sea ice concentration anomalies in the Pacific (a and b) and Atlantic (c and d) regions. The PCs are taken from the multivariate EOF of winter daily change in sea ice concentration, daily mean significant height of wind wave anomalies, and daily mean surface latent heat flux. Reds indicate that the sea ice directly varies with sea ice and blues indicate indirect variation. 105

5.1 Displacement of sea ice floes from the one dimensional sea ice model forced by a single ocean wave. The displacement results from each time step (a) is plotted in black with the time of largest displacement highlighted. Locations where the shear force exceeds the fracture threshold are marked by red x's. In (b), colors correspond to the time step. Locations where the shear force in $\hat{x}$ exceeds the ridging threshold are marked by arrowheads pointing in the direction the force is acting. The boundaries between sea ice floes are shown with vertical black lines. Both plots correspond to experiment 1 in Table 2.3. 112

5.2 Displacement of sea ice floes from the one dimensional sea ice model forced by a single ocean wave. The displacement results from each time step (a and c) is plotted in black with the time of largest displacement highlighted. Locations where the shear force exceeds the fracture threshold are marked by red x's. In (b) and (d), colors correspond to the time step. Locations where the shear force in $\hat{x}$ exceeds the ridging threshold are marked by arrowheads pointing in the direction the force is acting. The boundaries between sea ice floes are shown with vertical black lines. Plots (a) and (b) correspond to experiment 2 in Table 2.3, and plots (c) and (d) to experiment 3. 113

5.3 Displacement of sea ice floes from the one dimensional sea ice model forced by a single ocean wave. The displacement results from each time step (a) is plotted in black with the time of largest displacement highlighted. Locations where the shear force exceeds the fracture threshold are marked by red x's. In (b), colors correspond to the time step. Locations where the shear force in $\hat{x}$ exceeds the ridging threshold are marked by arrowheads pointing in the direction the force is acting. The boundaries between sea ice floes are shown with vertical black lines. Both plots correspond to experiment 4 in Table 2.3. 114

5.4 Displacement of sea ice floes from the one dimensional sea ice model forced by a single ocean wave. The displacement results from each time step (a, c, and e) is plotted in black with the time of largest displacement highlighted. Locations where the shear force exceeds the fracture threshold are marked by red x's. In (b), (d) and (f), colors correspond to the time step. Locations where the shear force in $\hat{x}$ exceeds the ridging threshold are marked by arrowheads pointing in the direction the force is acting. The boundaries between sea ice floes are shown with vertical black lines. Plots (a) and (b) correspond to experiment 5 in Table 2.3, plots (c) and (d) to experiment 6, and plots (e) and (f) to experiment 7. 115

5.5 Displacement of sea ice floes from the one dimensional sea ice model forced by a single ocean wave. The displacement results from each time step (a and c) is plotted in black with the time of largest displacement highlighted. Locations where the shear force exceeds the fracture threshold are marked by red x's. In (b) and (d), colors correspond to the time step. Locations where the shear force in $\hat{x}$ exceeds the ridging threshold are marked by arrowheads pointing in the direction the force is acting. The boundaries between sea ice floes are shown with vertical black lines. Plots (a) and (b) correspond to experiment 8 in Table 2.3, and plots (c) and (d) to experiment 9. 116

5.6 Displacement of sea ice floes from the one dimensional sea ice model forced by a single ocean wave. The displacement results from each time step (a) is plotted in black with the time of largest displacement highlighted. Locations where the shear force exceeds the fracture threshold are marked by red x's. In (b), colors correspond to the time step. Locations where the shear force in $\hat{x}$ exceeds the ridging threshold are marked by arrowheads pointing in the direction the force is acting. The boundaries between sea ice floes are shown with vertical black lines. Both plots correspond to experiment 10 in Table 2.3. 117

5.7 Displacement of sea ice floes from the one dimensional sea ice model forced by a single ocean wave. The displacement results from each time step (a and c) is plotted in black with the time of largest displacement highlighted. Locations where the shear force exceeds the fracture threshold are marked by red x's. In (b) and (d), colors correspond to the time step. Locations where the shear force in $\hat{x}$ exceeds the ridging threshold are marked by arrowheads pointing in the direction the force is acting. The boundaries between sea ice floes are shown with vertical black lines. Plots (a) and (b) correspond to experiment 11 in Table 2.3, and plots (c) and (d) to experiment 12. 118

6.1 Schematic depicting the proposed mechanisms for the formation of VRILEs. First, a surface cyclone and a high pressure region set up across the MIZ. The winds from the pressure gradient create a region of enhanced ocean waves and ocean vertical mixing. Additionally, the cyclone's warm sector represents a region of enhanced sensible heat fluxes. As the cyclone moves through the MIZ (2), the floes in the regions highlighted in (1) are reduced in size. This reduction make transport out of the MIZ by the cyclone's winds easier, resulting in the large sea ice loss in panel (3). The smaller floes can also be further melted by the cyclone's warm sector. 124

Abstract

Forecasting Arctic sea ice is a complex, open problem in polar science, exasperated by climate change and Arctic amplification. Climate models consistently under represent sea ice processes on subseasonal timescales which may contribute to the forecasting challenges. Very rapid sea ice loss events (VRILEs) are substantial sea ice loss events that occur on the timescale of days. There are three mechanisms proposed to cause VRILEs: heat transport by surface cyclones, wind driven ocean waves, and ocean heating from vertical mixing. We hypothesize that ocean waves play as much if not more of a role in causing VRILEs as atmospheric heat transport.

We approach this problem from three perspectives. First, a detailed comparison of sea ice properties in observations and the Community Earth System Model version two large ensemble (CESM2 LENS). Of note is that neither CESM2 or any other model couples ocean waves to sea ice. We find that model performance in this area is insufficient to study short term phenomena meaningfully. Next we take a statistical approach, utilizing multivariate EOFs to examine the relative importance of various atmospheric and ocean fields to subseasonal changes in sea ice concentration. In general, heating terms more strongly co-vary with sea ice concentration than ocean waves with seasonal difference in the importance of 2-m temperature anomalies. Finally we construct a one-dimensional, Finite Element Analysis model to study how effective ocean waves are at fracturing sea ice in the Marginal Ice Zone (MIZ). Ocean waves, particularly low frequency waves, are capable of fracturing large ice floes over a kilometer deep in the MIZ. Taken all together, we find that ocean waves likely play an causal role for VRILEs but one intertwined with the other mechanisms. That is, there is not a single most important factor but VRILEs are related to increased storminess caused by a surface cyclone interacting with a preexisting high pressure system that generated ocean waves and upwelling. They cyclone itself transports heat, especially in its warm sector, and its winds can drive sea ice both deeper into the central Arctic and out of the Arctic depending on the cyclone's local winds.

Chapter 1

Introduction

The overarching goal of this dissertation is to identify the causal mechanisms behind very rapid sea ice loss events (VRILEs). These dramatic sea ice loss events occur over short time periods, losing an average of 0.18×10^{-6} km^2 of sea ice on the scale of days(Cavallo et al.). There are three main mechanisms proposed as causal mechanisms: poleward transport of atmospheric heat, ocean wave mechanically breaking up the sea ice, and ocean heating from wind driven vertical mixing. Our aim is to determine the relative importance of these mechanisms.

1.1 Motivation

The Arctic is a dynamically changing environment, warming at approximately twice the rate as the rest of the world (e.g. Solomon et al. 2007; Blunden and Arndt 2012; Huang et al. 2017). One of the many consequences of accelerated warming in the Arctic is a dramatic reduction in both sea ice extent and thickness, particularly in the summer (Comiso 2012; Lindsay and Schweiger 2015; Kwok 2018). This sea ice decline has resulted in more open ocean in this region than ever recorded, opening sea lanes not previously accessible (Stephenson et al. 2013; Stephenson and Smith 2015). These sea lanes make available the abundant natural resources of the Arctic. Accessing these newly available regions safely requires a thorough understanding of the hazardous ocean and weather conditions that occur there (Eicken et al. 2009; Lovecraft et al. 2013; Knol et al. 2018).

The Arctic's warming climate is also connected to an increase in the human populations in the region (Durkalec et al. 2015). These populations will be affected by coastal erosion, cyclone activity, and other climatological changes (Overeem et al. 2011; Dobrynin et al. 2012; Hemer et al. 2013; Barnhart et al. 2016). Ensuring the safety of the local populations

and shipping workers during hazardous weather events requires reliable forecasting for the Arctic.

In addition to the concerns for Arctic stakeholders, a better understanding of the connection between cyclones and sea ice is critical for improving modeling capabilities. In some years a strong, long-lived cyclone can have dramatic effects on sea ice extent (SIE), in the case of the Great Arctic Cyclone of 2012 (Simmonds and Rudeva 2012). But most cyclones do not result in such dramatic ice loss (Valkonen et al. 2021). These differences provide a substantial challenge for seasonal prediction models' ability to forecast summer sea ice minimum extent (Stroeve et al. 2015). Even the most sophisticated global climate models do not capture current observed trends in Arctic cyclones (Nishii et al. 2015; Day et al. 2018). Additionally most climate models consistently underestimate SIE decline (Msadek et al. 2014). However, the latest release of the Community Earth Systems Model (CESM2) has a strong negative bias in SIE, hinting at an over correction between CESM and CESM2 in certain sea ice processes and potentially missing important physical processes in sea ice dynamics (DeRepentigny et al. 2020). Improving our understanding of short timescale sea ice processes will provide valuable insight to these issues.

1.2 Background

1.2.1 Sea Ice

Arctic sea ice varies across many time scales. It has a strong annual cycle, freezing in the autumn and winter and melting in the spring and summer, but there is also a significant amount of interannual variability. As the Arctic continues to warm at twice the rate as the rest of the planet (Solomon et al. 2007; Blunden and Arndt 2012), sea ice has declined in both thickness and extent (Comiso 2012). These differences are especially noticeable in September at the end of the melt season (Simmonds and Keay 2009). Even the most conservative estimates predict that this enhanced climate change will result in an ice-free September this century (Stroeve et al. 2007; Docquier and Koenigk 2021),. However, as

of the time of this writing, 2012 still holds the record minimum for September sea ice extent (Fetterer et al. 2017). Several mechanisms have been investigated to understand the interannual variability, including changes in cloud cover, wind, both atmospheric and oceanic heat transport, and cyclone activity (Stroeve et al. 2012; Cai et al. 2023; Wang et al. 2024).

There are many ways in which a warming climate affects Arctic sea ice. Reduced sea ice extent is linked to increases in atmospheric and ocean mixed-layer temperatures (Stroeve et al. 2012), surface solar heating (Perovich et al. 2008; Xie et al. 2024), and ocean heat fluxes (Steele et al. 2008; Hayden and O'Neill 2024). Other ways in which the Arctic's rapidly changing climate affects sea ice are less intuitive than increasing temperatures. One example is the Atlantification of the Arctic Ocean. The Arctic Ocean is fed by both the relatively cold, less saline Pacific waters and warmer, more saline Atlantic waters. One of the consequences of climate change in the Arctic is the Arctic Ocean becoming more like the Atlantic Ocean (Årthun et al. 2012). This means warmer ocean temperatures and an increase in near surface salinity, both of which can further increase sea ice melt and inhibit sea ice growth (Lind et al. 2018). The length of the melt season is also increasing. This not only allows for more ice to melt but also reduces the amount of time sea ice has to recover before the next melt season (Markus et al. 2009; Stroeve and Notz 2018). There has also been a decrease in the percentage of sea ice that persists from year to year, known as multi-year ice (Bi et al. 2020). Multi-year ice is thicker compared to first year ice and consequently harder to melt, meaning that current sea ice is more susceptible to large changes than in the past (Comiso 2012).

Some of sea ice's interannual variability can be attributed to teleconnection patterns, specifically the Arctic Oscillation (AO) (e.g. Ogi and Wallace 2007; Knudsen et al. 2015) and the North Atlantic Oscillation (NAO) (Kwok 2000). Schematics of the positive and negative phases of these teleconnection patterns are presented in Figures 1.1 and 1.2. Winter and springtime high AO indices tend to be associated with reduced sea ice cover in

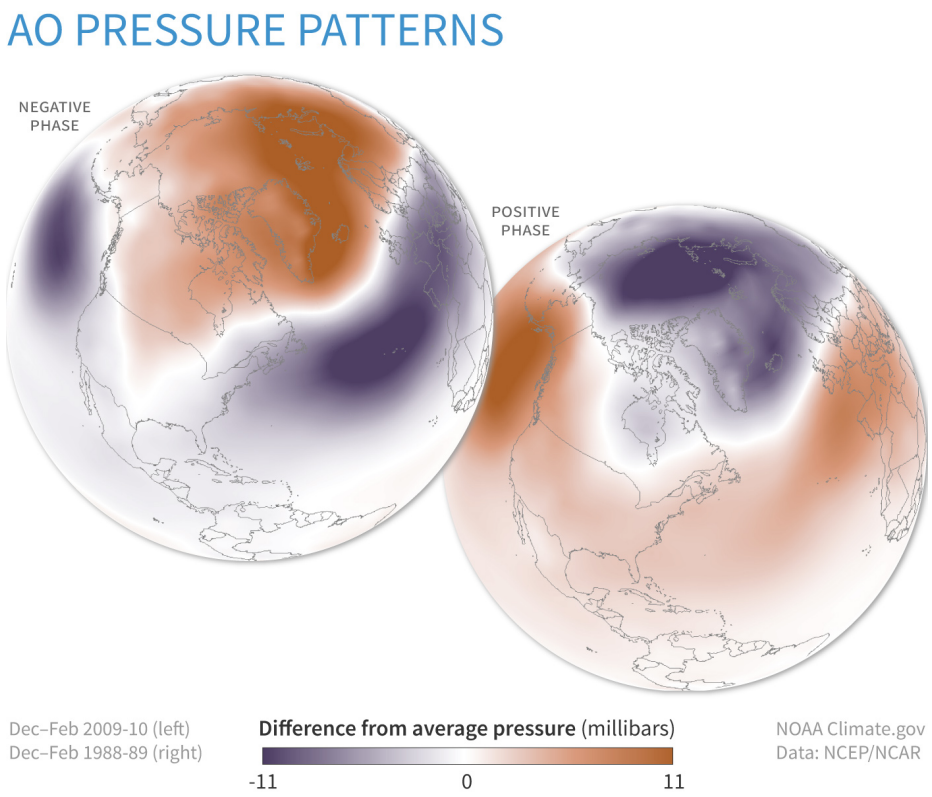


Figure 1.1: Winter surface pressure anomalies associated with the strong positive and negative Arctic Oscillation) AO indices. Image comes NOAA Climate.gov and is based on data from the Physical Sciences Lab (Lindsey 2009).

the eastern Arctic ocean, Greenland Sea, and Barents Sea (Kwok 2000). Increased sea ice flux through the Fram Strait is strongly correlated with the positive phase of the NAO (Kwok and Rothrock 1999). Additionally, persistent anomalies in the upper troposphere, not specifically tied to a known teleconnection pattern, can also affect sea ice. When there is a persistent positive potential temperature anomaly in the upper troposphere in the late spring and early summer, September sea ice extent tends to fall below the climatological trend (Screen et al. 2011). The mechanism behind this relationship is thought to be that the upper level anomaly leads to fewer clouds and fewer cyclones over the Arctic, which allows for more direct sunlight on the sea ice and that this enhanced short wave radiation leads to enhanced melt (Screen et al. 2011).

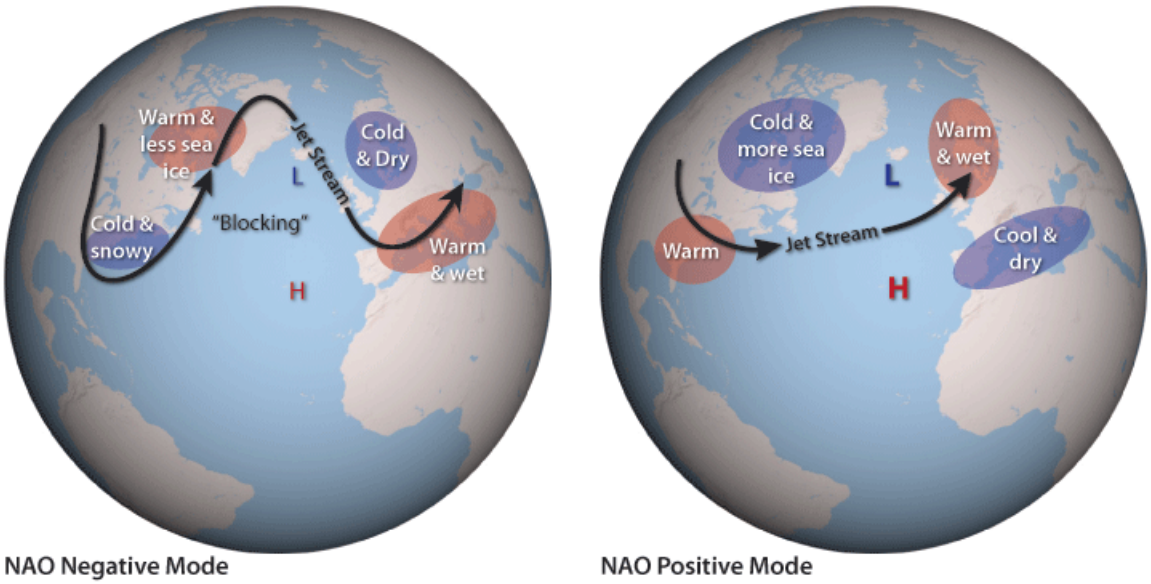


Figure 1.2: Schematic of the positive and negative phases of the North Atlantic Oscillation (NAO). Image is from NOAA Climate.gov (Lindsey and Dahlman 2009).

One of the large open questions in global climate models representing sea ice is the role interannual variability plays. Interannual variability is observed to be an important factor in Arctic sea ice trends, both in paleo (Chan et al. 2017; Hörner et al. 2017; Kolling et al. 2018, e.g.) and satellite era records (Notz and Stroeve 2018; Roberts et al. 2020, e.g.). It accounts for 40-50% of the observed multi-decadal trends in Arctic sea ice (Ding et al. 2019) and as much as 60% of the declining trend of September sea ice extent (Ding et al. 2017). Further complicating matters, the sea ice's susceptibility to influence by internal factors are not spatially uniform (England et al. 2019; Olonscheck et al. 2019). While only 10% of observed sea ice trends in the Eastern Siberian Sea can be attributed to internal variability, that number jumps to over 60% in the Barnets and Kara seas (England et al. 2019). Additionally, sea ice variability is not uniform in time. March sea ice variability is driven by radiative feedback of clouds and water vapor (Luo et al. 2017), surface albedo, surface winds, and oceanic heat transport while September sea ice interannual variability is primarily driven by surface albedo and temperature effects (Olonscheck et al. 2019).

Four important factors in sea ice internal variability are temperature (Olonscheck et al. 2019; Dahlke et al. 2020), winds (Graham et al. 2019), ocean heat flux (Docquier et al. 2021) and riverine heat flux (Park et al. 2020). The relative important of each of these factors is difficult to quantify due largely to differences in model representation (Burgard and Notz 2017) and sparsity of their observations. While CMIP6 has introduced tools to help address issues of inter-model comparison (Keen et al. 2021), the lack of observations remains a challenge to researchers.

Studies in the early 2000s indicated possible links between sea ice variability and the North Atlantic Oscillation (NAO) (Deser et al. 2000; Hu et al. 2002) or the Arctic Dipole (Watanabe et al. 2006). However, more recent research has shown that trends in Arctic sea ice decline cannot be directly attributed to either of these teleconnection patterns (Deser and Teng 2008). Though there is evidence that suggests that the NAO has a role to play in summer sea ice extent (Ogi et al. 2008, 2010). Other trends in general atmospheric circulation also play a role in Arctic sea ice decline. Observations indicate that stronger Arctic warming, and consequently faster sea ice decline, is connected to cooler SSTs over the tropical, Eastern Pacific (Kosaka and Xie 2013). However, global climate models fail to represent linkages between the Arctic and the low latitudes (Ding et al. 2019).

1.2.1.1 Sea Ice Trends

Arctic sea ice decline has long been a strong indicator of the effects of climate change. Driven by the ice-albedo effect and other climate feedbacks, Arctic amplification has had devastating effects on sea ice (e.g. Solomon et al. 2007; Blunden and Arndt 2012). Perhaps most noticeable has been the decline of September minimum sea ice extent throughout the satellite record and its accelerated decline in recent decades (Kwok and Cunningham 2010; Comiso 2012). But there are other, perhaps less obvious climatological trends in Arctic sea ice. Until recently, the March maximum sea ice extent appeared to be relatively unaffected

by climate change (Cavalieri and Parkinson 2012). However, as much of the Arctic's multi-year ice has disappeared and been replaced by relatively thin and easier to melt first year ice, March extent has begun to exhibit a decreasing trend as well (Stroeve and Notz 2018). Along with the transition from predominately multi-year to predominately first year ice, there has been a significant decrease in sea ice volume (Meredith et al. 2019).

Even though these trends are well understood, there is significant interannual variability to them (Notz 2014). For example, the record minimum September sea ice extent occurred in 2012 and has not been surpassed in the following decade (Stroeve and Notz 2018). The mechanisms behind this interannual variability are not well understood, which represents a significant obstacle for sea ice forecasting (Notz 2014).

1.2.1.2 Sea Ice In Global Climate Models

Global climate models have consistently been too conservative in their representation of Arctic sea ice's response to climate change (e.g. Msadek et al. 2014; Notz and Community 2020). This underestimation is evident by the models failing to capture observed trends in climate change and results in predictions of when the Arctic will experience ice free summers that are years or even decades too late (Notz and Stroeve 2016; Rosenblum and Eisenman 2017; Notz and Community 2020). Much of this uncertainty is rooted in how global climate models account for the sea ice's internal variability. CESM2 LENS is an exception to this rule, having an overall negative sea ice bias rooted in insufficient growth of winter ice thickness (DeRepentigny et al. 2020). This negative sea ice bias is a change from CESM1, which has a strong positive sea ice bias (DeRepentigny et al. 2020). However, the negative bias in CESM2 can be corrected for by adjusting parameters in the sea ice model physics related to surface albedo, surface melt, sea ice thickness, and summer ice area (Kay et al. 2022).

1.2.1.3 Observations

Satellite observations provide the most robust spatial coverage of the Arctic. Before the satellite era, consistent measurements of the entire region were impossible. Generally speaking, the goal of Arctic satellite monitoring platforms is to provide broad coverage of the entire region. Consequently, most satellites pass over each location in the Arctic once or twice a day. This temporal coverage makes it impossible for satellites data to provide detailed looks at short time scale processes. Additionally, there can be challenges in determining certain surface values from satellite data (Sallila et al. 2019). For example, differentiating between ice melt ponds and open ocean or clouds and ice can be difficult, which can lead to incorrect estimations of sea ice extent (Tilling et al. 2020).

Another source of Arctic data comes from a network of buoys managed by the International Arctic Buoy Program (IABP). This program operates a number of ice-fast atmospheric stations and buoys as well as ocean buoys. While each platform carries different instrument packages, the most common measurements taken are surface temperature and pressure. The main limiting factor of these platforms tends to be battery life and their ability to survive multiple freeze and melt cycles, with few platform lifetimes exceeding 18 months. Buoys are also limited spatially due to each one only being able to sample a single point in space and the platforms drifting with ice motion and ocean surface currents. Also, the observational platforms are not evenly distributed across the Arctic with the majority of the IABP's buoys located north of Alaska.

Finally, another invaluable data resource for studying the Arctic comes from observations collected during field campaigns. An excellent example of such a campaign is the 2019 MOSAiC project in which the German icebreaker, Polarstern, was embedded in the sea ice and allowed to drift for a full year (Nicolaus et al. 2022). This campaign collected data products ranging from atmospheric profiles, aerosol concentrations, ice biogoechemistry, and ocean profiles. Data such as these provide invaluable insights to the processes affecting sea ice, they do not give information across spatial and temporal scales.

1.2.2 Arctic Cyclones

In this section we give an overview of Arctic cyclones, addressing their definition, seasonal and regional variability, and climatological trends. Additionally we address how these features are represented in climate models, specifically focusing on CESM and CESM2 LENS.

There is no singular definition of an Arctic cyclone but generally speaking they are synoptic-scale cyclones that either form in the Arctic or are transported into it. The broadest definition is any cyclone that spends any amount of time north of 60°. The most restrictive definition classifies Arctic cyclones as long-lived, barotropic features that undergo both genesis and lysis over the central Arctic (Tanaka et al. 2012). Most studies use a definition closer to the former than the latter for identification purposes. Arctic cyclones may differ structurally from extra-tropical cyclones with an axi-semetric, cold-core, barotropic structure in their mature phase (Tanaka et al. 2012; Aizawa et al. 2014; Aizawa and Tanaka 2016; Tao et al. 2017).

Whatever the specific definition, there are two broad categories that these cyclones fall into: cyclones that are born in the Arctic and cyclones that migrate in from the mid-latitudes. These categories are important because they have different seasonal and climatological variability (Sepp and Jaagus 2011). Additionally, cyclones entering from the mid-latitudes tend to be stronger than those generated over the Arctic Ocean (Zhang et al. 2004). Many mid-latitude cyclones that migrate into the Arctic originate within the Icelandic Low (IL), where the strongest systems are found (Serreze et al. 1993).

Other complicating factors in discussing Arctic cyclones are differences in cyclone tracking algorithms and differing definitions for the Arctic itself. The southern border of the Arctic is generally taken to be between 60 and 70° N. While the choice of latitude is somewhat arbitrary it does affect how cyclones are divided between those two broad categories previously mentioned. Some of the main issues to come up with different tracking algorithms are whether vertical vorticity maxima or mean sea level pressure minima are

tracked and whether the algorithm requires closed contours of the specified field to consider it a cyclone. For example, an algorithm that tracks vertical vorticity maxima may identify cyclogenesis before one that tracks sea level pressure minima (Mesquita et al. 2009; Neu et al. 2013; Rudeva et al. 2014).

Generally, there are fewer Arctic cyclones in the winter than there are in the summer and winter cyclones tend to be stronger than their summer counterparts (Zhang et al. 2004; Crawford and Serreze 2016; Day and Hodges 2018). There can be regional variations to that pattern. Winter is the more active season than summer for cyclones in the North Pacific, Bering Sea, and Alaska (Mesquita et al. 2010). Figure 1.3, taken from Valkonen et al. (2021), shows cyclone counts for the cold season (Figure 1.3 a-c) and warm season (Figure 1.3 d-f) and their differences (Figure 1.3 g-i) from 1979 - 2015 in three different reanalysis datasets and shows the seasonal differences in cyclone count location.

When strong, open systems, which are not usually captured by tracking algorithms, are included in cyclone counts, winter emerges as the most active season (Simmonds et al. 2008). Some of these inconsistencies can be attributed to differences in how an individual study defines the Arctic. However, despite these differences, there is general consensus in the literature that over the Central Arctic Ocean (CAO), there are fewer but stronger storms in the winter than the summer (Crawford and Serreze 2016).

The Arctic frontal zone (AFZ) is a baroclinic region in the Arctic that is the result of the land-sea temperature contrasts along the Arctic coastline. This region appears in the literature as early as 1945 (Dzerdzeevskii 1945) and was generally considered to be an important region for cyclogenesis (Reed and Kunkel 1960; Serreze et al. 2001; Serreze and Barrett 2008) based on the baroclinic instability model for genesis of extratropical cyclones (Eady 1949; Farrell 1985; Pierrehumbert and Swanson 1995). It develops in the spring and persists through the summer as sea ice retreats and snow ashore melts (Reed and Kunkel 1960). Over the ocean, energy from incoming solar radiation goes into melting sea ice and

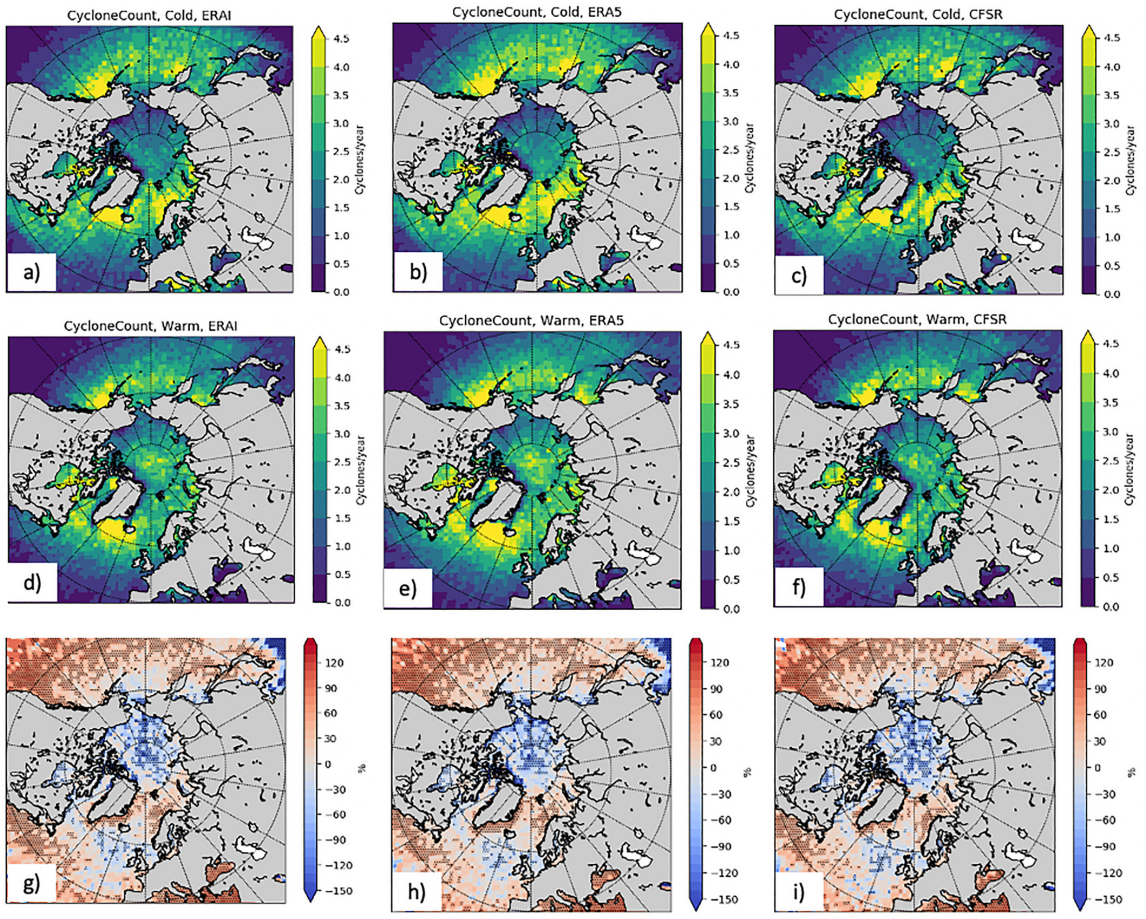


Figure 1.3: Figure 2 from Valkonen et al. (2021). The seasonal average cyclone count for 1979–2015 calculated over 150 × 150 km grid boxes. Panels (a–c) show results for the cold season, and (d–f) for the warm season. The last row shows the difference between cold and the warm seasons. First column (a, d, and g) shows results for ERA-I data, the second column (b, e, and h) for ERA5 data, and the last column (c, f, and i) for CFSR. Statistically significant differences are shown by the stippling.

heating the upper layer of the ocean, resulting in only small increases in air temperature. In contrast, air over the land increases quickly once the snow has melted.

It should be noted that in some places, the term Arctic front and Arctic frontal zone are used to describe the boundary of the Arctic air mass. That feature exists year-round, but its border varies seasonally and geographically. It also roughly corresponds to the northern border of the boreal forest (Bryson 1965). While this air mass boundary is sometimes referred to as the Arctic front, it is a separate feature from the AFZ discussed here.

Climatological studies indicate that in the summer, regions with the highest frequencies of cyclogenesis are to the south of the AFZ. More specifically, summer cyclogenesis favors the lee sides of the Verkhoyanski, Cherski, Gydan, and Mackenzie mountain ranges in Siberia and Alaska (Crawford and Serreze 2016). This led Crawford and Serreze (2016) to conclude that the AFZ plays a more important role in cyclone intensification than cyclogenesis.

There are additionally regional variations in cyclone frequency that themselves can vary seasonally. The North Atlantic storm track is a persistent region of both cyclogenesis and cyclolysis in the North Atlantic Ocean and Greenland and Norwegian Seas, which is especially important in the winter (Serreze 1995). In the summer, additional regions of cyclogenesis are present over Siberia and Canada, as discussed in conjunction with the AFZ. Also note that the North Atlantic storm track is collocated with the Aleutian Low, which is strongest in the winter. Strengthening or weakening of the Aleutian Low tends to correspond with strengthening and weakening of the Azores High. These patterns taken together are the North Atlantic Oscillation (NAO) (Walker 1923). A positive NAO is associated with an increase in cyclone activity in this region both in counts and intensity (Serreze et al. 1997).

No long-term trend in the overall number of cyclones in the Arctic has been found (Screen et al. 2011; Simmonds et al. 2008; Serreze and Barrett 2008). There is evidence that the number of cyclones entering the Arctic is increasing, specifically through the Bering

Strait, Alaska, the Baffin Sea, and Eastern Siberia but the number of cyclones formed over the CAO has remained constant (Sepp and Jaagus 2011). Cyclone counts, depth, and radius are connected to the Arctic Oscillation (AO) and to a somewhat lesser degree the NAO (Simmonds et al. 2008). The positive phase of the AO is associated with cyclones that are deeper, larger, and occur more frequently. Though the relationship between a positive AO and cyclone frequency and depth is stronger than the relationship with cyclone size (Simmonds et al. 2008).

1.2.3 Tropopause Polar Vortices

A tropopause polar vortex (TPV) is an extratropical feature based on the dynamic tropopause that can be either a cold-core cyclone or warm-core anti-cyclone. They are especially common in the Arctic because the polar environment is particularly conducive to sustaining vortices (Hakim 2000) and radiative cooling dominates over latent heating (Cavallo and Hakim 2013). A cyclonic TPV is characterized by a negative potential temperature anomaly, higher pressure and consequently a lower tropopause height. They are defined by a closed material contour and typically have a radius less than 1000 km. Additionally they can be incredibly long lived, with lifetimes capable of exceeding a month, making them the longest lived sub-synoptic scale atmospheric features on Earth (Cavallo and Hakim 2009, 2010).

TPVs play a role in the development and intensification of surface cyclones. The importance of tropopause disturbances in the development of synoptic scale surface cyclones is well established (e.g. Eliassen and Kleinschmidt 1957; Hoskins et al. 1985). TPVs also have important implications for improving predictability in both the Arctic and mid-latitudes (Yamazaki et al. 2015; Cavallo et al. 2016). But here, we are primarily concerned with their connection to Arctic cyclones. A surface cyclone can form when a TPV passes over a temperature gradient at the surface, such as the AFZ or the sea ice margin.

1.2.4 Atmospheric and Ocean Drivers of Sea Ice Loss

1.2.4.1 Cyclone Interactions

There are large bodies of work addressing Arctic cyclones and sea ice variability individually (e.g. Zhang et al. 2004; Serreze and Barrett 2008; Simmonds et al. 2008; Wang and Overland 2009; Sepp and Jaagus 2011; Wei et al. 2016) but fewer studies on the connections between the two, though that has begun to change in recent years (Clancy et al. 2022; Finocchio et al. 2020; Finocchio and Doyle 2021; Finocchio et al. 2022; Schreiber and Serreze 2020, e.g.). Much of the literature addressing connections between sea ice loss and Arctic cyclones is focused either on individual storms (e.g., Holt and Martin 2001; Simmonds and Keay 2009; Lammert et al. 2009; Blanchard-Wrigglesworth et al. 2022) or overall trends in cyclone characteristics during anonymously high and low sea ice years (e.g., Simmonds and Keay 2009; Screen et al. 2011; Valkonen et al. 2021).

Perhaps the most well-known cyclone associated with a large, sudden sea ice loss event is the Great Arctic Cyclone of 2012 (Simmonds and Rudeva 2012; Parkinson and Comiso 2013; Kriegsmann and Brümmer 2014). While the Great Arctic Cyclone is not the strongest or longest-lived storm recorded in the Arctic (Simmonds and Rudeva 2012), it was associated with 4.4% of the total decrease in sea ice extent that season, contributing to 2012's record minimum extent (Zhang et al. 2013).

There are several mechanisms by which an individual cyclone may affect sea ice. A cyclone can transport sea ice out of the Arctic through the Bering Strait or Barrents Sea and into lower latitudes where melt can more easily occur (Ogi and Wallace 2007; Ogi et al. 2008). Other mechanisms for sea ice melt have to do with the interplay between the atmosphere, ocean, sea ice. The marginal ice zone, the transitional region between open ocean and the solid sea ice pack, is frequently exposed to wind driven ocean waves and these coupled interactions have been the focus of a large body of research, both theoretically and practically (e.g. Wadhams 1981; Squire 2007; Asplin et al. 2012, 2014; Collins III et al. 2015). One such event was observed during a field campaign in 2009 by Asplin et al.

where large ocean swells penetrated the sea ice pack up to 250 km from the edge, resulting in a significant size reduction of the ice floes (Asplin et al. 2012). Once the sea ice is mechanically broken into these smaller pieces, a greater area is exposed to heat fluxes causing it to be more susceptible to melt, especially in the summer months (Asplin et al. 2014). The sea ice margin is also a baroclinic zone which may contribute to local cyclongenesis or strengthening, especially in the autumn (Overland and Wang 2010; Inoue and Hori 2011). Strong winds can lead to upwelling, mixing warm ocean water up from beneath the freshwater cap and induce sea ice melt (Zhang et al. 2013).

Studies not focused on individual storms tend to address overall trends in cyclone characteristics during anomalously high and low sea ice years (e.g., Simmonds and Keay 2009; Screen et al. 2011). Years with anonymously low September sea ice extent tend to have fewer storms earlier in the summer than other years (Screen et al. 2011). There is no difference in the number of September cyclones between low and high sea ice years, but low sea ice years tend to have deeper and larger September cyclones than high sea ice years (Simmonds and Keay 2009).

Cyclones that occur in the late spring may act to preserve sea ice by increasing the cloudiness and consequently reducing melting from direct sunlight (Curry et al. 1993; Intrieri et al. 2002) and cyclones in the winter can sometimes increase the Arctic ice mass (Kriegsmann and Brümmer 2014), highlighting the complex nature of cyclone-sea ice interactions.

Our hypothesis is that the ocean wave mechanical effects are just as, if not more, important for VRILE formation than atmospheric heat transport and ocean up-welling. We approach this problem through several lenses. The next chapter lays out the data and methods used in all of these approached. First, we evaluate the performance of climate models in capturing subseasonal sea ice losses generally and VRILEs specifically. This establishes the efficacy, or lack thereof, of using climate models to study VRILEs. These results are presented in Chapter 3. Secondarily, we take a statistical approach, using multivariate

empirical orthogonal functions to characterize the relative importance of three proposed mechanisms for VRILEs. Chapter 4 presentes the results of this analysis. Finally, since no existing model allows ocean waves to interact with the sea ice, we construct a simple one dimensional sea ice model forced by ocean waves to evaluate the nature of those interactions. Results from the one dimensional model are in Chapter 5. Chapter 6 summarizes the main takeaways from this work as a whole.

Chapter 2

Data and Methods

Chapters 3-5 present results from three very different approaches to the overall topic of this dissertation: what physical mechanisms cause VRILEs? Consequently, this chapter, which presents the data and methodology utilized for each approach, is divided into three sections corresponding to each of those chapters. These sections are the comparison of Arctic sea ice and surface cyclones between observations and model representation, statistical analyses utilizing multivariate empirical orthogonal functions, and a one dimensional dynamic sea ice and ocean wave model.

2.1 Comparison of Arctic sea ice and cyclone properties between CESM2 LENS, observations, and ERA5

The overarching goal of this section is to quantify how well CESM2 performs in the Arctic with regards to its representation of sea ice concentration, ability to capture trends in sea ice extent, performance in capturing short time scale sea ice processes such as VRILEs, and representation of surface cyclones. For the sea ice field, we compare CESM2 to datasets from the National Snow and Ice Data Center (NSIDC) (Fetterer et al. 2017). All other variables come from ERA5 reanalysis (Hersbach et al. 2019). Both CESM2 LENS (Rodgers et al. 2021) and a subseasonal forecast system utilizing CESM2 (Richter et al. 2022) that we refer to as CESM2 S2S in the text.

2.1.1 CESM2 LENS Ensemble Member

CESM2 is a fully coupled climate model with components that model the atmosphere, ocean, land, land ice, sea ice, river run off, and ocean waves in Earth's past, present, and future (Kay et al. 2015). CESM2 LENS has 100 ensemble members initialized from various

points in its 1400-year pre-industrial simulation. Each member's output ranges from 1850 - 2101 (Rodgers et al. 2021). Because comparing all 100 ensemble members to observations is not computationally feasible, a single ensemble member is selected. The single member chosen is the member with the highest correlation to the ensemble mean in monthly average sea ice extent. Data from this member is used for all sea ice and surface atmospheric fields. The one that met these criteria was the 17th member started in model year 1301, identifiable by the label "1301.017" in the filename.

Since model year does not directly relate to calendar year, we determine a comparable time period in CESM2 LENS data to NSIDC data from 1980-2020. Figure 2.1 shows September and March sea ice extents in both datasets. These figures illustrate CESM2 LENS's negative bias in sea ice extent that is well discussed in the literature (Keen et al. 2021; DeRepentigny et al. 2020; DuVivier et al. 2020, e.g.). Two forty year time periods are selected from CESM2 LENS to compare to NSIDC data in our analyses. CESM2 LENS has its maximum September sea ice extent in model year 1964. Model years 1960-2000 are selected because those years are closest in September sea ice extent to the observational dataset in both overall extent and linear climate trend. The second dataset selected is 1910-1950. This range is selected because it represents model performance without a strong climate trend present. This allows us to consider model performance in a base state without strong climate forcings.

2.1.2 Identifying VRILEs

A VRILE is defined as the bottom 5% of loss events of the daily change in sea ice extent that has been filtered to remove processes that occur on a timescale greater than 18 days (Cavallo et al.). NSIDC provides daily sea ice extent data from 1988 onward and every other day from 1978-1988 (Fetterer et al. 2017)). These data are linearly interpolated in time to fill in the missing days between 1978 and 1988 to provide temporally consistent data from 1978 to present. The dataset being continuous in time is necessary for several of the

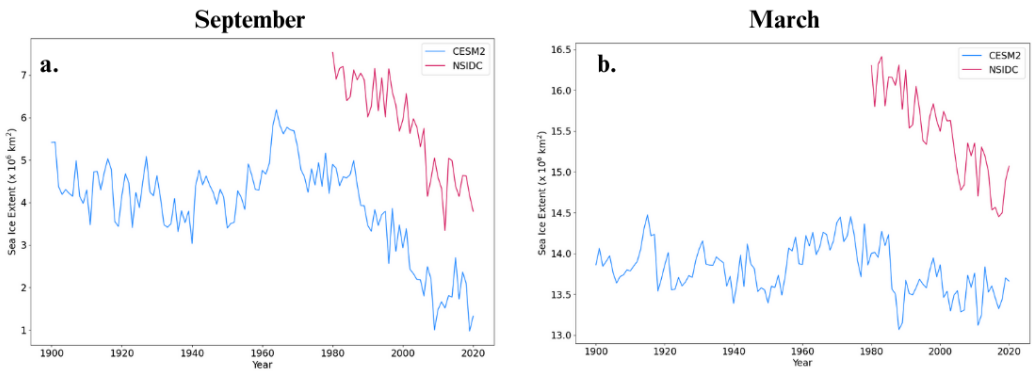


Figure 2.1: September (a) and March (b) average sea ice extent for CESM2 LENS (pink) and NSIDC (blue). CESM2 LENS data is from 1900-2020 and NSIDC data from 1980-2020.

analyses performed, including the filtering process and power spectra and EOF analysis described in the next section. The daily change in extent is calculated and a three day running mean is applied before filtering the data with a Butterworth filter to remove longer timescale processes. Sea ice extent is not an output variable of CESM2. Instead, it retains the percent of each grid cell that is covered in sea ice on the U grid. CESM2 LENS has two spatial grids, the U grid and the T grid (Kay et al. 2015). On a rectangular grid, the T grid corresponds to the center of each rectangle and the U grid to the upper right corner. Sea ice extent is calculated by first isolating the northern hemisphere and identifying every grid cell with an ice area of at least 15%. Then the percentage is multiplied by the area of each of the grid cells retained. These values are summed, resulting in sea ice extent. Note that cell area on the U grid is a CESM2 output variable. Once extent is calculated, data processing proceeds as with the NSIDC data.

The process described above locates VRILEs in time but not space. In order to locate VRILEs in space, the five day change in sea ice concentration for the appropriate date is calculated and then the largest connected region of loss is found. The specific location of the VRILE is found by doing a center of mass calculation within the region of loss, with percent change in sea ice coverage taking the place of mass.

2.1.3 CESM2 Reforecasts

In addition to the large ensemble, CESM2 is used to produce subseasonal forecasts and reforecasts (Richter et al. 2022). We utilize these reforecasts to analyze four VRILE cases, comparing the model's performance to NSIDC and ERA5 data. Two summer and two winter VRILEs are selected, one on the Atlantic side and one on the Pacific side of the Arctic in each season. The VRILEs selected occur on 3 July 2007, 11 December 2011, 9 August 2012, and 23 December 2016.

The reforecasts are initialized every Monday from 1999 - 2020 and run for 45 days. The atmosphere is initialized with NCEP coupled forecast system model version 2 (CFSv2) (Saha et al. 2014), the land with Community Land Model (CLM2) (Lawrence et al. 2019) spun up with CFSv2, and the ocean and sea ice with the Japanese 55-year reanalysis (JRA-55) (Japan Meteorological Agency, Japan 2013) (Richter et al. 2022). These reforecasts are run with two different atmospheric dynamical cores, CAM6 (Danabasoglu et al. 2020) and WACCM6 (Gettelman et al. 2019). There are two chief differences between these dynamical cores: vertical depth of the atmosphere and atmospheric chemistry. CAM6 has 32 vertical levels reaching to 3.6 hPa while WACCM6 has 70 vertical levels that extend up to 6 x 10^{-6} hPa. WACCM6 also has interactive chemistry. CESM2 tends to perform better in terms of sea ice with WACCM6 as the atmospheric component rather than CAM6 (DeRepentigny et al. 2020) but the WACCM6 reforecasts do not have full temporal coverage from 1999-2020. There are WACCM6 reforecasts available only for the 2011 and 2016 cases. When comparing reforecast data to NSIDC and ERA5 we only use one member. The member selected has the most negative change in sea ice extent on the day of the VRILE.

When VRILEs are located in space in NSIDC, we use the five-day change in sea ice concentration. This motivates how we choose which reforecast to consider for each VRILE. We select the reforecast initialized closest to the day five days before the VRILE. For the 2007 VRILE, we use the reforecast initialized on 25 June 2007, eight days before the

VRILE Cases			
Season	Region	VRILE Date	Model Initialization
Summer	Atlantic	3 July 2007	28 June 2007
Summer	Pacific	9 August 2012	30 July 2012 6 August 2012
Winter	Atlantic	23 December 2016	19 December 2016
Winter	Pacific	11 December 2011	5 December 2011

Table 2.1: Date and region of VRILE cases and initialization date for CESM2 S2S reforecasts.

VRILE. Unfortunately the next reforecast is not initialized until 2 July, 2007 which does not give enough time to evaluate the VRILE. For the 2011 VRILE, we use the reforecast initialized on 5 December 2011. We analyze two different reforecasts for the 2012 VRILE, one initialized on 30 July and one on 6 August. Since the VRILE occurs on 9 August, the 6 August reforecast is likely to underestimate the sea ice loss but there were key atmospheric features missing from the 30 July run that motivated the consideration of the later reforecast run. Finally, for the 2016 VRILE we use the 19 December reforecast, which only allows for a four-day change in sea ice concentration, because using an earlier reforecast gave highly unrealistic results.

The fields we compare between the CESM2 S2S reforecasts and observations are the five day change in sea ice concentration and the five day mean in mean sea level pressure (mslp) and 10 m winds. However, wind fields from the reforecasts are only available on pressure levels, not at the 10 m level. To compare winds from the reforecasts to ERA5's 10 m winds, we take the winds at the pressure level closest to the surface to compare to ERA5's 10 m winds.

Finally, we also analyze the difference in sea ice concentration between the reforecast and NSIDC data at the start of the reforecast and on the day of the VRILE. Because these

data are on different native grids and have significantly different spatial resolutions, we project the CESM2 S2S data onto the finer NSIDC grid before subtracting them.

2.1.4 Cyclone Tracker

The tracking algorithm utilized is based on a watershed method. It identifies local minima in mean sea level pressure for surface cyclones and in potential temperature for TPVs and calculates a vorticity basin around those minima (Szapiro and Cavallo 2018). Certain parameters used by this algorithm are sensitive to the data's spatial resolution. The ERA5 data used is on a 0.5° x 0.5° grid and CESM2 LE data is on a 0.9° x 1.25° latitude x longitude grid. This difference affects how the dFilter and segRestrictPerc parameters are handled. The dFilter term sets the radius for whether a local extremum is considered the regional extrema and segRestrictPerc determines the percentile of boundary amplitudes to restrict the watershed basins. For coarser spatial resolution, the dFilter must be lowered and segRestrictPerc raised or else the tracker cuts off cyclone tracks prematurely. The exact values were determined experimentally so that the tracker returned results in line with cyclone climatologies. Additionally, tracks are restricted to points north of 60°N.

When comparing cyclone properties between the two cyclone datasets, a two-sample Kolmogorov-Smirnov (KS) test is used to determine the relatedness of the distributions. A two-sample KS test has the null hypothesis that the two samples come from the same distribution. A KS test returns two values, the KS statistic and the p-value. In a two-sample KS test, the KS statistic is the maximum distance between the two cumulative distribution functions.

2.2 Statistical Analysis of Proposed VRILE Drivers

The purpose of these analyses is to identify weather ocean wave dynamics or surface thermodynamic process are more important drivers for subseasonal sea ice loss. The specific fields from ERA5 considered are 2-m temperature, mean surface latent heat flux (LH), and

significant height of wind waves. Significant height of wind waves is the average height of the top third of wind driven ocean waves, which specifically excludes wave height due to swell. If the process driving sea ice loss in VRILEs is wind-driven waves breaking apart the ice, then we would expect to see high wind wave heights when VRILEs occur.

Initially, we considered several other fields as well, including surface winds, pressure gradient, and normalized energy flux into waves. The three fields selected all have high RMSC values and proposed direct mechanisms for inducing sea ice loss, which makes interpreting the results more concrete.

For the analysis, data from February 1, 1988, through December 31, 2019 in NSIDC and ERA5 are used. This time range was chosen because of the availability of daily sea ice concentration data at the time of access. To perform a multivariate EOF between datasets they much share at least one dimension. Consequently, daily mean values from ERA5 over the same date range are used so that the datasets share a temporal dimension.

We begin by calculating the root mean square covariance (RMSC) between the daily average of various atmospheric and ocean wave fields and the daily change in sea ice concentration. These fields are divided into the summer months of June, July, and August (jja)and winter, December, January, and February (djf), and Atlantic (120E-90W) and Pacific (90W-120E) sections. These sections were chosen so that the Pacific region contains the average location of the Beaufort High.

To calculate the RMSC between two fields, we start by finding their covariance matrix. For two data sets, $A_{m\times n}$ and $B_{m\times p}$ their covariance matrix, C is given by

$$C = \frac{1}{m-1} AB^T, \tag{2.1}$$

and

$$RMSC = \sqrt{\frac{1}{s^2} Tr(CC^T)}, \tag{2.2}$$

where s is the mean variance of C, and Tr is the trace.

Preparing the data for analysis requires several steps. For sea ice concentration, we first find the daily change in sea ice concentration and for all other fields we calculate the daily mean. Then we remove the seasonal cycle and any linear trend in the data and smooth the data in space with a Gaussian filter.

We calculate RMSC between the fields with the atmospheric field lagged behind sea ice for 0-3 days and for a five day running mean applied both fields. Finally, we further filter the data by performing singular value decomposition on it and retaining the top 80% of the data. This filter was added for consistency with the multivariate EOF analysis. Only retaining the 80% most significant data reduces noise in the output signal of the multivariate EOF. When performing the multivariate EOF analysis, we only use the data smoothed in time and not the lagged data.

2.2.1 Multivariate Empirical Orthogonal Functions

Multivariate Empirical Orthogonal Function (EOF) analysis is a statistical tool for determining spatial and temporal patterns that best explain the covariance between multiple fields. The mathematical engine behind this analytical tool is a singular value decomposition, which takes any m x n matrix, M, and converts it to the product of three matrices:

$$M = U\Sigma V^T. \tag{2.3}$$

Both U and V are square matrices with orthonormal bases and are orthogonal to each other. Σ is a rectangular, diagonal matrix that contains the singular values, σ_{ij}, of A. The columns of U and V are the left and right singular vectors, respectively.

For multivariate EOFs, we begin by combining all of the data into a single matrix. Suppose you have two datasets, $A_{m\times n}$ and $B_{m\times p}$. Combined, these become

$$D_{m\times(n+p)} = [A_{m\times n}, B_{m\times p}] \tag{2.4}$$

and we perform singular value decomposition on the square matrix $D^T D$. This process can be expanded to include additional datasets with the same temporal sampling (m) by adding them column-wise to the matrix D.

Since the columns of U and V are ordered in descending order of relevance, the maximum covariance between A and B is represented by the first left and right singular vectors, u_1 and v_1, and the first singular value, σ_1. The fraction of the squared covariance explained for each mode is calculated by

$$f_k = \frac{\sigma_k^2}{\sum_{i=1}^{l} \sigma_i^2}. \tag{2.5}$$

The other restriction on the output is that all u_i and v_i must be orthogonal to each other. This caveat is important when analyzing physical systems because in reality, those physical systems have no such requirement.

We desire to utilize this tool to inform our understanding of the relative importance of various atmospheric and oceanic fields on Arctic sea ice variability. To that end, we structure our data as two-dimensional matrices organized as time x space. The data is pre-processed in the same manner as described for calculating the RMSC.

Once the EOF is complete, we find the leading PC timeseries, normalize them, and regress them onto the sea ice input field. Conceptually this shows how sea ice concentration changes in response to the atmospheric field. We do not consider the other signal, when the PC is regressed onto the atmospheric field, because that would be the atmospheric response to sea ice changes which is not the focus of this work.

We compute these EOFs for each atmospheric field individually and with all three combined. That is, we perform the analysis four times on $D_i^T D_i$ where

$$D_1 = [A_{\text{sea ice}}, E_{t2m}], D_2 = [A_{\text{sea ice}}, F_{lh}], D_3 = [A_{\text{sea ice}}, G_{shww}] \tag{2.6}$$

and

$$D_4 = [A_{\text{sea ice}}, E_{t2m}, F_{lh}, G_{shww}], \tag{2.7}$$

and $A_{\text{sea ice}}$, E_{t2m}, F_{lh}, and G_{shww} are time x space matrices containing the sea ice concentration, two meter temperature, surface mean latent heat flux, and significant height of wind waves data respectively.

For D_{1-3} we analyze the first four PC timeseries for physical mechanisms and for D_4, we compare its leading modes to D_{1-3}. If a mode in D_4 strongly resembles one or more in D_{1-3}, it is evidence for the relative importance of that mechanism.

2.3 Finite Element Analysis Model

The three proposed mechanisms for VRILEs are atmospheric heat transport, ocean wave dynamics, and ocean heat transport driven by vertical mixing. Most of the work addressing the relative importance of these mechanisms have focused on atmospheric heat and moisture transport CITE. However, though climate models, CESM2 in particular, capture poleward heat and moisture transport well CITE. In Chapter 3, we show that CESM2 does not capture VRILEs either in its large ensemble or in S2S reforecasts. This discrepency suggests that one or both of the proposed ocean processes play an important role in VRILE formation. In this section, we aim to determine if ocean waves driven by Arctic cyclones are capable of fracturing sea ice floes throughout the marginal ice zone (MIZ).

Climate models have historically worked under the assumption that ocean waves only minimally impact sea ice and consequently do not permit ocean waves to interact with sea ice for simplicity. However, recently that assumption is being challenged (Squire 2020) and it is now believed that ocean waves may play an important role in some types of sea ice loss. Work is being done to include sea ice-ocean wave interactions in the next generation of climate models but at the time of writing no such model exists to our knowledge.

In the absence of a functional sea ice-ocean wave dynamical model, we focus our attention on a simple question: can ocean waves fracture ice floes in the MIZ? Focusing on this question allows us to simplify our problem to a one-dimensional beam bending model. Note that this analysis does not include any thermodynamic effects and does not study the

effects of vertical mixing on the sea ice. This analysis is designed to test the assumption that ocean waves do not affect sea ice in the MIZ and studying the effects of ocean heat transport are beyond the scope of this study.

In general, our approach is to consider sea ice floes as a series of spring supported beams and calculate their response to being forced by a wave. Model set up is inspired by models of floating piers that represent its components as plates supported on each end by springs that represent buoyancy (Barros 2002). To solve for the forces and displacement of the beam, we implement this model in finite element analysis software package. Note that this package only solves for one time but can be manually updated at each time step.

The basic model set up is shown in Figure 2.2, though when conducting our experiments we have a total of ten ice floes. The left most boundary condition, point A in Figure 2.2, is fixed to represent the transition from the MIZ to solid ice pack. All other supports are springs with a spring constant of

$$k_s = \rho_{sw} g L^2, \tag{2.8}$$

where ρ_{sw} is the density of sea water and g is acceleration due to gravity. Additional supports are added to to midway point of each beam. These supports are added to directly oppose loads applied to the beam. This set up is discussed in more detail below.

We represent floes in the marginal ice zone as square slabs of sea ice of length L and depth h. When defining beam geometry, the model is given the beam cross-sectional area, $L \times h$, and the second moment of area in the $\hat{y}$ and $\hat{z}$ directions, I_y and I_z where $J_{BB'} = [I_x, I_y, I_z]$. Generally speaking, the second moment of area for an arbitrary two-dimensional shape is given by

$$J_{BB'} = \iint_R \rho^2 dA, \tag{2.9}$$

where ρ is the distance from the region dA to the origin. For a rectangle this equation simplifies greatly. For our beam,

$$\begin{aligned} I_y &= \frac{Lh^3}{12} \\ I_z &= \frac{L^3 h}{12}. \end{aligned} \tag{2.10}$$

The final geometric property to include is the torsional constant. The torsional constant for a rectangle is experimentally determined to be

$$J \approx \frac{L}{2}\frac{h}{2}^3 (\frac{16}{3} - 3.36\frac{h}{L}(1 - \frac{\frac{h}{2}^4}{12\frac{L}{2}^4})). \tag{2.11}$$

Part of initializing the beam includes setting the initial location in three-dimensional space of each user-defined node. This is important to consider when adapting the model to evolve in time as the location of each point in $\hat{z}$ must be updated from the previous time step.

There are three forces we consider from the wave: inertial (F_I), drag (F_D), and slam (F_S). The Morrison Equation,

$$F_{tot} = F_D + F_I = \rho_{sw} C_m V \dot{u} + \frac{1}{2}\rho_{sw} C_d A u|u|, \tag{2.12}$$

gives the total force exerted on an object by non-breaking ocean waves. In the above equation, C_m is the inertia coefficient, V is volume of the object impacted, $\dot{u}$ is the time derivative of the wave's particle velocity, C_d is the drag coefficient, A is the area impacted, and u is particle velocity. Since ocean waves can effectively "break" on ice floes we must also consider the slam force which is given by,

$$F_s = \frac{1}{2}\rho_{sw} C_s D u^2, \tag{2.13}$$

where C_s is the slam coefficient, D is a characteristic length scale, and ρ_{sw} and u are as before (Hirdaris et al. 2014). The slam force is important for calculating wave loads on offshore structures, such as oil rigs, wind turbines, and ships.

The values used for the constant terms are laid out in Table 2.2. However u and $\dot{u}$ are wave properties and must be calculated at each time step. For deep waves, that is waves in which the depth of the body of water is much greater than the wavelength,

$$\begin{aligned} u &= \frac{\pi H}{T} e^{kz} \cos(kx - \sigma t) \\ \dot{u} &= \frac{2\pi^2 H}{T^2} e^{kz} \sin(kx - \sigma t). \end{aligned} \tag{2.14}$$

H is the wave's height, T its period, k is wave number and equal to $\frac{2\Pi}{\lambda}$ where λ is wavelength, and σ is $\frac{2\Pi}{T}$.

Additionally, since sea ice strongly attenuates ocean waves, we add an additional term to the particle velocity and acceleration terms to account for that. This term is e^{-ax} where a is the attenuation factor with units of m^{-1}. The attenuation factor has a power law relationship with frequency, $a \propto \omega^n$, where n is generally taken to be between 2-4 (Squire 2020). However, the specific value for a and how to best implement it into parameterizations for ocean wave models is an open area of research (Squire 2020). Adding wave attenuation into our model revises the particle velocity and acceleration terms to

$$\begin{aligned} u &= \frac{\pi H}{T} e^{-ax} e^{kz} \cos(kx - \sigma t) \\ \dot{u} &= \frac{2\pi^2 H}{T^2} e^{-ax} e^{kz} \sin(kx - \sigma t) \end{aligned} \tag{2.15}$$

(Meylan et al. 2018).

In our experiments, we consider the sea ice response to a single wave passing through the MIZ. Since we have reduced the problem to a one dimension, this wave can only impart forces in the $\hat{z}$ direction. In the finite element analysis (FEA) model, this is a point load in the $\hat{z}$ direction. We choose our time-step, Δt, based on wave frequency and L such that Δt is the time is takes for the wave to travel a distance of $\frac{\mathrm{L}}{2}$. An example is shown in Figure 2.2. For example, at t0 a forces are applied at node D only, but at t1 = t0 + Δt, forces are applied to the sea ice at D and the halfway point between C and D. The model members, representing the sea ice, are fixed rigidly to the spring supports at the center of the floes but are free to rotate about the support in $\hat{z}$ at the floe edges.

For simplicity we make a key assumption about sea ice's material properties, that it behaves as a brittle material in the $\hat{z}$ direction. This assumption means both that the sea ice will not ductally deform along the z axis and that once a crack is started, it will propagate through the entire floe. This model is not sophisticated enough to change ice floe size midway through an experiment but once the experiment has completed, we note locations of fracture, ridging, and rafting based off of set criteria. These criteria are set based on the results of experiments conducted in the field on first year ice in the MIZ by Dempsey et al. (1999) who reports a flexural strength 0f 0.45 MPa. Since we are treating sea ice in our model as a brittle material, we use 0.5 MPa, the flexural strength plus a buffer of 50 kPa, as the threshold for fracture.

Sea ice behaving in a brittle manner in x and y as well as z overly simplifies our model as ice in the MIZ can both ridge, deform under compression, and raft, stack on each other (Thorndike et al. 1975). We assume ridging will occur when there are compressive forces at the boundary between two floes that exceeds the maximum tensile strength of sea ice, T_{max}. Standard sea ice parameters give $T_{max} = 1.63\frac{kN}{m^2}$ (Bouchat and Tremblay 2017). Finally, we assume that rafting occurs if a floe is vertically displaced a distance greater than ice thickness from a neighboring flow and there is a force applied in the $\hat{x}$ direction directing the displaced floe towards that neighbor.

The values of variable terms used in each experiment are presented in Table 2.3. The terms varied are floe size, slam force, wavelength, sea ice thickness, wave height, and frequency.

This concludes the discussion of the methodologies used here. The following three chapters follow the same order as their methods are presented.

Geometry		
L	50 m	Bateson et al. (2022)
h	1 m	Bateson et al. (2022)
Material Properties		
Young's Modulus (E)	$5 \times 10^9 \frac{N}{m^2}$	Chang et al. (2021)
Shear Modulus (G)	$3 \times 10^9 \frac{N}{m^2}$	Chang et al. (2021)
Sea Ice Density (ρ_{ice})	$910 \frac{kg}{m^3}$	
Sea Water Density (ρ_{sw})	$1025 \frac{kg}{m^3}$	
Coefficients		
C_m	2	Sarpkaya (1977)
C_d	2.5×10^3	Curcic and Haus (2020)
C_s	6	Cointe and Armand (1987)
Wave Properties		
λ	100 m	Squire (2020)
T	10 sec	Stopa et al. (2016)
H	3 m	Thomson and Rogers (2014), Stopa et al. (2016)

Table 2.2: Standard values used in one dimensional FEA model along with citations. These are the values used in each experiment unless explicitly stated otherwise.

Experimental Set Up							
Experiment	L (m)	F_s	λ (m)	z (m)	H (m)	a (m^{-1})	f (sec^{-1})
1	50	on	100	1	3	10^{-5}	0.1
2	100	on	100	1	3	10^{-5}	0.1
3	10	on	100	1	3	10^{-5}	0.1
4	50	off	100	1	3	10^{-5}	0.1
5	50	on	100	0.75	3	10^{-5}	0.1
6	50	on	100	0.5	3	10^{-5}	0.1
7	50	on	100	0.25	3	10^{-5}	0.1
8	50	on	50	1	3	10^{-5}	0.1
9	50	on	10	1	3	10^{-5}	0.1
10	50	on	100	1	5	10^{-5}	0.1
11	50	on	100	1	3	10^{-4}	0.3
12	50	on	100	1	3	10^{-3}	0.45

Table 2.3: Table of values for each variable in sea ice-ocean wave experiments. Experiment one is the baseline.

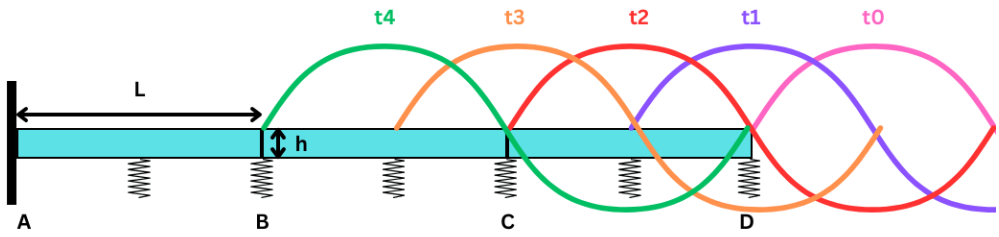


Figure 2.2: Simplified diagram of a one dimensional, dynamic sea ice and ocean wave model. This shows three ice floes of length L and depth h. Point A represents the boundary between the MIZ and solid ice pack, modeled as a fixed boundary. Points B and C are the boundaries between the floes. Point D is the location where the MIZ gives way to open ocean. Each floe is supported at its center and edges by a spring mimicking the buoyancy force, with the exception of the fixed boundary at A.

Chapter 3

Comparison of Arctic sea ice and cyclone properties between CESM2 LENS, observations, and ERA5

In this chapter we investigate Arctic sea ice extent, sea ice concentration, VRILEs, and surface cyclones in CESM2, comparing both the large ensemble and S2S reforecasts to ERA5 and NSIDC data. Our goal is to determine CESM2's efficacy in representing VRILEs. If CESM2 is able to accurately capture VRILEs even though it does not permit sea ice ocean wave dynamics, then it is unlikely that ocean waves play a large role in VRILE formation. However, if CESM2 does not accurately capture VRILEs that is not positive evidence for the importance of ocean waves. This chapter is divided into five sections: broad sea ice properties, VRILEs, case studies using CESM2 S2S reforecasts, surface cyclones, and a brief summary.

3.1 Sea ice properties

The first property we investigate is monthly average sea ice extent. Figure 3.1 shows several key differences between the CESM2 LENS and observational data. First, there is a strong negative bias in CESM2 LENS sea ice extent in all months (Figure 3.1). This bias results in ice free summers already being the norm before current day (DeRepentigny et al. 2020). Additionally, the inner quartile range is much narrower for CESM2 LENS than in NSIDC, particularly in the spring (Figure 3.1). This lack of variability is likely driven by the minimal variability in the maximum March extent (DeRepentigny et al. 2020).

CESM2 LENS's negative bias in sea ice extent is also seen in its annual minimum and maximum extents (Figure 3.2). CESM2 LENS has a reasonable depiction of the observed linear, climate trend in September minimum extent (Figure 3.2 b). In contrast, March sea ice extent does not exhibit as much similarity between CESM2 LENS and NSIDC. While

observations indicate a steady decline in the maximum sea ice extent as well, there is only a slight trend in CESM2 LENS (Figure 3.2 b).

Next, we analyze the power spectrum of the daily change in sea ice extent in both NSIDC and CESM2 LENS. This analysis shows which signals in NSIDC are captured in CESM2 LENS. Figure 3.3 shows that annual and seasonal cycles are well represented in CESM2 LENS, matching the periods in observations incredibly well. However, there is significant power at timescales less than 20 days in NSIDC (Figure 3.3 b) that not in CESM2 LENS (Figure 3.3 d). This lack of significant power in CESM2 LENS suggests that there are significant short term processes occurring in nature that are not represented in the model.

Sea ice interannual variability in CESM2 LENS gives seemingly contradictory results. On one hand, its maximum and minimum extent vary to a similar degree as observations (Figure 3.2). On the other hand, sea ice extent in CESM2 LENS has a much narrower inner quartile range than ERA5 (Figure 3.1), indicating less interannual variability in the model than observations. The latter is supported by CESM2 LENS's lack of significant power at short periods as VRILEs and other subseasonal processes may account for some of sea ice's interannual variability. While we can conclude that CESM2 LENS has less overall interannual variability than NSIDC, the mechanism behind the variability in Figure 3.2 cannot be explained by subseasonal processes because these processes do not produces significant changes to sea ice in the model.

Interannual variability in CESM2 LENS sea ice extent may be due to the Arctic Oscillation (AO) and model internal variability. While a full analysis of these factors is beyond the scope of this research, the mean pressure at the lowest model level the spring (March, April, and May) before anomalously low and high sea ice years is consistent with the mslp signal in positive and negative AO phases respectively (Figure 3.4). This relationship is consistent with observed connections between the AO and sea ice extent where low September sea ice years are correlated with a positive AO the previous winter (Rigor et al. 2002). CESM2

LENS does not have an AO index available to directly test this hypothesis but it does have an NAO index (Phillips et al. 2014). Positive sea ice anomalies have been shown to precede a positive phase of the NAO by several months (Caian et al. 2018).

The strongest correlation found is between climate detrended sea ice extent in NSIDC and the NAO when sea ice leads the NAO by three months (Table 3.1). That is, positive NAO anomalies are related to positive sea ice anomalies three months later. This is the opposite causal relationship from what was reported by Caian et al. (2018), though their work was specifically looking for a predictive mechanism for the NAO. In the non-detrended observational data, there is a correlation of 0.1012 between them when sea ice lags the NAO by six months (Table 3.1), consistent with previous findings (Caian et al. 2018). That data shows a positive correlation with sea ice leading by 3 months.

For CESM2, in both the detrended and non-detrended data, the strongest correlation between sea ice extent and the NAO is when sea ice leads the NAO by six months (Table 3.1). The correlation is ≈ -0.1 in both instances, indicating that positive NAO anomalies correlate to negative sea ice anomalies six months later. While these results are inconsistent with their observational counterparts, none of the correlations found here are particularly strong.

We also consider how sea ice loss and growth changes spatially from year to year. Another indicator that CESM2 is missing key sea ice processes would be if it gains and loses sea ice in the same places every year as that is not consistent with observations. We investigate sea ice's spatial variability by considering the standard deviation of monthly average sea ice concentration. Larger standard deviation indicates higher interannual variability at that location. Note that CESM2 LENS reaches an ice-free summer in the 1960-2000 time frame, but in reality there are not ice free summers. Consequently, we expect to see higher standard deviation values north of the Canadian archipelago in CESM2 LENS sea ice concentration than NSIDC. And indeed, this is the case. Near the seasonal sea ice edge, NSIDC has a higher standard deviation than CESM2 LENS but a lower value where multi-year ice

Correlation between sea ice extent and NAO index	-6 mo	-3 mo	0	+3 mo	+6mo
NSIDC (detrended)	0.061	-0.0167	0.1111	0.1753	-0.0161
NSIDC	0.1012	0.0549	0.0883	0.1135	0.0369
CESM2 LENS (detrended)	0.0625	0.0668	0.0530	-0.0562	-0.1026
CESM2 LENS	0.0463	0.0469	0.0304	-0.0690	-0.1102

Table 3.1: Correlation between seasonal mean NAO indices and sea ice extent between NSIDC and CESM2 LENS. For the first two rows, the NAO index is from NOAA's Climate Prediction Center (Van den Dool et al. 2000) and for the bottom two rows the NAO index is calculated from CESM2 LENS (Phillips et al. 2014). Indicated time offsets are for sea ice extent relative to the NAO.

persists (Figure 3.5). These results paint a picture in CESM2 LENS of sea ice being lost in a steady manner, slowly along the edges throughout the summer. But the NSIDC data paints a more dynamic picture, of sea ice being lost in different regions at different times from year to year. This is consistent with the analysis of the power spectrum, namely that CESM2 does well at capturing sea ice's annual and seasonal cycles but not subseasonal variability.

3.2 VRILEs

Even though CESM2 LENS does not have significant changes in sea ice extent at short timescales, we can still identify VRILEs using the same criteria as with NSIDC data. The key difference between VRILEs in CESM2 LENS and NSIDC is the amount of sea ice loss attributed to each event. VRILEs in CESM2 LENS are an order of magnitude smaller than their observational counterparts (Figure 3.6).

It is possible that this discrepancy accounts for some of CESM2 LENS's negative sea ice bias. Winter (djf) VRILEs can ultimately result in substantial sea ice growth days to weeks following the loss event by exposing the ocean surface at high latitudes (Kriegsmann and Brümmer 2014). The fact that this process is largely absent in CESM2 LENS may contribute to its underestimation of wintertime sea ice growth.

There are also notable differences in where VRILEs occur in CESM2 LENS versus NSIDC. For summer VRILEs, the locations are especially affected by CESM2 LENS's premature ice-free summers, allowing for VRILEs to occur further poleward than in observations (Figure 3.7 a-c). In the winter, CESM2's VRILEs are more clustered around the north Atlantic storm track than in NSIDC (Figure 3.7 d-f). It has no VRILEs in Hudson Bay or off Greenland's southwestern coast where there are VRILEs in NSIDC and fewer in the Bering Strait (Figure 3.7 d-f).

Using the VRILE locations, we generate composite means of mslp on the day of the VRILE. In the summer, CESM2 LENS data from both 1960-2000 and 1910-1950 show a low pressure anomaly over the VRILE location (Figure 3.8 b-c). The 1960-2000 data also captures a north-south oriented pressure gradient. ERA5 data shows an east-west oriented pressure gradient with more localized features than captured in CESM2 LENS (Figure 3.8 a). There are clear surface cyclone signals in the mslp centered data for both CESM2 datasets, consistent with the ERA5 composites (Figure 3.8 d-f). In the 1960-2000 period, the north-south oriented pressure gradient is stronger than in the VRILE centered data. The high pressure region is much more spread out than in ERA5 data in addition to the different orientation.

In the winter VRILE composites, CESM2 LENS 1960-2000 shows a weakly negative anomaly nearly everywhere (Figure 3.9 b). In the 1910-1950 VRILEs, the signal is near zero everywhere with weakly positive and negative anomalies scattered throughout the region (Figure 3.9 c). Neither CESM LENS2 period shows the pressure gradient that is present in the ERA5 data (Figure 3.9 a). However, when the composite mean is re-centered

on the closest local minimum in mslp, both CESM2 LENS periods reveal a surface cyclone (Figure 3.9 d-f). Neither signal in either CESM2 LENS period is as strong as in ERA5 and the signal is stronger in the 1960-2000 data than 1910-1950. In reanalysis datasets, less sea ice coverage is associated with larger and stronger cyclones (Valkonen et al. 2021). This association between declining sea ice and stronger cyclones may account for the different signals between the two periods in CESM2 LENS, since the period from 1960-2000 has a strong, linear climate trend and the 1910-1950 period does not. Additionally, in ERA5 there is a statistically significant region of high pressure northeast of the cyclone that is not present in the CESM2 LENS datasets (Figure 3.9 d).

In summary, CESM2 LENS is depicting a weak relationship between surface cyclones and VRILEs, especially in the summer. Missing from the CESM2 LENS composites is the clearly defined pressure gradient present in the ERA5 composites (Figure 3.8 d and 3.9 d). This is also reinforced by the fact that winter VRILEs in CESM2 LENS are strongly co-located with cyclone tracks (Figure 3.7 e-f).

3.3 CESM2 Reforecast VRILE Case Studies

This section analyzes the change in sea ice extent, change in sea ice concentration, mslp, and 10-m winds for four VRILE cases: two summer and two winter VRILEs. We begin by considering the daily change in sea ice extent in the 11 ensemble members for each reforecast. In all four cases, the daily sea ice change associated with each VRILE is much too small (Figure 3.10). Notably, the changes in sea ice extent in the reforecasts are generally $< 0.1 \times 10^6$ km^2, a similar magnitude to the VRILEs in CESM2 LENS (Figure 3.6). For the two winter cases, there is a dip in the increase in sea ice extent around the time of the VRILE but the net change remains positive (Figure 3.10 b and d). This is most likely because the seasonal trend can not be filtered out from the reforecast data like it can in NSIDC or CESM2 LENS because the reforecasts only have 45 days of data.

3.3.1 3 July 2007 VRILE

The VRILE on 3 July 2007 occurs in the Kara Sea. Noteworthy is that CESM2's sea ice field is much smoother than NSIDC's (Figure 3.11 a, c). This is likely due to the differences in the data's native grids. The NSIDC data is on a 30-km grid (Fetterer et al. 2017) while CESM2 is on a one-degree ($\sim$45 km) grid (Kay et al. 2015). Nonetheless, this reforecast captures a region of sea ice loss in approximately the same shape and location as seen in NSIDC data (Figure 3.11 a and c).

When considering the initial difference between the reforecast and NSIDC, there are broad differences along the sea ice edge (Figure 3.12 a). While CESM2 initially has too much sea ice at the VRILE location, there are also locations where it has too little sea ice relative to NSIDC (Figure 3.12 a). However, by the time the VRILE occurs, the reforecast only has positive differences, especially in the region of the VRILE (Figure 3.12 b). This means that not only is the VRILE too small, but there is too little ice loss Arctic wide during this time period. Given CESM2 LENS's overall negative sea ice bias, one might anticipate aggressive seasonal losses, however this is not the case.

In ERA5, there is a weak high-pressure region over the VRILE with a surface cyclone over Great Britain (Figure 3.11 b). Neither of these systems is particularly strong or widespread, which is different from cases later in this section. This example highlights the picture painted by the composite mean in ERA5 data (Figures 3.8 a and 3.9 a) that suggests the importance of the strength of the pressure gradient rather than the strength of either individual system. In the CESM2 data, the high pressure system is offset to the east of the VRILE and the surface cyclone is both weaker and less coherent than in ERA5 (Figure 3.11 d). Interestingly, CESM2 captures the most sea ice loss for this VRILE than the other three cases. In CESM2, the VRILE appears to occur on 1 July 2007 rather than the 3rd, losing approximately 0.12×10^6 square kilometers of sea ice (Figure 3.10). The VRILE being offset from observations is not particularly concerning due to the filtering that goes

into both datasets and is one of the reasons we consider the five-day change in sea ice concentration. While this VRILE accounts for $\approx 0.29 \times 10^6$ square kilometers of sea ice loss, there are others in the dataset closer to 0.12×10^6. Thus, while the estimated sea ice loss by CESM2 in this case is too low, it is within the normal range for VRILEs. This is not the case for any VRILE identified in CESM2 LENS (Figure 3.6).

3.3.2 11 December 2011 VRILE

The 11 December 2011 case is a wintertime VRILE in the Bering Sea. In both the NSIDC and CESM2 reforecast data there is nearly ubiquitous sea ice growth (Figure 3.13 a, c, and e). This ubiquitous growth is also present in CESM2's change in sea ice extent (Figure 3.10 b). In the CAM6 run, there is no region of sea ice loss (Figure 3.13 c). The WACCM6 reforecast indicates a small region of sea ice loss co-located with the VRILE in NSIDC data (Figure 3.13 e). Both reforecasts have too little sea ice along Alaska's west coast at the start of the reforecast (Figure 3.14 a and c). On the day of the VRILE, the WACCM6 run still has too little sea ice in that region (Figure 3.14 d) but the CAM6 run has too much relative to NSIDC (Figure 3.14 b). The CAM6 scenario can be interpreted as the change in sea ice concentration in the VRILE region (Figure 3.14 a, b) as beginning with too little sea ice and experiencing sea ice growth consistent with the seasonal trend in the reforecast resulting in an approximately zero difference between it and observations. The WACCM6 scenario (Figure 3.14 c-d), can be interpreted as the reforecast still losing sea ice in the VRILE region; thus the scenario begins and ends with too little sea ice at the VRILE location. Since the WACCM6 scenario has a less negative difference in sea ice concentration from NSIDC on the day of the VRILE than in its initial conditions, its VRILE still did not lose enough sea ice. If it had, we would expect the initial difference in sea ice between the WACCM6 scenario and NSIDC to be approximately the same as the difference between them at the time of the VRILE.

There is a large, deep surface cyclone in the Bering Sea associated with this VRILE (Figure 3.13 b). Note that while there is not a strong region of high pressure nearby, the central Arctic has relatively high pressure resulting in a strong pressure gradient across the VRILE region. Additionally, winds along Alaska's west coast are roughly parallel to the shore and directed poleward (Figure 3.13 a). While there is insufficient data to be certain, it is likely that recently frozen ice in the Bering Sea is being transported through the Bering Strait by the strong surface winds generated by the pressure gradient. The CAM6 scenario captures the surface cyclone, though it appears weaker and more sheared that its ERA5 counterpart (Figure 3.13 d). There is also a weak low-pressure system over the central Arctic and there are both poleward and equatorward surface winds in the Bering Strait (Figure 3.13 d). These winds would inhibit the type of transport mechanism described above. In the WACCM6 run, both the mslp field and 10 m winds are closer to ERA5's, with winds along Alaska's west coast consistently directed poleward, allowing for sea ice transport through the strait (Figure 3.13 f).

3.3.3 9 August 2012 VRILE

The 9 August 2012 VRILE is associated with the Great Arctic Cyclone of 2012 (Figure 3.15). For this VRILE, we consider two different reforecast runs. This choice is motivated by the fact that the Great Arctic Cyclone is absent from the first run, initialized on 30 July 2012 (Figure 3.15). Since the second reforecast is initialized on 6 August 2012, the change in sea ice concentration in Figure 3.15 e is only for three days instead of five. This is less than the five day change used to identify VRILEs.

Both CESM2 reforecasts have too little sea ice over most of the Arctic, notably near the Canadian archipelago where multi-year ice persists (Figure 3.16). The exception in both initial conditions and on the day of the VRILE being at the VRILE location (Figure 3.16 d). Additionally, CESM2 loses sea ice over this period in the central Arctic (Figure 3.15

c and e) rather than the Beaufort and Chukchi Seas (Figure 3.15 a). In the 30 July 2012 initilization, the sea ice loss is displaced to the Laptev and Kara Seas (Figure 3.15 c).

In this case, more so than the others, CESM2's negative sea ice bias seems to be at play. Even before the Great Arctic Cyclone, 2012 was on track to be a significantly low sea ice year (Zhang et al. 2013). so CESM2 losing ice everywhere is not necessarily inaccurate. However, in the observations there is sea ice growth over the five days outside of the VRILE region (Figure 3.15 a). It is highly unlikely that this sea ice gain is due to freezing because of the warm temperatures and August being the height of the melt season. Rather, transport is the most likely mechanism for those regions of growth. This suggests that CESM2 is either missing transport mechanisms or melts sea ice too aggressively for sea ice transport to occur. But it is important to remember that the sea ice loss over this time period is still noticeably less than the loss associated with the VRILE in observations (Figure 3.10).

As previously discussed, strong surface pressure gradients are associated with VRILEs (Figures 3.8 and 3.9). Therefore, the presence of a large scale high pressure system in the Pacific Ocean present in both ERA5 and the CESM2 reforecasts is notable (Figure 3.15 b, d, and f). When that high pressure system is paired with a second, smaller high pressure system in the Chukchi Sea in the 30 July 2012 reforecast the resulting surface winds are fairly weak and directed towards the Alaskan shore (Figure 3.15 d). In contrast, when there is a strong surface cyclone present, there are much stronger surface winds that are directed offshore (Figure 3.15 b and f). Taking all of this into consideration, the 6 August 2012 reforecast captures the synoptic set up for this VRILE but still does not represent the actual sea ice loss.

3.3.4 23 December 2016 VRILE

The 23 December 2016 is in the Kara Sea. In the NSIDC data, there is an expected signal for a winter VRILE: sea ice loss at the VRILE location but ice growth everywhere else (Figure 3.17 a). However, while the CAM6 run does capture sea ice loss at the VRILE

location, there is also ice loss all along the sea ice edge (Figure 3.17 c). This un-seasonal ice loss may be related to the model's two large regions of low pressure, one in the Bering Sea and the other in the Greenland, Barents, and Kara Seas. These two regions result in lower pressure over the Arctic Ocean than the surrounding land, opposite the normal pattern. These low pressure systems pull the warmer air from lower latitudes into the Arctic, likely causing the sea ice loss. While the WACCM6 reforecast does a better job of capturing sea ice behavior Arctic wide, its VRILE is still much too small (Figure 3.17 e). In their initial conditions both reforecasts have too much sea ice at the VRILE location, too little in Hudson Bay but otherwise are fairly close to NSIDC (Figure 3.18 a and c). At the time of the VRILE, both reforecasts have even more sea ice than NSIDC in that location (Figure 3.18 b and d). These patterns suggest that neither reforecasts lost enough sea ice over this time period. If they had lost a similar amount of sea ice as the VRILE in observations, we would expect to see a similar differences between the reforecasts and NSIDC at the initial conditions and at the time of the VRILE.

Both reforecasts depict the large low pressure system that stretches from the southeast coast of Greenland across the Eurasian coast (Figure 3.17 b, d, and f). However, the reforecasts also have a second, strong low-pressure system in the Bering Sea that is not present in ERA5 (Figure 3.17 b, d, and f). Additionally, ERA5 has generally high pressure over Europe and Asia, creating the typical pressure gradient associated with VRILEs (Figure 3.17 b). But both reforecasts have a low-pressure trough over parts of Russia that weaken the pressure gradient. (Figure 3.17 d and f).

There are several commonalities between these four VRILE cases. First, that CESM2 generally captures the associated surface cyclone when considering cases close enough to the start of the reforecast. The presence of these surface cyclones supports the results in the composite mean of mslp associated with VRILEs (Figures 3.8 and 3.9). However, while CESM2 generally captures the surface cyclone, it captures the observed pressure gradients less consistently. One proposed mechanism for VRILEs is heat transport by

surface cyclones. The presence of surface cyclones but general absence of VRILEs in these reforecasts suggests that heat transport by surface cyclones is insufficient to cause a VRILE. Note that while the reforecasts do often capture some sea ice loss in the correct region, it is much too small a change to truly be considered a VRILE. The missing piece may be the lack of ocean wave-sea ice dynamics. This issue is also tied into model resolution. CESM2 has a grid spacing of approximately 50 km (Kay et al. 2015), but sea ice floes and the ocean waves are on the order of 100 m. Additionally, low-level jets that can drive these ocean sea ice dynamics requires $\Delta x \approx 17 - 23$ km to resolve with peak winds occurring on even smaller scales (Guest et al. 2018). For global climate models, these resolution issues point towards a need to reevaluate how the affected processes are handled in the model's parameterization schemes.

3.4 Cyclone Properties

There are an abundance of short lived cyclones in CESM2 LENS. A total of 123,613 cyclones were located north of 60°N in model years 1980-2015. However, when these cyclones are filtered to exclude those with a lifetime less than two days the number of cyclones reduces to 34,959. This number is comparable to its ERA5 counterpart which has a total of 32,553 cyclones generated north of 60°N with the same minimum lifetime. The ERA5 and CESM2 LENS cyclones have remarkably similar probability distributions of their lifetimes (Figure 3.19 a). There is also little difference between summer cyclone lifetimes and cyclones year-round in either dataset (Figure 3.19 a).

On average, we find cyclones in CESM2 LENS to be smaller and deeper than their ERA5 counterparts (Figure 3.19 b and c). In both datasets summer cyclones are significantly weaker than the overall average (Figure 3.19 b) and slightly smaller (Figure 3.19 c). These results are consistent with climatologies of observed surface cyclones (Zhang et al. 2004; Valkonen et al. 2021). The KS statistic for cyclone lifetime is 0.139 for all cyclones and 0.146 for summer cyclones, 0.107 for all and 0.077 for summer cyclone minimum

mslp, and 0.054 for all and 0.091 for summer cyclone radii. The p-values in all cases indicate distinct distributions with a confidence of $> 99.9\%$, which is supported by the small KS statistics in all cases.

Cyclone location densities in both CESM2 LENS and ERA5 have four main centers: off the northwest coast of Greenland, along Norway's coastline, the central Arctic, and northern Siberia (Figure 3.20 a and b). Though the Siberian center is nearly split into two in CESM2 LENS (Figure 3.20 a). The main difference between CESM2 LENS and ERA5 is that surface cyclones in CESM2 LENS are more concentrated to these regions than in ERA5. These differences are highlighted in Figure 3.20 c, which shows the difference between the normalized counts. Cyclones in CESM2 LENS are more likely to be found on the northwest coast of Greenland and along the coast of Norway than those in ERA5. The location that CESM2 LENS has noticeably fewer counts than ERA5 is in Siberia.

Cyclogenesis in both datasets is concentrated near 60°N (Figure 3.21 a and b). This is likely for two reasons: the fact that the domain of the cyclone tracker was restricted north of 60°N this is where cyclogenesis is identified for cyclones that formed south of 60°N and moved into the Arctic and secondly that the Alaskan Rockies and Chersky Range in northern Russia are common sites of lee cyclogenesis (Serreze et al. 2001). CESM2 LENS overemphasizes Atlantic cyclones entering the Arctic near the southern tip of Greenland (Figure 3.21 a and c). CESM2 LENS largely misses lee cyclogenesis in the Chersky Range in Eastern Siberia (Figure 3.21 c). However, CESM2 LENS has an abundance of genesis locations east of those mountains in the Bering Sea and into Alaska (Figure 3.21 c) which could indicate a general eastward shift of cyclogenesis in that region. ERA5 has a cyclogenesis center in western Russia that is not present in CESM2 LENS (Figure 3.21).

Cyclolysis locations (Figure 3.22) are nearly identical to the heatmap of all cyclone locations (Figure 3.20). The center off the western coast of Greenland in both the total (Figure 3.20 a) and -lysis (Figure 3.22 a) plots but not in the genesis (Figure 3.21 a) plot suggests a population of cyclones in CESM2 LENS that spend most of their lives in this

location but do not form there. Since this cluster is much less prominent in ERA5, the pattern is potentially due to difficulties in CESM2 transporting the cyclones over Greenland's topography. The lack of a cluster of lysis points at or near 60°N does suggest that once cyclones are in the Arctic, they are rarely transported out. Otherwise, the similarities between the lysis locations and all cyclone locations suggests that there are no preferential locations for cyclolysis in either CESM2 LENS or ERA5.

3.5 Summary

In this chapter we find that CESM2 LENS has a negative bias in sea ice extent in all seasons (Figures 3.1 and 3.2), no significant sea ice loss at synoptic time scales (Figure 3.3), and that VRILEs are smaller than observations by an order of magnitude in all seasons and regions (Figure 3.6). The overall negative sea ice bias is consistent with previous studies (Keen et al. 2021; DeRepentigny et al. 2020; DuVivier et al. 2020, e.g.) while the subseasonal discrepancies have not been addressed in prior literature. This size discrepancy remains even in subseasonal reforecast runs (Figure 3.10). Additionally we find that both September and March sea ice extent in CESM2 has a similar degree of interannual variability as observations. This is a somewhat surprising result as VRILEs are thought to play a role in that interannual variability. Upon investigation we find that the variability in CESM2 LENS exhibits minimal spatial variability as compared to observations (Figure 3.5) and that it is likely driven by internal model variability though there may be a connection to the Arctic Oscillation (Figure 3.4). While the spatial variability of Arctic sea ice is not widely documented, Peng and Meier (2018) provides a record for the annual cycles of Arctic sea ice divided into 15 different regions. Additionally, spatial variability in observational datasets is shown to be primarily related to the Arctic Oscillation (Stroeve et al. 2008).

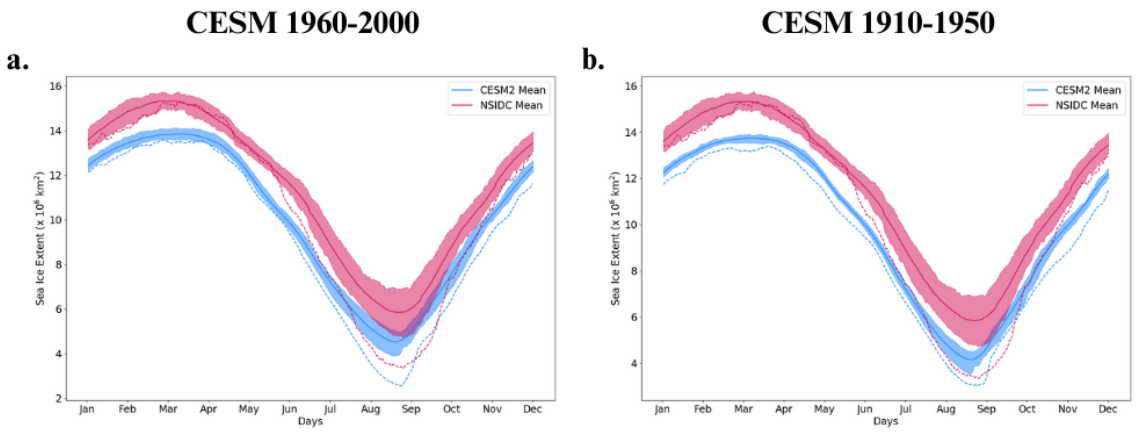


Figure 3.1: Monthly average sea ice extent for CESM2 LENS (pink) and NSIDC (blue). Mean values are plotted with a solid line. The year with the minimum September extent are plotted as the dotted lines. Shading indicates the inner quartile range. The NSIDC data in a and b is from 1980-2022 while a uses CESM2 LENS data from 1960-2000 and b shows 1910-1950.

Comparisons of sea ice and cyclone properties between CESM2 LENS, NSIDC, and ERA5 show that CESM2 LENS does a good job of representing surface cyclones, connects those cyclones to synoptic timescale sea ice loss, but does not adequately represent the changes in sea ice at those scales. Recall that there are three primary proposed mechanisms for VRILES: temperature and moisture transport, ocean wave dynamics, and ocean heating via vertical mixing. CESM2 LENS and S2S reforecasts both adequately capture cyclone activity, the most likely mechanism for poleward heat and moisture transport. This is supported by other studies on moisture transport in CESM2 (Benedict et al. 2019) and its representation of cyclones (Song et al. 2021; Karwat et al. 2024). If CESM2 captures poleward heat and moisture transport correctly but that transport does not result in significant sea ice loss it points to one or both of the ocean processes as the driver behind VRILEs.

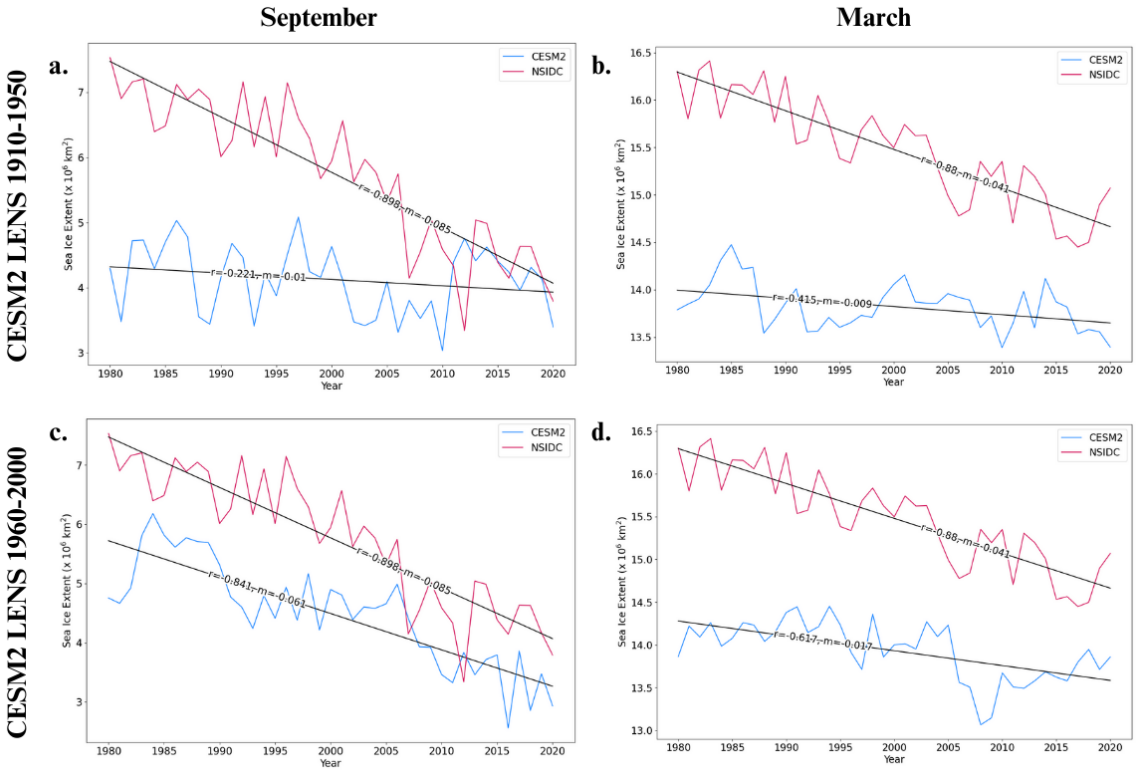


Figure 3.2: September minimum and March maximum sea ice extent for CESM2 LENS (blue) and NSIDC (pink). In a and b, CESM2 LENS data is from 1910-1950 and from 1960-2000 in b and d. NSIDC data is from 1980-2020 in both and CESM2 LENS data has been plotted against the same date range as the NSIDC data for ease of comparison. The black lines show the linear trend in each dataset with their associated r value and slope displayed inline.

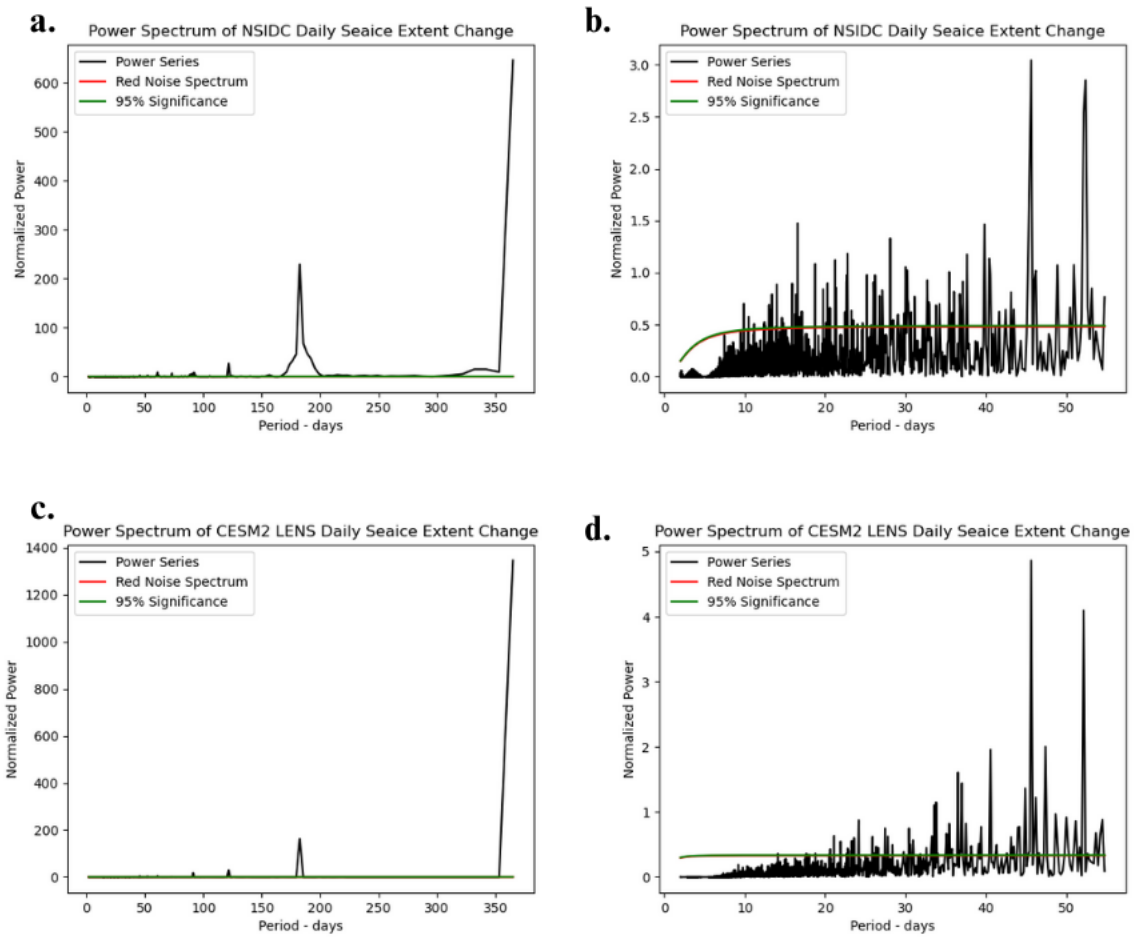


Figure 3.3: Normalized power as a function of period of the daily change in sea ice extent in NSIDC (a-b) and CESM2 LENS (c-d). The power spectrum is plotted in black, the red noise spectrum in red, and the 95% significance level in green. Panels (a) and (c) show the power spectrum out to 365 days while panels (b) and (d) are limited to shorter timescales.

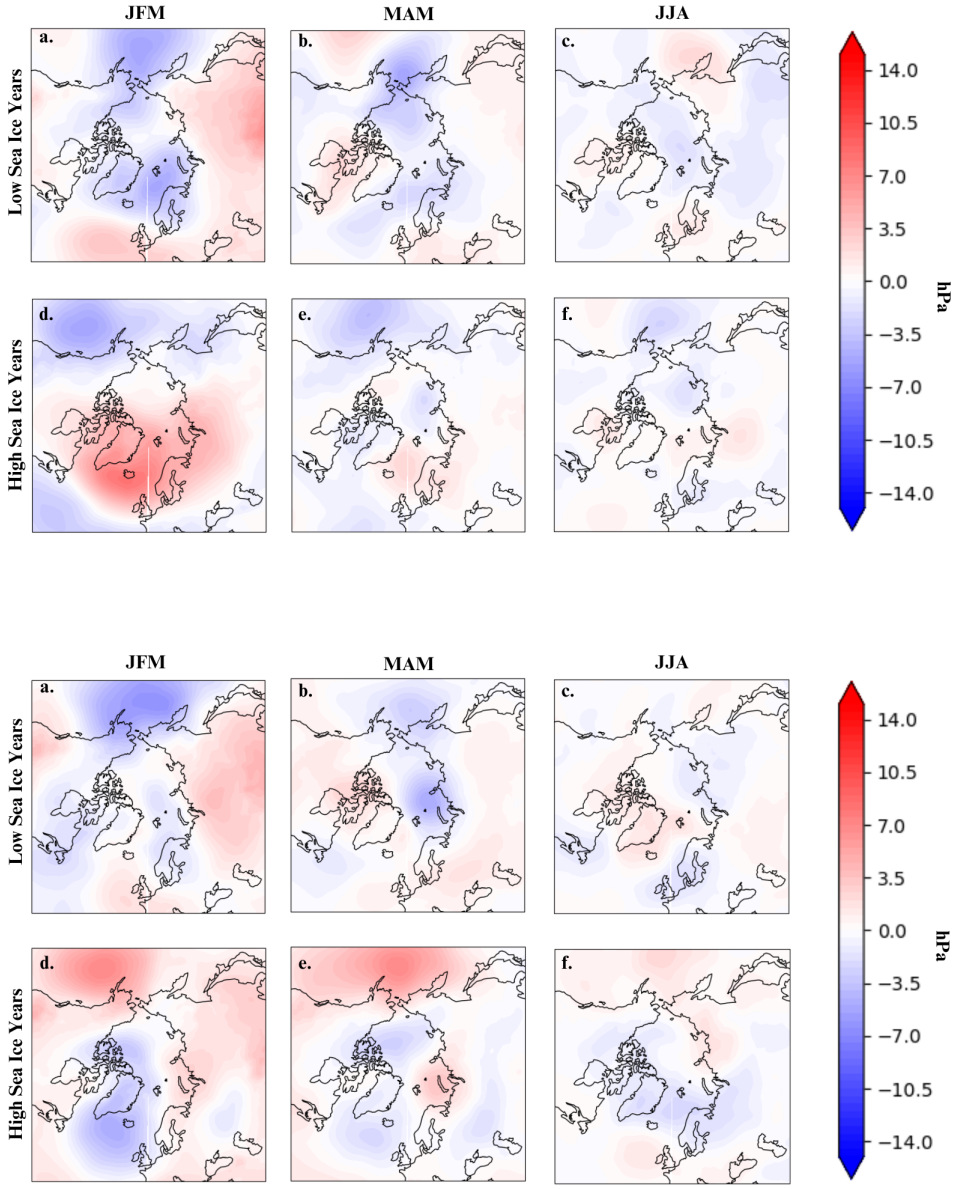


Figure 3.4: Composite mean of seasonal mean mslp of the five highest and lowest September sea ice minima with respect to the climate trend in CESM2 LENS. The top panel uses data from model years 1910-1950 and the bottom is for model years 1960-2000. In both panels, the left most column is January, February, and March (JFM), the middle column March, April, and May (MAM) and the right column for June, July, and August (JJA).

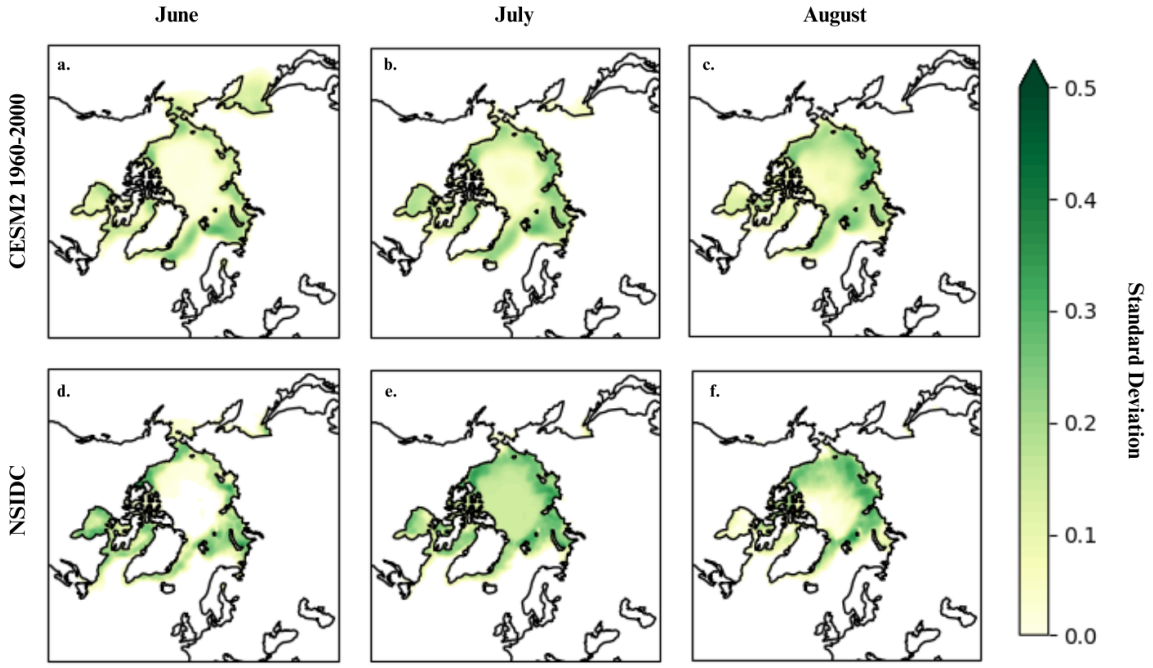


Figure 3.5: Standard deviation of monthly average sea ice concentration in CESM2 LENS and NSIDC. Panels (a-c) are the June, July, and August monthly sea ice concentration standard deviations in CESM2 LENS data from 1960-2000 respectively. Panels (d-f) show the June, July, and August sea ice concentration standard deviations in NSIDC data.

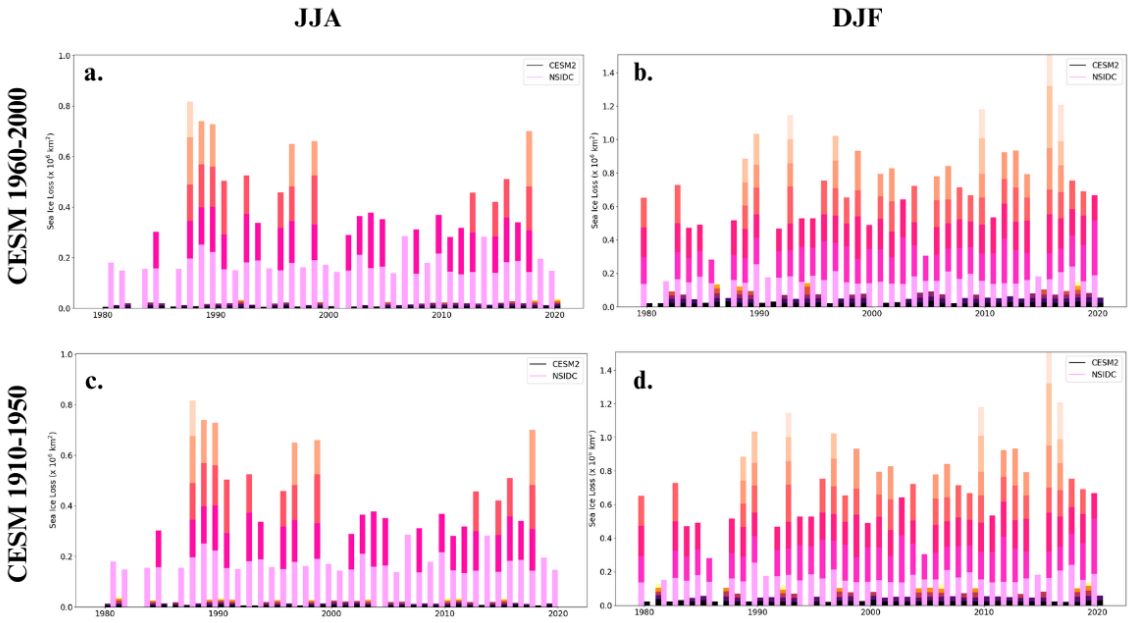


Figure 3.6: VRILE size by year in NSIDC (pinks) and CESM2 (blues) for summer (jja) in a and c and winter (djf) in b and d. In years with multiple VRILEs, the sea ice losses are vertically stacked and each color represents a unique VRILE. Figures a and b use CESM2 data from 1960-2000 while c and d use 1910-1950.

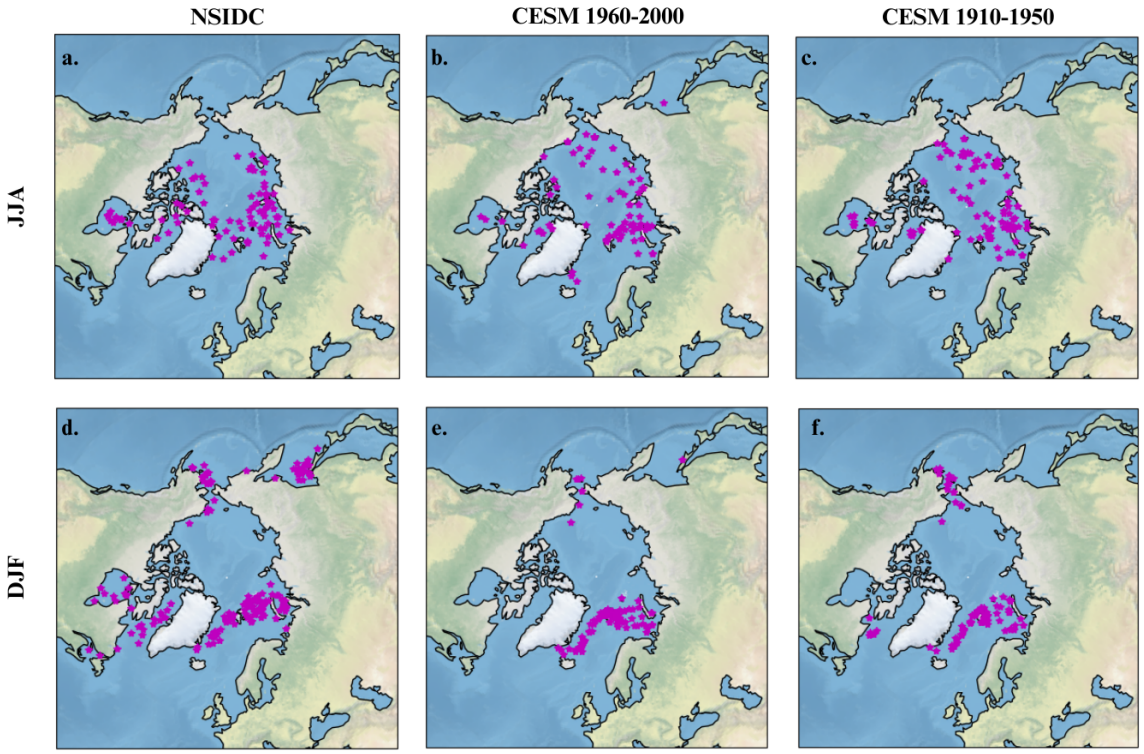


Figure 3.7: Location of VRILEs in NSIDC and CESM2 LENS datasets. Panels (a) and (d) respectively show the location of summer (jja) and winter (djf) VRILEs in NSIDC data. Panels (b) and (e) respectively show the locations of summer (jja) and winter (djf) VRILES in CESM2 LENS data from 1960-2000. Panels (c) and (f) respectively show the locations of summer (jja) and winter (djf) VRILEs in CESM2 LENS data from 1910-1950.

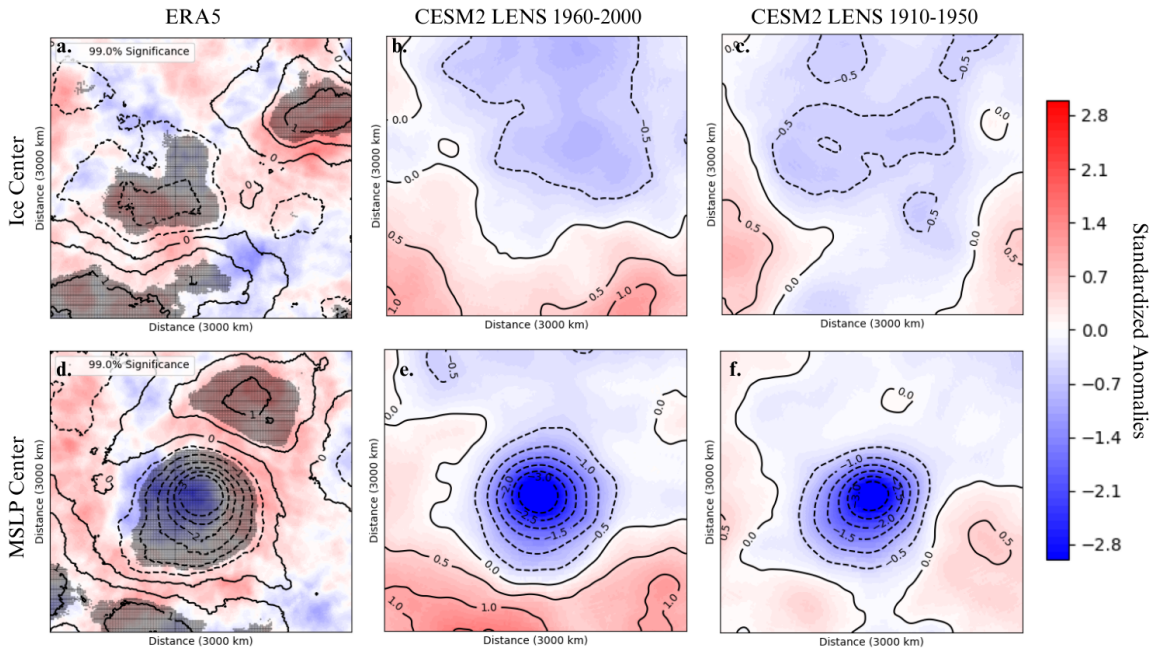


Figure 3.8: Composite mean of mslp for summer (jja) VRILEs centered on VRILE location (a-c) and closest local minimum in mslp to the VRILE location (d-f). Panels (a) and (d) utilize ERA5 data and are based on VRILEs found in NSIDC sea ice extent. Additionally, in these panels potential temperature on the dynamic tropopause (2 PVU surface) is shown by the colorfill and stippling indicates statistical significance at $> 99\%$ in the mslp field. In panels b, c, e, and f, only mslp is shown in both the contours and colorfill. Units for all fields are standardized anomalies. Panels (b) and (e) are generated from CESM2 LENS data from 1960-2000 and panels (c) and (f) are generated from CESM2 LENS years 1910-1950.

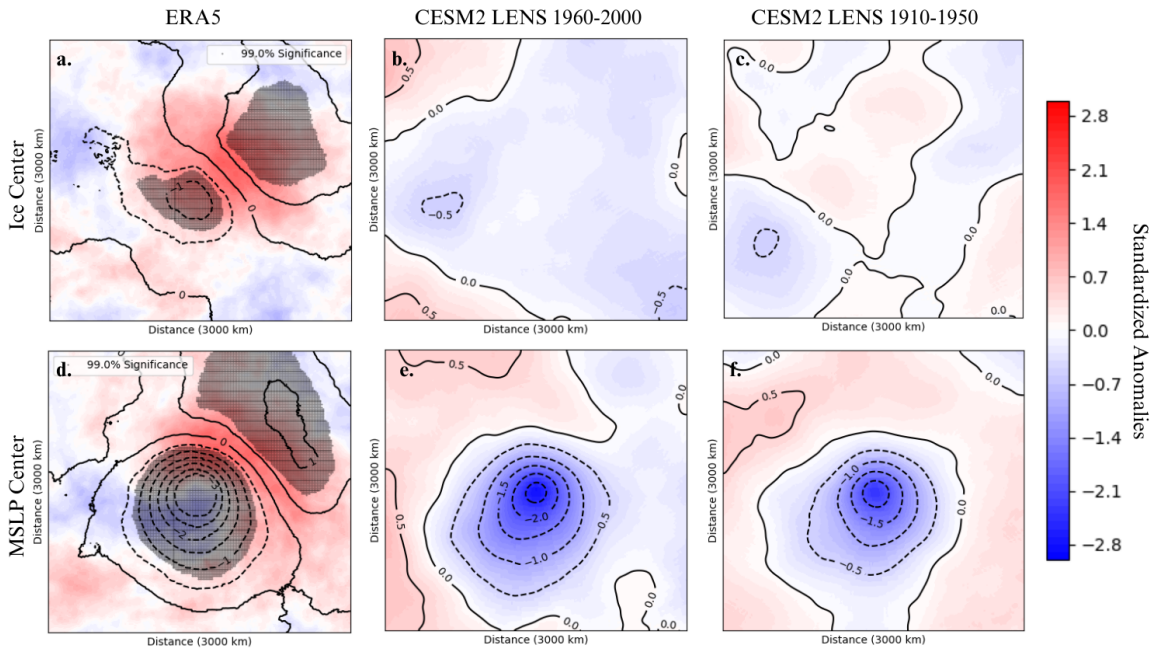


Figure 3.9: Composite mean of mslp for winter (djf) VRILEs centered on VRILE location (a-c) and closest local minimum in mslp to the VRILE location (d-f). Panels (a) and (d) utilize ERA5 data and are based on VRILEs found in NSIDC sea ice extent. Additionally, in these panels potential temperature on the dynamic tropopause (2 PVU surface) is shown by the colorfill and stippling indicates statistical significance at $> 99\%$ in the mslp field. In panels b, c, e, and f, only mslp is shown in both the contours and colorfill. Units for all fields are standardized anomalies. Panels (b) and (e) are generated from CESM2 LENS data from 1960-2000 and panels (c) and (f) are generated from CESM2 LENS years 1910-1950.

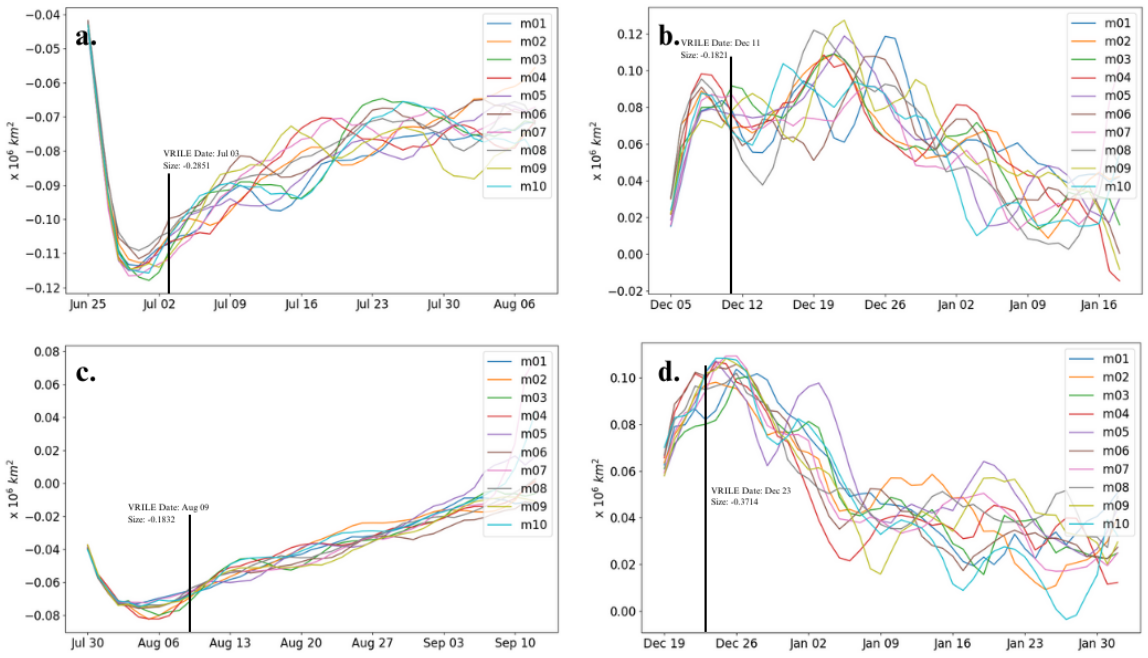


Figure 3.10: Daily sea ice extent change of the ten member reforecasts used to analyze four VRILE cases. The day of the VRILE and the sea ice loss associated with it it marked on each plot with a black line. Panel (a) is for the VRILE that occurred on 3 July, 2007 and the reforecast initialized on 25 June, 2007. Panel (b) is for the VRILE that occurred on 11 December, 2011 and the reforecast initialized on 5 December, 2011. Panel (c) is for the VRILE that occurred on 9 August, 2012 and the reforecast initialized on 30 July, 2012. Panel (d) is for the VRILE that occurred on 23 December, 2016 and the reforecast initialized on 19 December, 2016.

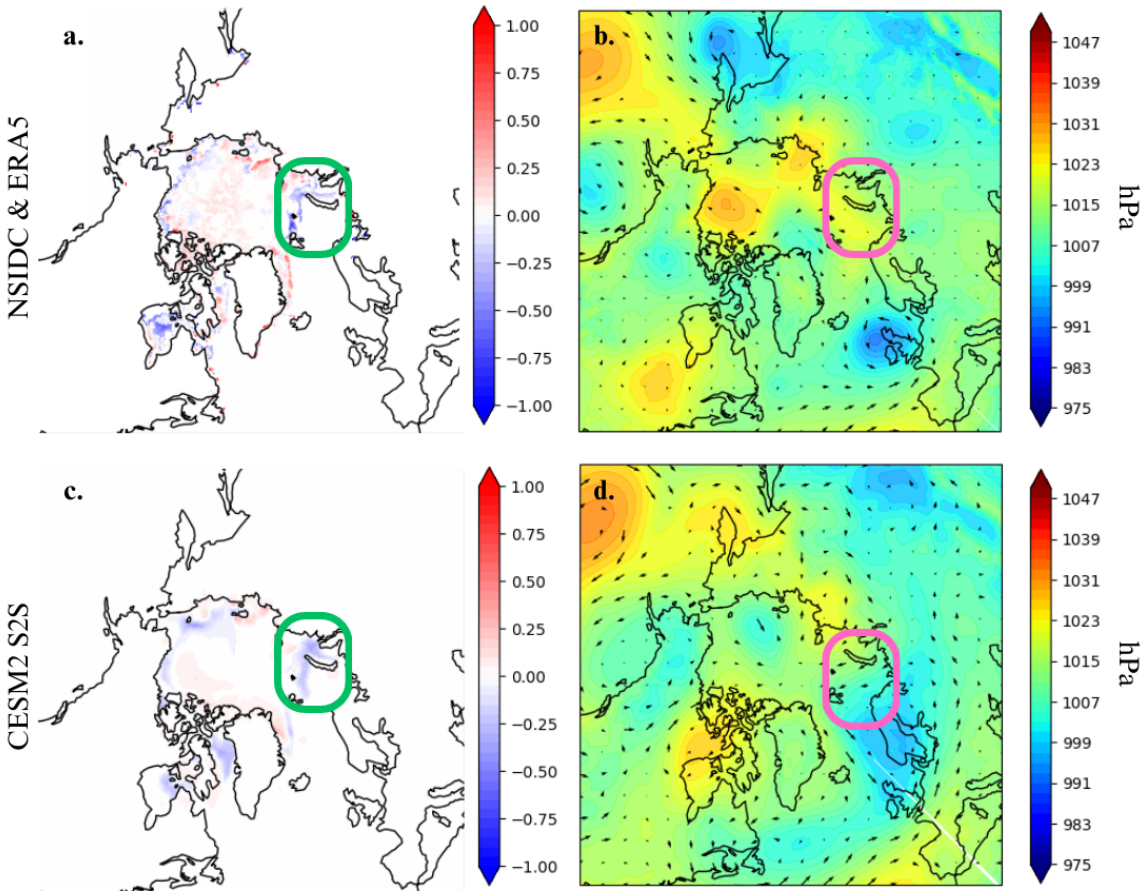


Figure 3.11: Five day change in sea ice concentration (a, c) and five day mean in mslp and 10 meter winds (b, d) for the 3 July 2007 VRILE. The location of the VRILE is circled on each panel. Panel (a) shows the difference in NSIDC sea ice concentration between 3 July 2007 and 28 June 2007. Panel (b) is the average mslp and 10 m winds for the same time period as (a) using ERA5 data. Panel (c) shows the difference in CESM2 S2S sea ice concentration between 3 July 2007 and 28 June 2007 from the reforecast initialized on 25 June 2007. Panel (d) is the average mslp and 10-m wind from the same reforecast and time period as in (c).

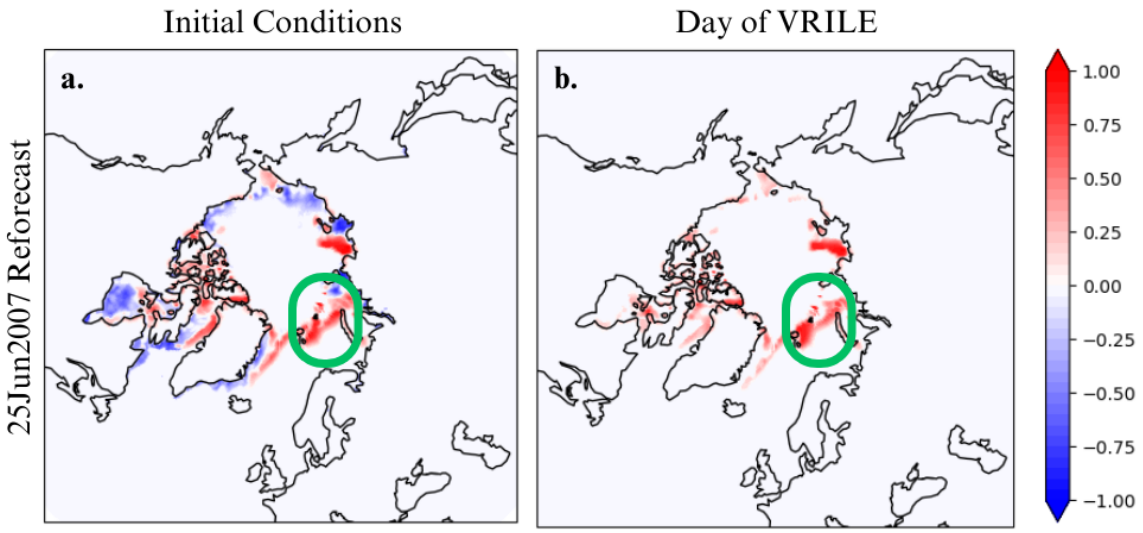


Figure 3.12: Difference in sea ice concentration in CESM2 S2S and NSIDC for the 3 July 2007 VRILE. The VRILE location is circled in green in both panels. Positive (Negative) values, shown in red (blue), indicate too much (little) sea ice in CESM2 in comparison to NSIDC. Panel (a) shows the difference in sea ice concentration on the day the CESM2 S2S reforecast was initialized, 25 June 2007, and panel (b) shows the difference on the day of the VRILE, 3 July 2007.

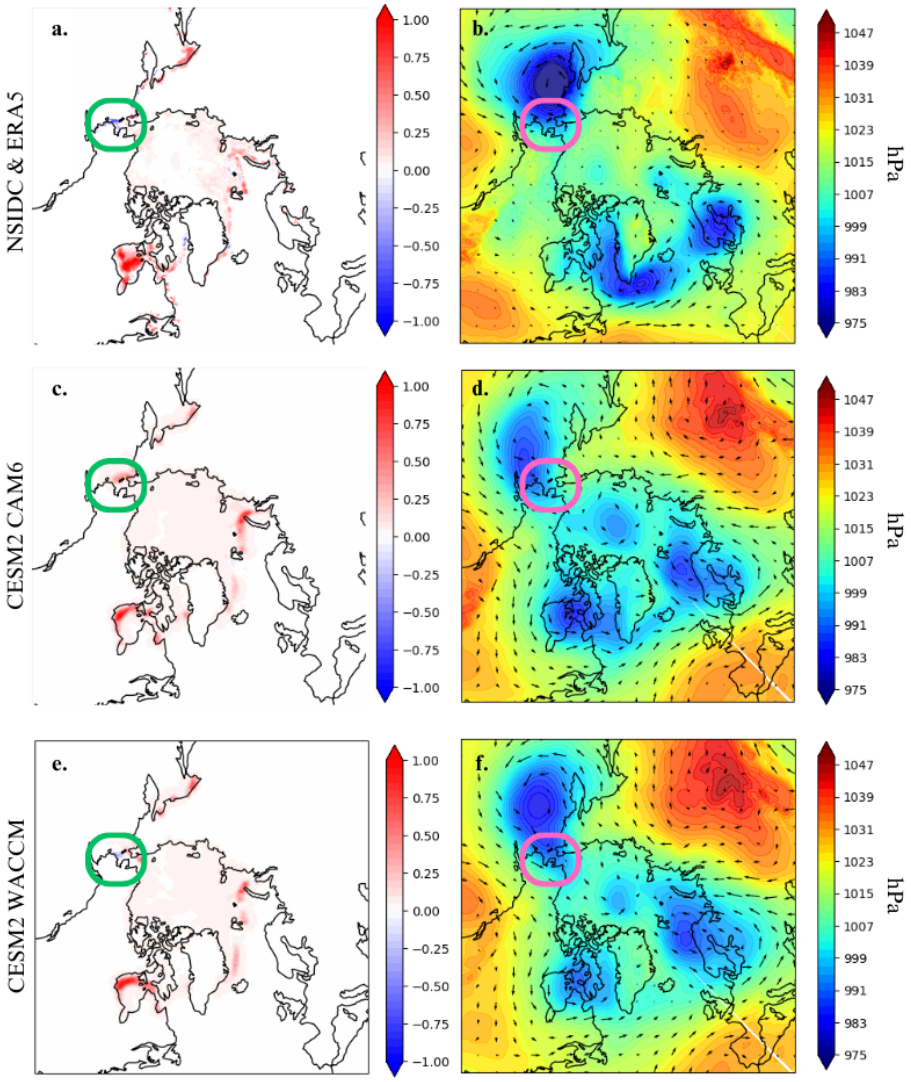


Figure 3.13: Five day change in sea ice concentration (a, c) and five day mean in mslp and 10 meter winds (b, d) for the 11 December 2011 VRILE. The location of the VRILE is circled on each panel. Panel (a) shows the difference in NSIDC sea ice concentration between 11 December 2011 and 6 December 2011. Panel (b) is the average mslp and 10 m winds for the same time period as (a) using ERA5 data. Panel (c) shows the difference in CESM2 S2S sea ice concentration between 11 December 2011 and 6 December 2011 from the reforecast initialized on 5 December 2011. Panel (d) is the average mslp and 10-m wind from the same reforecast and time period as in (c). Panels (e) and (f) are as (c) and (d) except WACCM6 was used at the atmospheric component in CESM2.

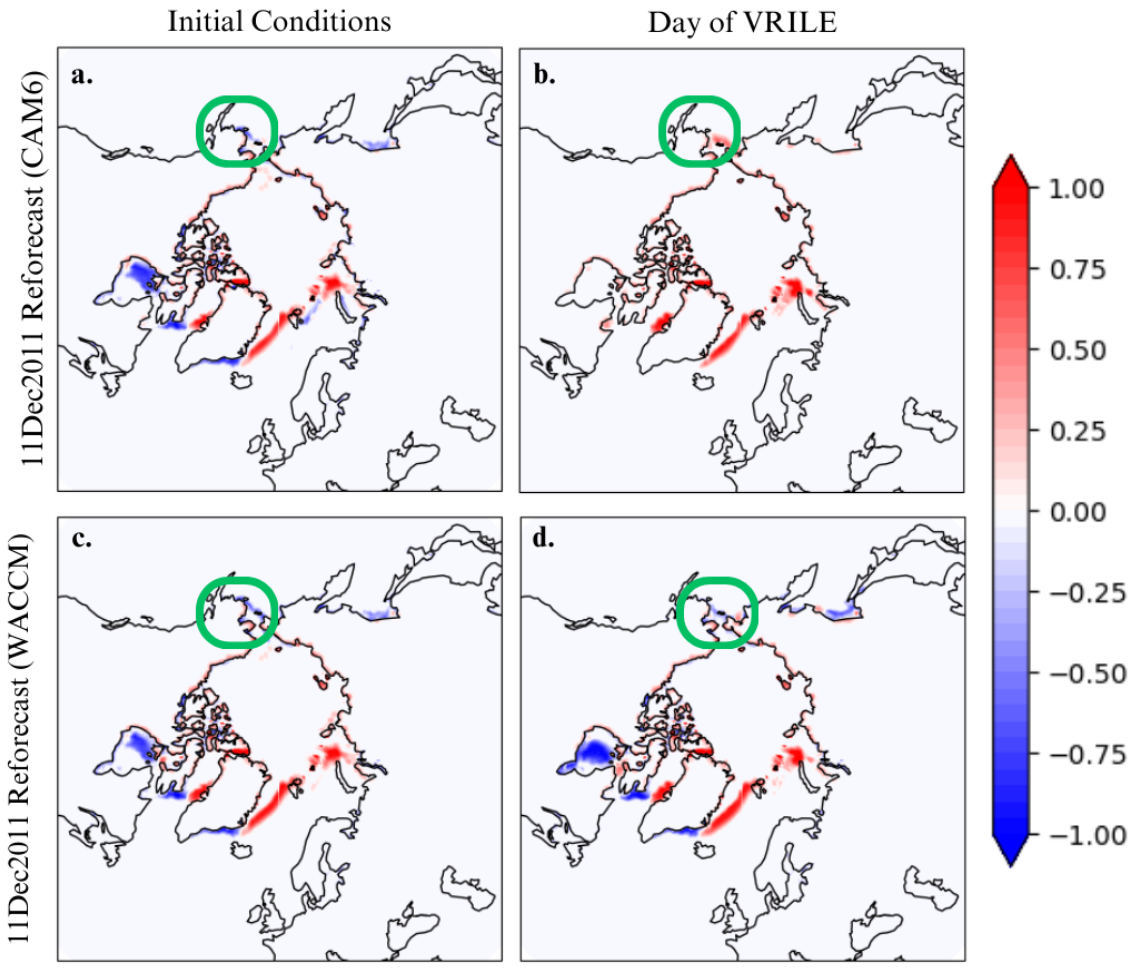


Figure 3.14: Difference in sea ice concentration in CESM2 S2S and NSIDC for the 11 December 2011 VRILE. The VRILE location is circled in green in both panels. Positive (Negative) values, shown in red (blue), indicate too much (little) sea ice in CESM2 in comparison to NSIDC. Panel (a) shows the difference in sea ice concentration on the day the CESM2 S2S reforecast was initialized, 5 December 2011, and panel (b) shows the difference on the day of the VRILE, 11 December 2011. Panels (c) and (d) are as (a) and (b) except WACCM6 was used at the atmospheric component in CESM2.

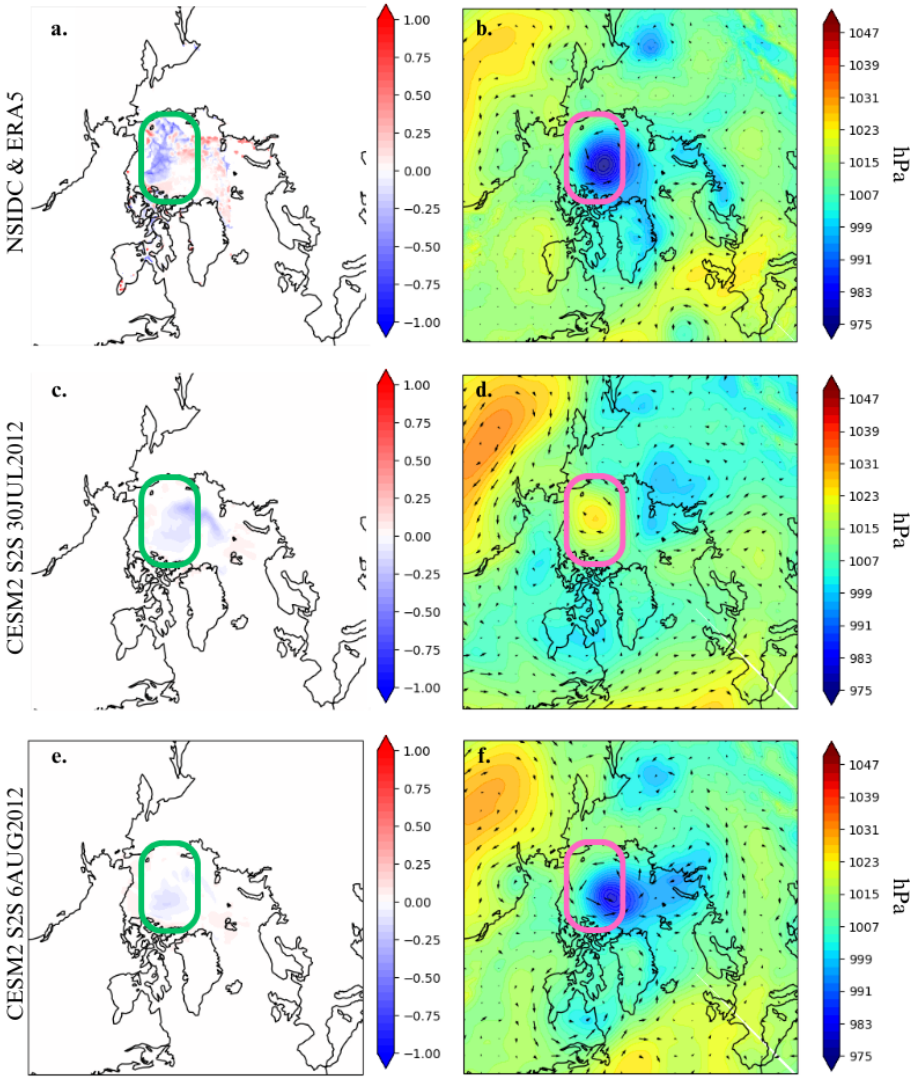


Figure 3.15: Five day change in sea ice concentration (a, c) and five day mean in mslp and 10 meter winds (b, d) for the 9 August 2012 VRILE. The location of the VRILE is circled on each panel. Panel (a) shows the difference in NSIDC sea ice concentration between 9 August 2012 and 4 August 2012. Panel (b) is the average mslp and 10 m winds for the same time period as (a) using ERA5 data. Panel (c) shows the difference in CESM2 S2S sea ice concentration between 9 August 2012 and 9 August 2012 from the reforecast initialized on 30 July 2012. Panel (d) is the average mslp and 10-m wind from the same reforecast and time period as in (c). Panels (e) and (f) are as (c) and (d) for the reforecast initialted on 6 August 2012.

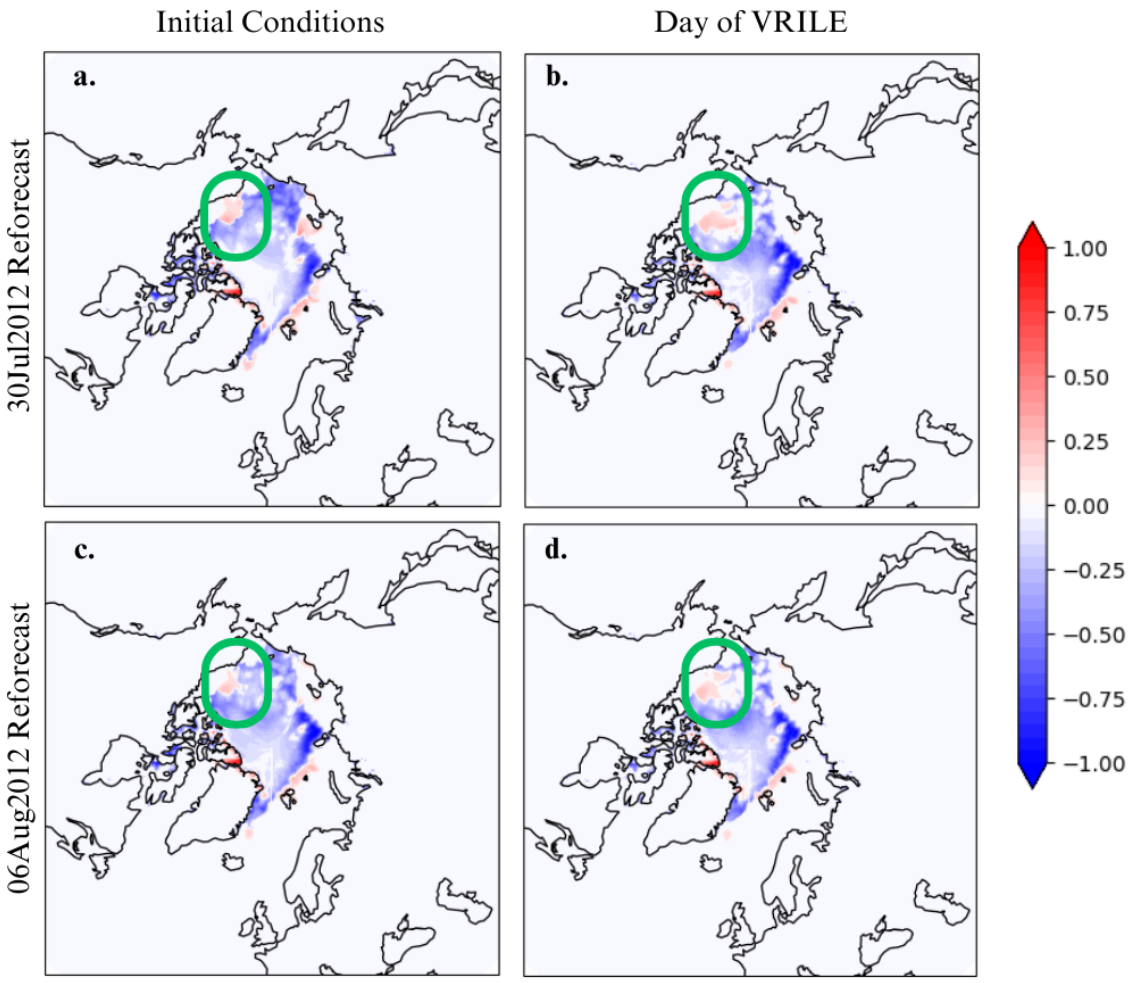


Figure 3.16: Difference in sea ice concentration in CESM2 S2S and NSIDC for the 9 August 2012 VRILE from the reforecasts initialized on 30 July 2012 and 6 August 2012. The VRILE location is circled in green in all four panels. Positive (Negative) values, shown in red (blue), indicate too much (little) sea ice in CESM2 in comparison to NSIDC. Panel (a) shows the difference in sea ice concentration on the day the CESM2 S2S reforecast was initialized, 30 July 2012, and panel (b) shows the difference on the day of the VRILE, 9 August 2012. Panel (c) shows the difference in sea ice concentration on the day the 6 August 2012 reforecast was initialized and panel (d) shows the difference on the day of the VRILE for that reforecast.

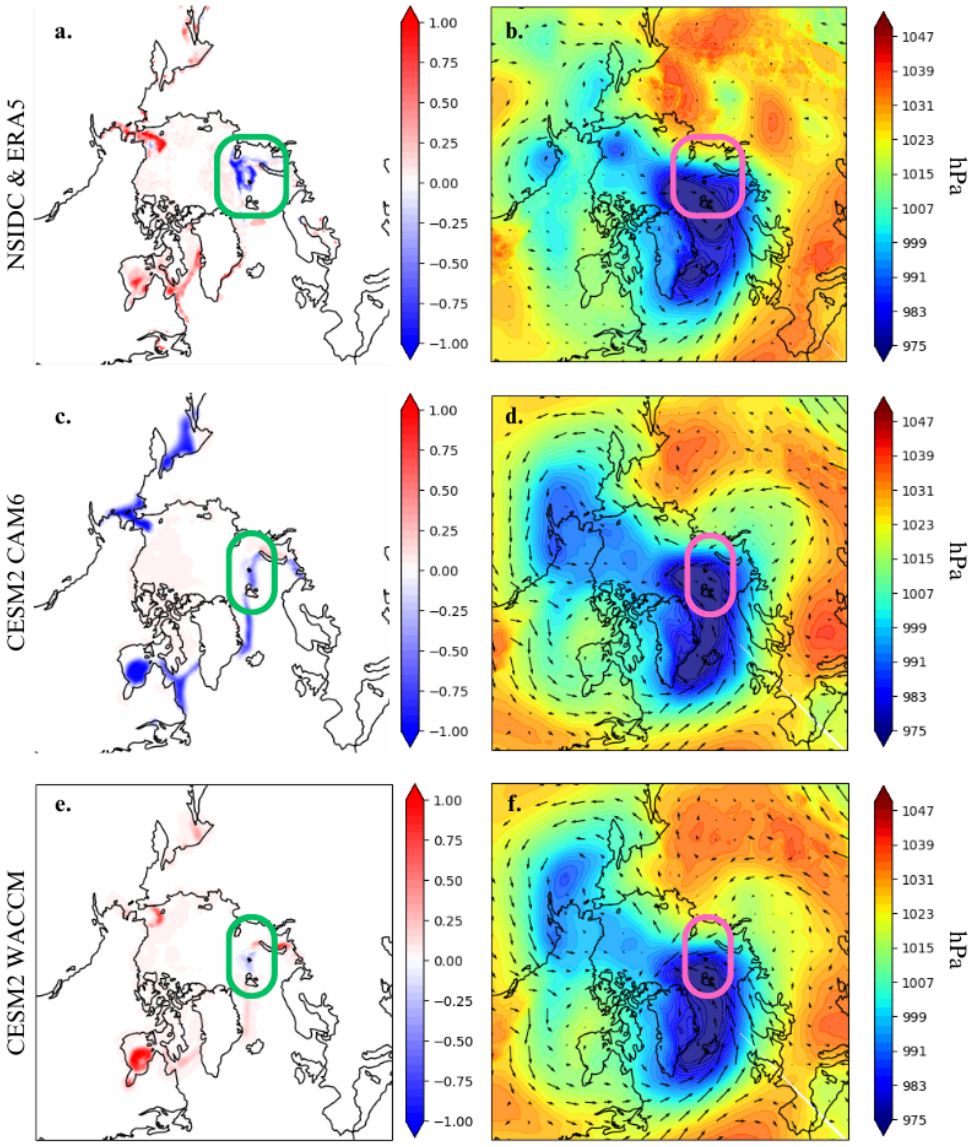


Figure 3.17: Five day change in sea ice concentration (a, c) and five day mean in mslp and 10 meter winds (b, d) for the 23 December 2016 VRILE. The location of the VRILE is circled on each panel. Panel (a) shows the difference in NSIDC sea ice concentration between 23 December 2016 and 18 December 2016. Panel (b) is the average mslp and 10 m winds for the same time period as (a) using ERA5 data. Panel (c) shows the difference in CESM2 S2S sea ice concentration between 23 December 2016 and 19 December 2016 from the reforecast initialized on 19 December 2016. Panel (d) is the average mslp and 10-m wind from the same reforecast and time period as in (c). Panels (e) and (f) are as (c) and (d) except WACCM6 was used at the atmospheric component in CESM2.

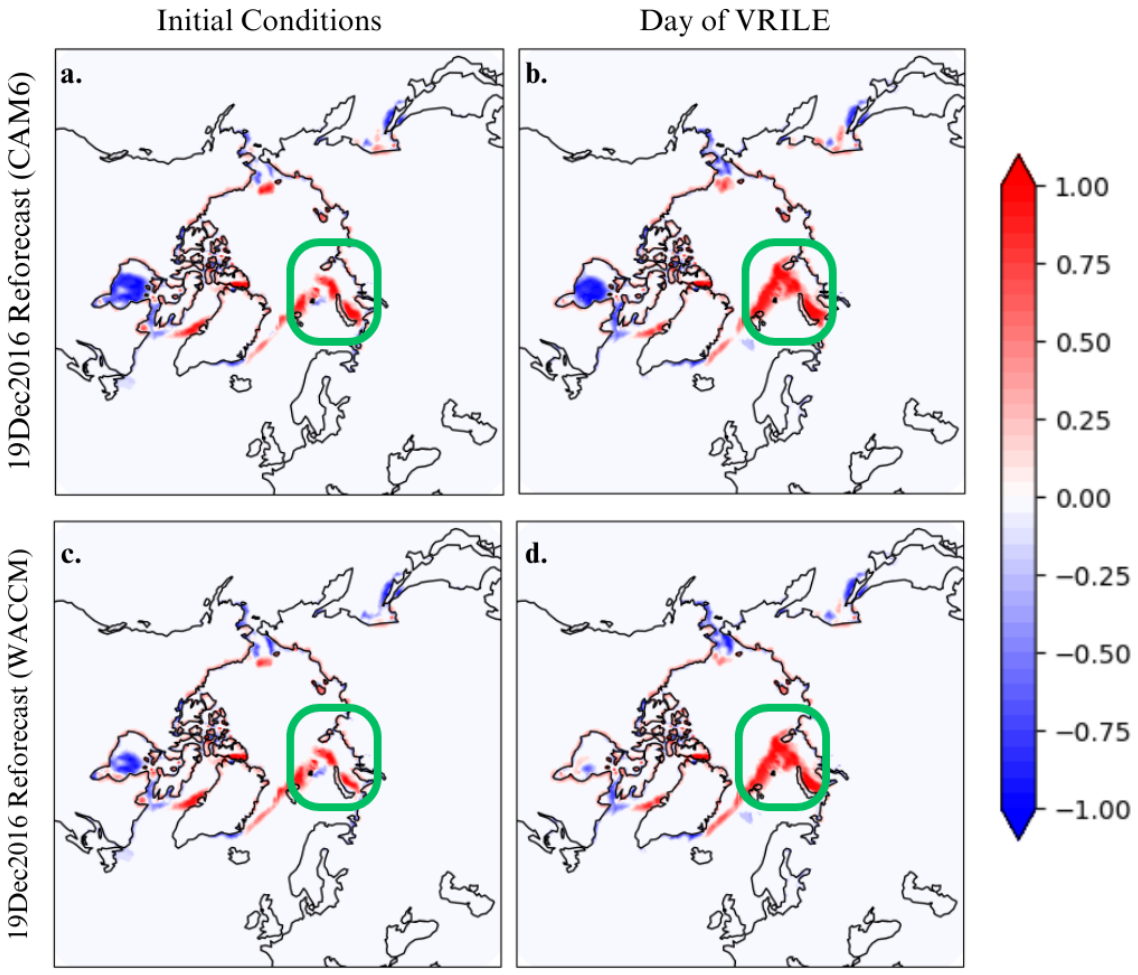


Figure 3.18: Difference in sea ice concentration in CESM2 S2S and NSIDC for the 23 December 2016 VRILE. The VRILE location is circled in green in both panels.Positive (Negative) values, shown in red (blue), indicate too much (little) sea ice in CESM2 in comparison to NSIDC. Panel (a) shows the difference in sea ice concentration on the day the CESM2 S2S reforecast was initialized, 19 December 2016, and panel (b) shows the difference on the day of the VRILE, 23 December 2016. Panels (c) and (d) are as (a) and (b) except WACCM6 was used at the atmospheric component in CESM2.

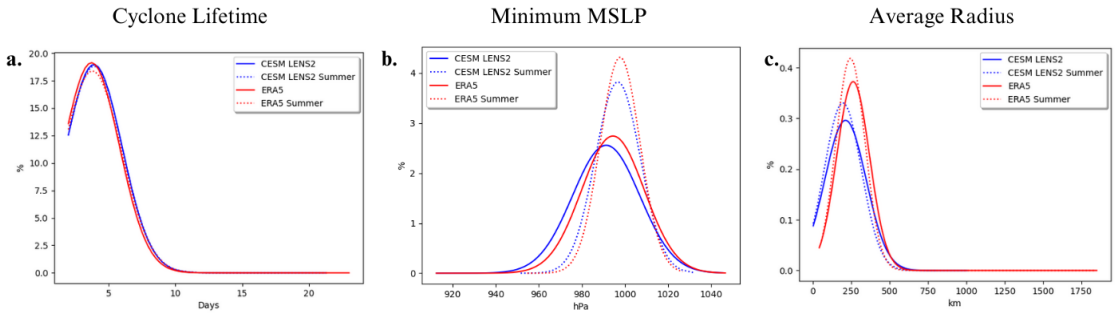


Figure 3.19: Probability density functions (PDF) of surface cyclones in CESM2 LENS and ERA5 of cyclone lifetime (a), minimum mslp (b) and average radius (c). CESM2 LENS data is plotted in blue and ERA5 in red. Solid lines correspond to the PDF of all cyclones while dashed lines correspond to summer cyclones (jja) only. Per the KS test, all CESM2 LENS distributions are significantly different from their ERA5 counterparts with greater than 99.9% confidence.

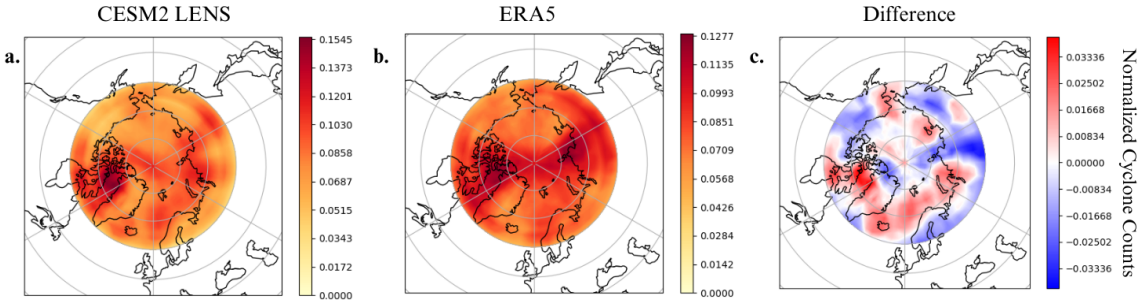


Figure 3.20: Density map of normalized cyclone location counts in CESM2 LENS (a) and ERA5 (b) and the difference, CESM2 LENS - ERA5, between them (c).

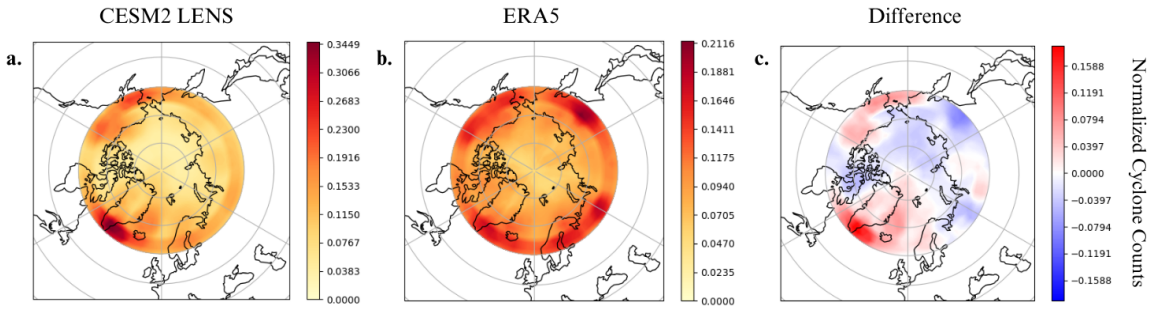


Figure 3.21: Density maps of normalized cyclogenesis location counts in CESM2 LENS (a) and ERA5 (b) and the difference, CESM2 LENS - ERA5, between them (c).

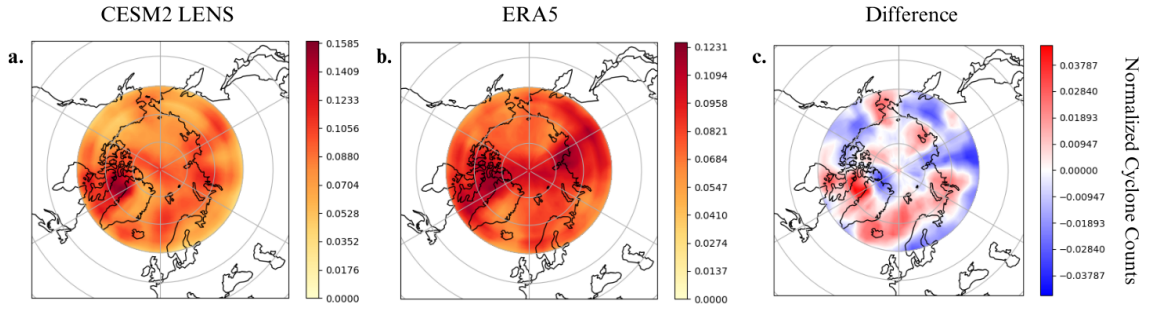


Figure 3.22: Density maps of normalized cyclolysis counts in CESM2 LENS (a) and ERA5 (b) and the difference, CESM2 LENS - ERA5, between them (c).

Chapter 4

Statistical Analysis of Proposed VRILE Drivers

The physical mechanism or mechanisms behind VRILEs is currently unknown. Identifying these mechanisms and their relative importance is crucial to addressing their representation in climate models. As discussed in Chapters 1 and 3, we know that when VRILEs occur, there tends to be a strong surface pressure gradient at the location of the sea ice loss. This fact suggests two potential mechanisms as their cause: heat transport from lower latitudes and mechanical forcing from wind driven ocean waves. Here, we take a statistical approach to understanding the relative importance of these mechanisms. Multivatiate EOFs can identify related spatial patterns between two or more datasets making it an appropriate tool for our purposes.

4.1 Root Mean Square Covariance

The root mean square covariance between the fields of interest, significant height of wind waves, surface mean latent heat flux and 2-m temperature, gives some insight into the importance of each factor. It is generally considered best practice to move forward with EOF analysis for related spatial patterns only if the RMSC is at least 0.1. The RMSC is also used to look at time-lagged relationships and determine which factors to consider in the multivariate EOF analysis. This is especially important in determining which terms available in ERA5 best captured the relationship between sea ice concentration and ocean waves. While ultimately we use significant height of wind waves in the EOFs , we initially considered normalized kinetic energy into waves and significant height of wind waves with swell as well. We choose to move forward with significant height of wind waves because it has the highest RMSC of the three. There are differences when the atmospheric field is lagged relative to sea ice concentration, but there are not consistent patterns between

variables, seasons, or regions except that the RMSC is larger in all cases when a five day running mean is applied to the data. This relationship informs how the data is pre-processed for the EOFs.

The RMSC values for significant height of wind waves, surface mean latent heat flux, and 2-m temperature in both regions and seasons range from 0.188 - 0.323 (Table 4.1). These values indicate that further analysis of these terms is warranted. However, the RMSCs alone do not give any clear indicators of the overall relative importance between the terms. In fact, the variability in RMSC may indicate that different factors are more or less important based on season and region. We discuss these differences moving forward in this chapter as we perform more in-depth analyses.

4.2 Multivariate EOF Analysis of Individual Atmospheric and Ocean Fields

In this section, we analyze the leading modes of variability of 2-m temperature, mean surface latent heat flux, and significant height of wind waves. This analysis addresses the total covariance between each of these fields and the daily change in sea ice concentration. Furthermore, we consider the physical basis behind the resulting signals.

The results of our Multivariate EOF analysis are presented as the applicable principal component timeseries regressed onto the sea ice field. The output is interpreted as the sea ice response to the atmospheric or oceanic field of interest. Positive values, shown in red in the output maps, are interpreted as direct variation with the input field while negative values, shown in blue, represent indirect variation. For example, if the leading mode of variability associated with 2-m temperature is negative (blue) everywhere, that is interpreted as sea ice loss associated with warm temperatures anomalies or sea ice gain with cold temperature anomalies. Since the results are presented this way, the resulting spatial patterns should be thought of at the sea ice response to the atmospheric or ocean field.

Root Mean Square Covariance							
			Lag 0	Lag 1	Lag 2	Lag 3	Smoothed
Significant Height of Wind Waves	Atlantic	JJA	0.179	0.177	0.176	0.176	0.235
		DJF	0.127	0.130	0.128	0.124	0.188
	Pacific	JJA	0.160	0.158	0.154	0.151	0.213
		DJF	0.262	0.257	0.258	0.264	0.314
Surface Mean Latent Heat Flux	Atlantic	JJA	0.100	0.102	0.101	0.099	0.163
		DJF	0.108	0.116	0.120	0.120	0.166
	Pacific	JJA	0.113	0.112	0.108	0.101	0.176
		DJF	0.163	0.166	0.165	0.156	0.233
2-m Temperature	Atlantic	JJA	0.194	0.196	0.193	0.187	0.254
		DJF	0.145	0.147	0.140	0.126	0.188
	Pacific	JJA	0.248	0.247	0.237	0.224	0.323
		DJF	0.184	0.179	0.166	0.151	0.236

Table 4.1: Table of RMSC values for significant height of wind waves, surface mean latent heat flux, and 2-m temperature.

For each of the Multivariate EOFs, we present the four leading modes. We chose four after considering the percent variance explained by each mode for each of the regions and seasons of interest (Figures 4.1 and 4.2). While there are not four independent modes for each season and region, the fourth mode maybe important in some of the some of the EOFs (e.g. Figure 4.1 f, 4.2 b, c, and d). We present four modes for each season and region for consistency.

The discussion of the modes of variability is presented with the a priori knowledge of how each of the factors can influence sea ice as discussed in Chapter 1. We do not suggest that ours are the sole interpretations of the resulting signals but rather one plausible explanation of the physical processes captured by the analysis. Our aim in this section is to see if the leading modes of co-variability between sea ice concentration and 2-m temperature, significant height of wind waves, and surface latent heat flux are consistent with the pressure gradient and surface cyclone associated with VRILEs seen in Figures 3.8 and 3.9.

4.2.0.1 Pacific Region JJA

The sea ice response to the significant height of wind waves appears to show a transport signal (Figure 4.3). When wind-driven ocean waves are larger than normal, there is widespread sea ice loss along the northern coastlines of Alaska and Siberia and sea ice gain in the central Arctic. The second leading mode is quite similar to the first but with an additional region of ice loss in the central Arctic (Figure 4.3 b). We suspect that the tripole in the second mode is a mathematical artifact rather than representative of a physical process and that the part of the signal that is ice loss near the sea ice edge and gain poleward is the same physical mechanism captured in the first mode. We interpret these signals as resulting from surface cyclones interacting with the Beaufort High driving strong poleward winds that induce the requisite above average waves, breaking up sea ice in the MIZ, and transporting it poleward (Figure 4.4). The third mode is much noisier than the first and

second but may be capturing further aspects of the dominant transport mode (Figure 4.3 c). Finally, the fourth mode generally indicates sea ice loss with larger than average wind waves (Figure 4.3 d). If the relationship between sea ice loss and wind waves was simply that larger waves lead to more loss, this is the type of signal we would expect to see in the leading modes. However, our analysis may be capturing differences in how sea ice is affected by wind waves in the early versus late summer. In late summer, when ice is at its thinnest, sea ice is more susceptible to destruction from wind waves than the thicker ice of the late spring and early summer. These differences could account for the transport signal dominating the EOFs.

In order to interpret sea ice response to mean surface latent heat (LH) flux, note that ERA5 defines positive fluxes to be downwards (Hersbach et al. 2020). Consequently, a negative latent heat flux is achieved when LH is transported from the ocean to the atmosphere. Consider the scenario proposed in Figure 4.5, where there is open ocean between ice floes or large melt ponds on the ice. This setup, along with clear sky conditions, results in a negative LH flux. With a negative LH flux, the large red region in the central Arctic in Figure 4.6 corresponds to sea ice loss. In fact, such a signal dominates the four leading modes we analyzed (Figure 4.6.) Physically, this setup could correspond to a persistent and strong Beaufort High leading to clear skies and increased shortwave radiation resulting in increased sea ice melt (Figure 4.5). This setup is consistent with previous studies that find that anonymously low sea ice years have fewer storms in the early summer as compared to high sea ice years (Screen et al. 2011).

The sea ice response to 2-m temperature is likely non-physical. The leading mode of variability indicates that with a warmer than average Arctic there is sea ice gain in some regions but loss in others (Figure 4.7 a). Therefore, this signal, while mathematically significant, is unlikely to represent a physically significant one. The second leading mode (Figure 4.6 b) indicates poleward transport through the Bering Strait with warmer temperatures. This pattern can be interpreted as warm temperatures in the Bering Sea leading to

sea ice thinning allowing for easier transport through the strait. However, it is also possible that the EOFs are simply capturing the fact that sea ice is highly variable in that region. The third mode is also a transport signal but is roughly a ninety degree rotation of the second mode, again suggesting mathematical importance but not physical. Finally the fourth mode indicates broad sea ice gain associated with warmer temperatures (Figure 4.6 d), which is unlikely to be physical. Overall, these signals do not indicate a clear physical relationship in 2-m temperature driving changes in sea ice concentration. That is not to say that 2-m temperature does not affect sea ice, but that at the sub-seasonal timescales considered here, it has no prominent mode distinguishable from noise. The signal could be capturing part of a reverse relationship, of sea ice changes driving 2-m temperatures, but such a consideration is beyond the scope of our work. This signal could also be a mathematical artifact. It is the nature of EOFs that the analysis will always return a signal even if it has no physical basis.

4.2.0.2 Atlantic Region JJA

The leading mode associated with significant height of wind waves (Figure 4.9 a) shows a similar dipole pattern to the Pacific region (Figure 4.3 b). We again interpret this signal as sea ice transport resulting from surface cyclones interacting with a persistent high pressure system (Figure 4.4). The remaining modes are too noisy to discern a physical process (Figure 4.3 b-d).

The overall signal in Figure 4.10 a is quite similar to its Pacific counterpart (Figure 4.6 a) with a large region of sea ice loss associated with upward (negative) latent heat flux. This signal is reinforced by the third leading mode (Figure 4.10 c). Physically we also interpret these signals to be driven by a persistent high-pressure system as described above (Figure 4.5). However, there are two prominent regions in the Laptev and Barents Seas that exhibit the opposite sea ice behavior in the leading mode though it is not present in the third (Figure 4.10 a, c).

There are several ways to interpret sea ice behavior in those regions. Firstly, these could simply be regions where the sea ice field exhibits high internal variability and that variability is dominating the coupled analysis. Additionally, the anomalous signal is strongest in the Laptev Sea. The sea ice in this region is landfast ice with much of it being both land and bottom fast year round (Mahoney 2018). Consequently it may not be affected dynamically in the same way as its non-fast counterparts. These different dynamical responses could result in the different signals in Figure 4.10 a.

The second and fourth leading modes of variability for latent heat flux appear to capture transport signals. In the second mode, there are two dipole signals, one in the Barents and Kara Seas and the other in the Laptev Sea (Figure 4.10 b). The fourth mode shows a single dipole signal across the region of interest (Figure 4.10 d). If there is sea ice loss in the regions of direct variation (red) as before, then the sea ice gain in the adjacent region of indirect variation (blue) could be due to the eastward transport of the sea ice. Notably, the transport direction is reversed in the Laptev Sea, which we also attribute to the complicated nature of landfast ice. Taken together with the loss signal discussed for the first and third modes, what this means is that when there is upward (negative) latent heat flux, sea ice tends to thin and melt, and that thinned ice is more easily transported.

Finally we consider the leading modes of variability resulting from 2-m temperature anomalies. Figure 4.11 shows more coherent signals than its Pacific counterparts (Figure 4.7). The first and third modes both capture north-south aligned dipole signals (Figure 4.11 a and c) while the second and fourth modes largely capture east-west aligned dipole signals (Figure 4.11 b and d). However, these signals seem to negate each other. While the first mode indicates equatorward transport associated with a warmer Arctic, the third mode indicates poleward transport for the same temperature anomaly. Similarly, the second mode indicates westward transport and the fourth eastward for a warm Arctic. While it is certainly possible for sea ice to be transported in any direction, that alone does not present a discernible relationship between changes in sea ice concentration and 2-m temperature.

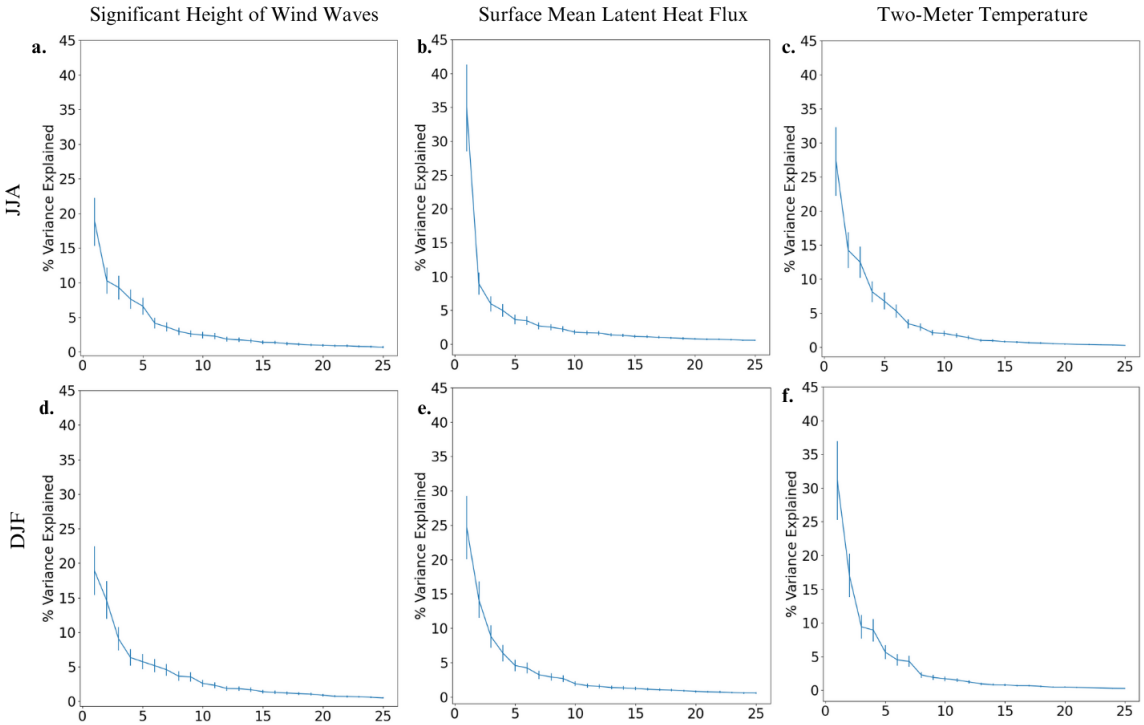


Figure 4.1: Percent variance explained of each EOF for the Atlantic region. The top row (a-c) is for summer (jja) and the bottom row (d-f) is for the winter (djf). Panels a and d are for significant height of wind waves, b and e for surface mean latent heat flux, and c and f are for 2-m temperature.

4.2.0.3 Pacific Region DJF

The first and second modes of variability for the significant height of wind waves show transport of sea ice through the Bering Strait but in opposite directions (Figure 4.12 a and b). The first mode indicates sea ice being drawn from the Bering Sea, through the Bering Strait, and into the Chukchi Sea (Figure 4.12 a). This mode could result from the same poleward winds driven by a surface cyclone interacting with the Beaufort High, as discussed with the summer wave signal (Figure 4.3 a). This pattern could arise by the surface cyclone traveling east such that its warm sector is in the Chukchi Sea. Then the cyclone winds would act to pull sea ice equatorward through the strait (Figure 4.8). The

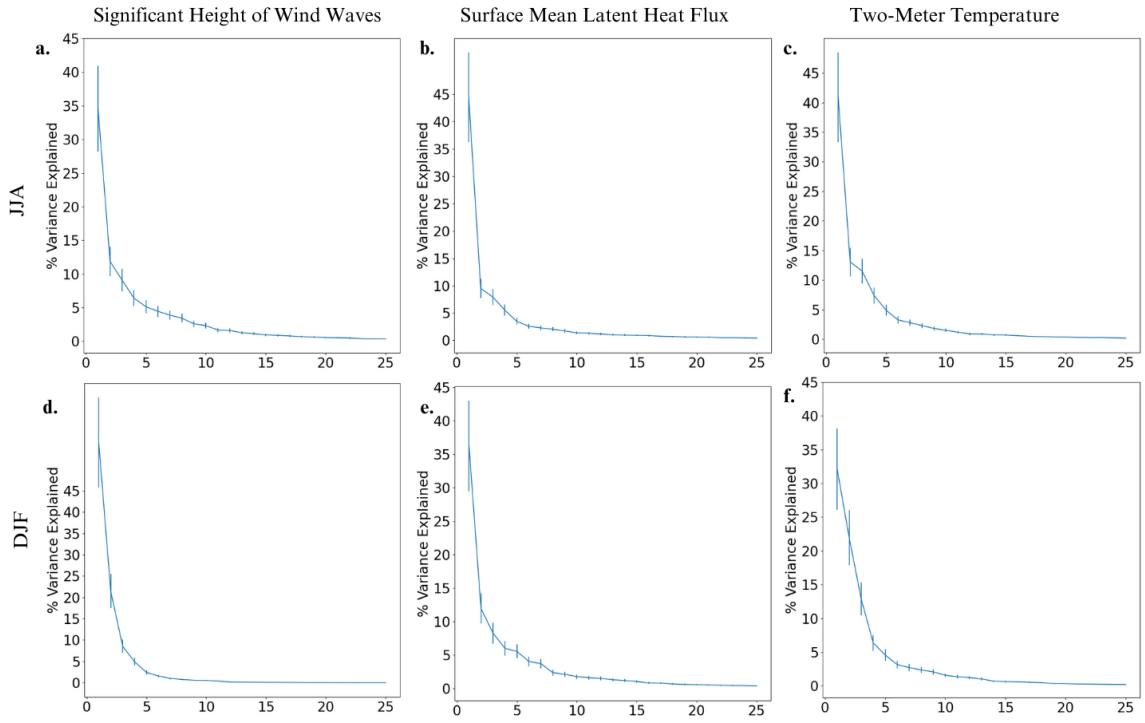


Figure 4.2: Percent variance explained of each EOF for the Pacific region. The top row (a-c) is for summer (jja) and the bottom row (d-f) is for the winter (djf). Panels a and d are for significant height of wind waves, b and e for surface mean latent heat flux, and c and f are for 2-m temperature.

third and fourth modes both show tripole signals through the Bering Strait that are unlikely to be physical (Figure 4.3 c and d). Mathematically, these are likely higher harmonics of the dipole modes previously discussed. Even though the fourth mode captures a large region of variability in the Sea of Okhotsk (Figure 4.12 d), we are wary of deriving much meaning from the signal because it is tied to the non-physical tripole.

The first two modes for mean surface latent heat flux are largely similar and likely represent the same physical relationship (Figure 4.13 a and b). Anytime there is open ocean, there will be large, upward (negative) surface latent heat fluxes. Unlike in the summer months, the lack of shortwave radiation in winter does not allow for the clear skies explanation presented above. However, the temperature difference between open ocean and sea

ice is greatest in the winter, resulting in a baroclinic zone. We propose that the physical processes being captured in the first two leading modes for latent heat is the open ocean portion of that baroclinic zone, whose exact location will change throughout the winter, and represents increased storminess on smaller spatial and temporal scales than are being captured here. It is then those storms that lead to the sea ice loss associated with the negative (upward) latent heat flux (Figure 4.5). It is worth noting that this setup is consistent with the the physical mechanism proposed for the second mode in significant height of wind-driven waves (Figure 4.12 b) and the first two modes for 2-m temperature (Figure 4.14 a and b).

The third and fourth modes for latent heat flux show transport through the Bering Strait, equatorward for the third, and poleward for the fourth (Figure 4.13 c and d). Note that these two modes could be reversed due to the sign invariance of empirical orthogonal functions. We interpret both modes through the lens of mean surface latent heat flux being positive (downward) over the whole region. This setup corresponds to partial sea ice coverage, similar to the MIZ (Figure 4.15). Since the EOF analysis is performed on anomalies, this can be thought of as either a positive or weakly negative flux. Additionally, sea ice floes are transported more easily than solid ice pack. Then the transport mechanisms in Figure 4.4 can act on the sea ice. Note that in this scenario, the latent heat flux signal is not a direct mechanism for sea ice loss but acts as an environmental precursor.

For 2-m temperature, the first, second, and fourth leading modes indicate sea ice gain with warmer temperatures (Figure 4.14 a, b, and d). This counter intuitive result could be consistent with the overall picture discussed in this section. Consider the warm sector of a surface cyclone that moves eastward across the Bering Sea. When that warm sector is aligned with the Bering Strait, not only would there be anomalously warm surface temperatures but northerly winds as well. These winds could act to pull sea ice south through the strait, resulting in sea ice gain (Figure 4.8). The third mode is more aligned to what we would expect to see, warmer temperatures associated with sea ice loss (Figure 4.14

c). There is a region along the Alaskan coast that indicates sea ice gain but that may be a mathematical artifact or the analysis struggling to capture the dynamics of landfast ice.

Taken together, all three of these factors generally point to the same setup: the strong baroclinic zone between the sea ice pack and open ocean leads to increased storminess in the Bering Sea which causes bidirectional sea ice transport through the Bering Strait depending on the storm's location and local wind direction. Furthermore, the generally high variability of sea ice concentration in the Bering Strait is highlighted. There has yet to be a year where the March maximum sea ice extent does not extend through the Bering Strait, but there is variability in how deep into the Bering Sea the ice extends. Consequently, that region being highlighted by the EOF analysis is expected. This variability is seen in the composite difference in sea ice concentration for high sea ice years versus low (Figure 4.16). The composite difference shows higher sea ice all along the sea ice edge; if we focus on the Bering Strait, we see that high sea ice years have more sea ice throughout the Bering Strait and Sea (Figure 4.16 a) and that the region has a high degree of variability (Figure 4.16 b).

4.2.0.4 Atlantic Region DJF

We only consider the first mode of variability for significant height of wind waves. The second, third, and fourth modes show both tri- and quadrupole moments that are unlikely to be physical (Figure 4.17). The first mode shows widespread sea ice gain for larger than average ocean waves (Figure 4.17 a). We interpret this as half of a transport signal where the region of sea ice loss occurs far enough south and spreads across a wide enough region that it is not captured by the EOFs. Additionally, we are interpreting these results with the context that the leading mode of variability for this term in the other seasons and regions analyzed are transport signals, thus making it likely for this one to be as well.

For our discussion of latent heat, we focus our analysis on its first and third modes. The second and fourth modes of variability in latent heat are quadrupole patterns that are

likely to be mathematical artifacts and non-physical (Figure 4.18 b). The first and third modes show approximately opposite signals, one indicating sea ice gain (loss) and one sea ice loss (gain) with positive (negative) surface latent heat flux (Figure 4.18 a and c). In the third mode, the strongest part of the signal is further south than in the first, roughly co-located with the North Atlantic storm track (Figure 4.18 c). We interpret these signals with a positive (downward) surface latent heat flux.

As discussed in the previous section, a positive flux is associated with a sea ice state of mixed ice floes and open ocean. Then, the ice gain in the region in the first mode corresponds to the southern advancement of the MIZ. As sea ice freezes throughout the winter, the sea ice edge extends further and further south. If we considered a location that was ice-free in the summer but ice covered in March, then it would start the freeze season as open ocean, transition to a state of ice floes with regions of open ocean, and finally, solid ice pack. This transition would be associated with a change from a strongly negative (upward) surface latent heat flux to either a weakly negative or positive (downward) signal. That is, positive latent heat flux where sea ice is accumulating, as seen in the first mode (Figure 4.18 a).

In the third mode, however there is sea ice loss associated with positive latent heat flux. We believe this pattern is related to sea ice loss from surface cyclones in the North Atlantic storm track, a key region for winter VRILEs (Figure 3.7). While the first mode is capturing the solidification of the MIZ, the third is capturing the MIZ's interactions with the broader environment. Additionally, after winter VRILEs occur, there can be a net ice gain in the following days and weeks due to the opened region refreezing, causing the third mode to ultimately feed the first.

Finally, we address 2-m temperature. Note that the leading mode in 2-m temperature (Figure 4.19 a) is nearly identical in shape to the third mode in mean surface latent heat flux (Figure 4.18 c). With this in mind, we interpret the leading mode for 2-m temperature

in context of sea ice loss and colder temperature in order to align the results with our discussion from the latent heat.

One final note on the higher order signals. These regions of loss and gain are aligned along the path of the prevailing winds (Figure 4.19 b-d). It is possible that these modes are capturing large scale ice transport through the Barents Sea. In the winter, this is a highly dynamic region for sea ice with the overall trend to be gain but as new sea ice freezes that thin ice is susceptible to numerous forcings. We believe these patterns are the product of the singular value decomposition driver of the analysis categorizing that susceptibility into distinct modes.

4.3 Combined Analysis

While the above analysis provides us with insight as to how different mechanisms lead to sea ice change, it does not indicate the relative importance of each variable. In order to ascertain that, we repeat the multivariate EOF on a matrix containing a combination of sea ice concentration, latent heat, 2-m temperature, and significant height of wind waves. If the leading mode from this combined analysis strongly resembles the leading mode from the individual analyses then it is an indication of the relative importance of that term.

The clearest results are in the summer in the Pacific region (Figure 4.20). Here we see that the first mode (Figure 4.20 a) is nearly identical to the leading mode of mean surface latent heat flux (Figure 4.6 a) and the combined second mode (Figure 4.20 b) is nearly identical to the leading mode of significant height of wind waves (Figure 4.3 a). This is also true for the summer months in the Atlantic region (Figure 4.21, 4.10 a, and 4.9 a), though the wind wave signal most closely resembles the combined second and third modes (Figure 4.21 b and c). The leading mode accounts for about 29% of the covariance in the Pacific (Figure 4.24 a) and 24% in the Atlantic (Figure 4.24 b) while the second modes account for 12% (Figure 4.24 a) and 8% (Figure 4.24 b) respectively. Therefore, we conclude that surface latent heat flux is roughly twice as important as wind driven waves

for sea ice concentration changes at subseasonal timescales in the summer. Additionally, we conclude that 2-m temperature is not a significant factor at these timescales during the summer.

2-m temperature plays a more important role in winter sea ice concentration changes. In fact, the leading mode of both winter combined modes strongly resembles the leading mode of 2-m temperature (Figures 4.22 a, 4.23 a, 4.14 a, and 4.19 a). Unfortunately, that signal is so dominate in the combined results that we are unable to further differentiate the relative importance of latent heating and wind waves. These results are reinforced by considering the North et al criteria. For the Pacific region, the leading mode is clearly distinct and accounts for approximately 35% of the total variance but all other modes are indistinguishable from each other (Figure 4.24 c). In the Atlantic region, none of the modes are distinguishable per the North et al criteria (Figure 4.24 d). Unfortunately, this means that we cannot determine the relative importance of the latent heat and ocean waves terms for winter subseasonal sea ice loss.

Since we are unable to parse out the relative importance of wintertime surface latent heat flux and significant height of wind waves because of the overwhelming 2-m temperature signal, we once again perform multivariate EOF analysis this time leaving out 2-m temperature. As in the summer, in the Pacific region, the leading mode is very similar to the leading mode in surface latent heat flux (Figure 4.25 a and 4.12 a) and the second mode is similar to the leading mode in significant height of wind waves (Figure 4.25 b and 4.12 a). In the Atlantic region, both leading modes are nearly identical to the first two modes for mean surface latent heat flux (Figure 4.25 c and d, 4.18 a and b). Taking these results into consideration, we conclude that in all seasons, surface latent heat flux plays a more important role in subseasonal sea ice changes than wind waves and that in the wintertime, 2-m temperature is the most important factor but does not play an important role in the summertime.

4.4 Conclusions

Broadly speaking, we find that modes in the Atlantic region are more variable than those in the Pacific. We attribute this difference primarily to geography. In the Pacific region, the Bering Strait is the only avenue by which sea ice can be transported to lower latitudes. But on the Atlantic side, Arctic waters interact with the Atlantic Ocean through a large swathe of open ocean, making sea ice transport easier. This greater degree of variability in the Atlantic region manifests in our analysis as less coherent signals and modes of variability being less distinct in a North et al. (1982) criteria sense (Figures 4.1 and 4.2). These regional differences are especially prominent in the winter months.

Additionally, we find noticeable differences between winter and summer results. In general, there are more significant, independent modes in the winter for all variables than there are in summer (Figures 4.1 and 4.2). This may be because of the dominance of the seasonal freezing signal; winter VRILEs can result in net ice gain once the open region has refrozen (Kriegsmann and Brümmer 2014). Or, especially for the Pacific region, resulting from the variability being constrained to a relatively small geographic region. We also find that 2-m temperature plays a significant role in winter sub-seasonal sea ice concentration change but not in the summer. Due to the lack of incoming shortwave radiation in the winter, this dependence could be pointing to an increased importance of surface cyclones. Finally, we find that in all seasons LH plays a more important role in subseasonal sea ice loss than ocean waves.

JJA Pacific Significant Height of Wind Waves

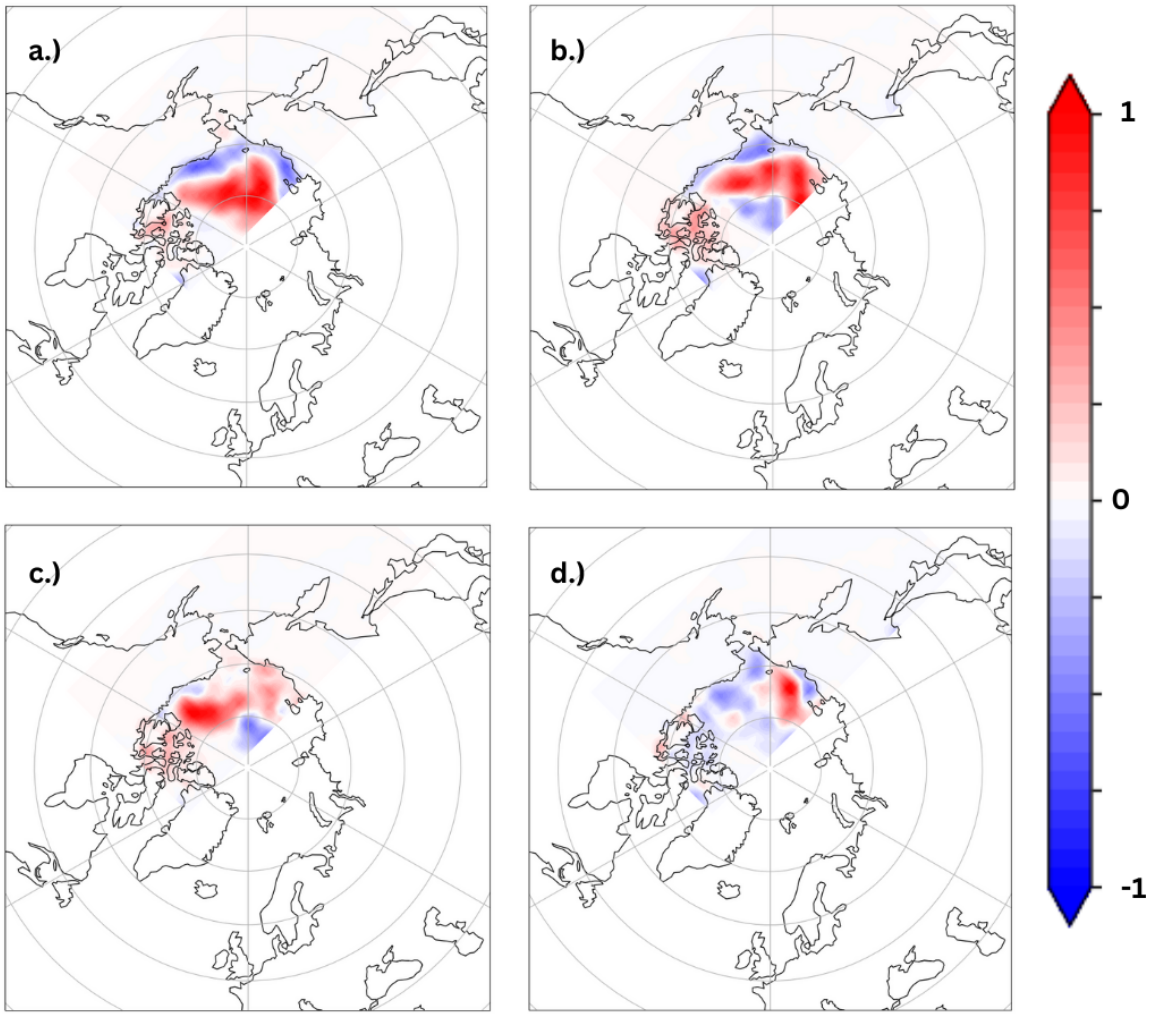


Figure 4.3: Normalized principal component timeseries 1-4 (a-d) projected onto daily change in sea ice concentration anomalies. The PCs are taken from the multivariate EOF of summer daily change in sea ice concentration and daily mean significant height of wind wave anomalies in the Pacific region. Reds indicate that the sea ice directly varies with sea ice and blues indicate indirect variation.

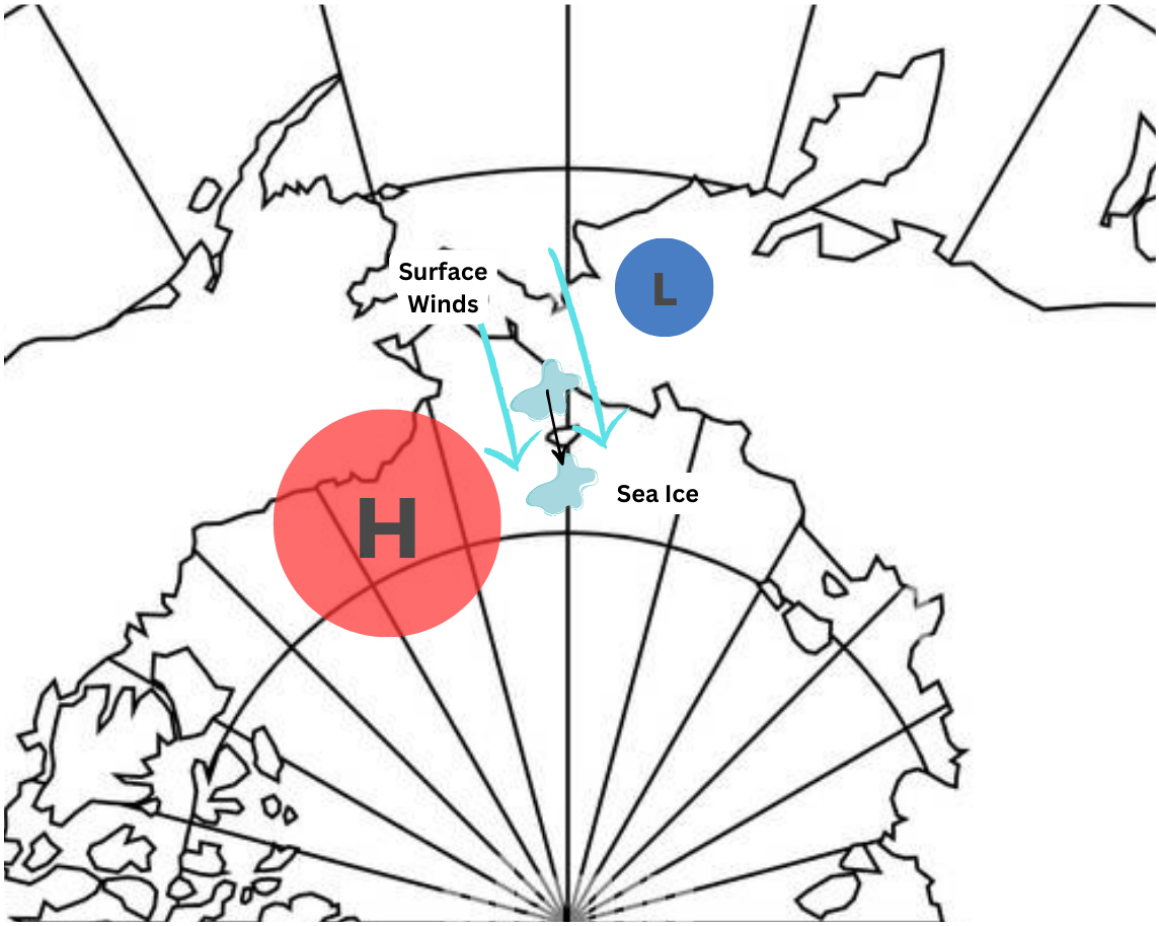


Figure 4.4: Diagram depicting an Arctic cyclone interacting with the Beaufort High and the resulting winds. The area of the winds would have higher than average ocean waves with sea ice gain at the arrow tip and loss behind it.

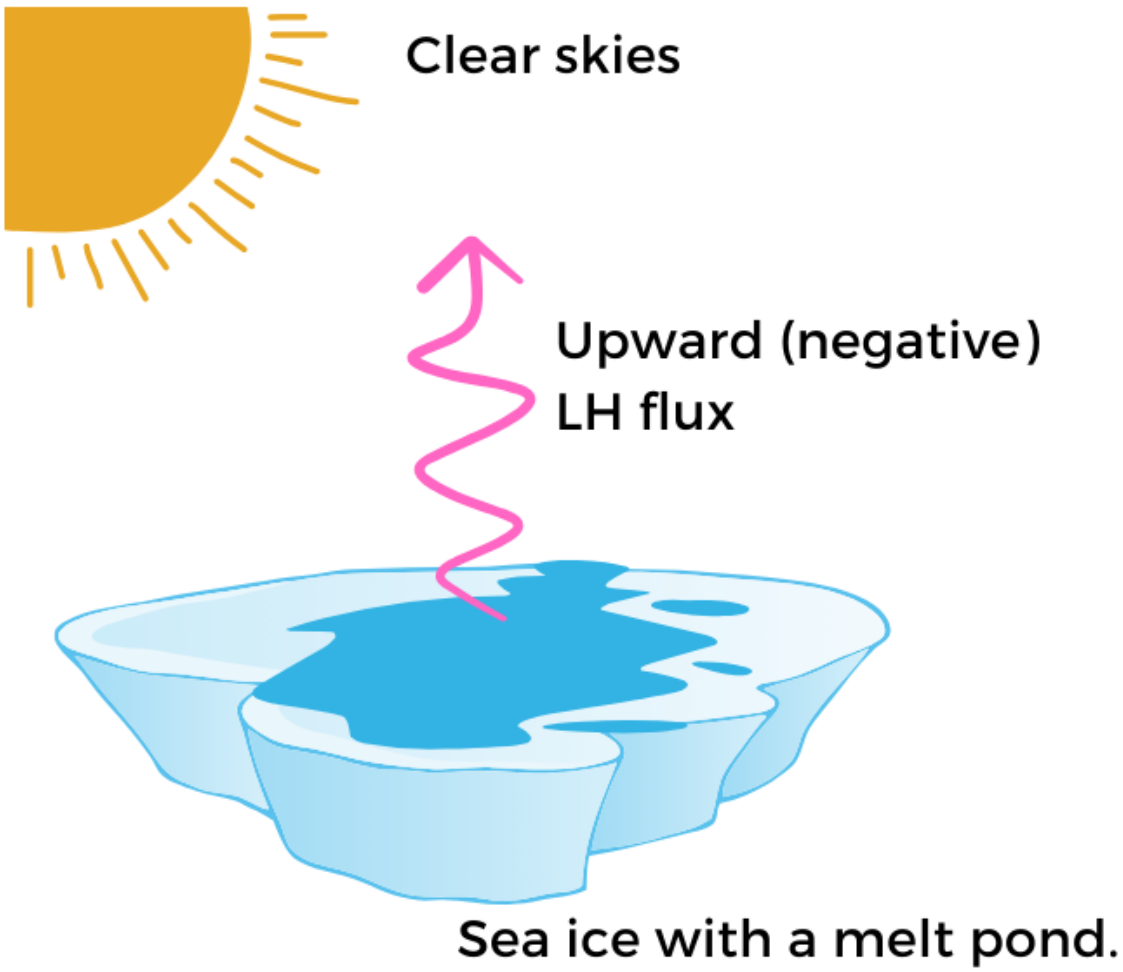


Figure 4.5: Schematic depicting the proposed mechanism for sea ice loss associated with negative latent heat fluxes in summer. Strong solar radiation from clear sky conditions leading to upward LH flux from melt ponds on sea ice.

JJA Pacific Surface Mean Latent Heat Flux

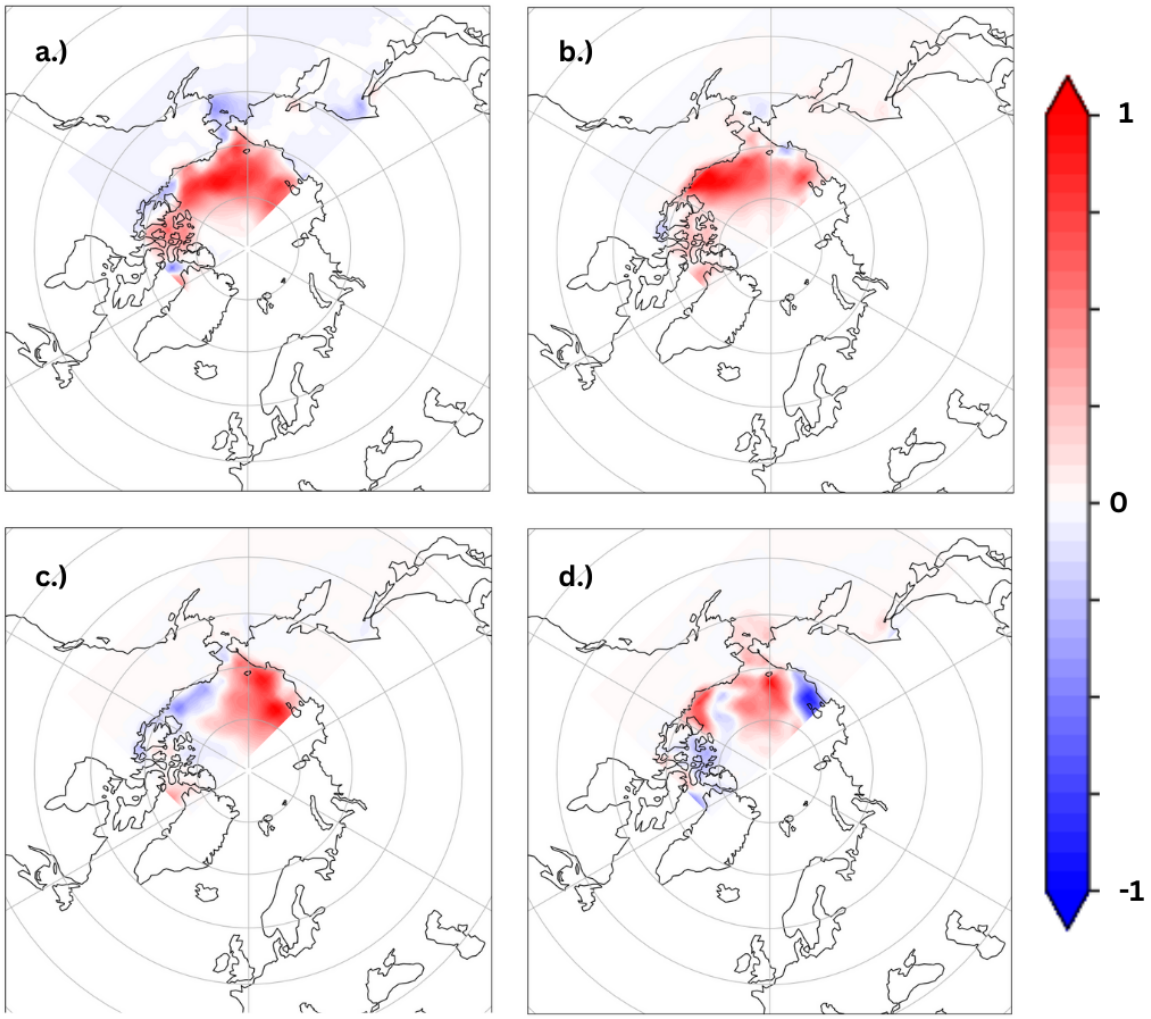


Figure 4.6: Normalized principal component timeseries 1-4 (a-d) projected onto daily change in sea ice concentration anomalies. The PCs are taken from the multivariate EOF of summer daily change in sea ice concentration and daily mean surface latent heat flux anomalies in the Pacific region. Reds indicate that the sea ice directly varies with sea ice and blues indicate indirect variation.

JJA Pacific 2-m Temperature

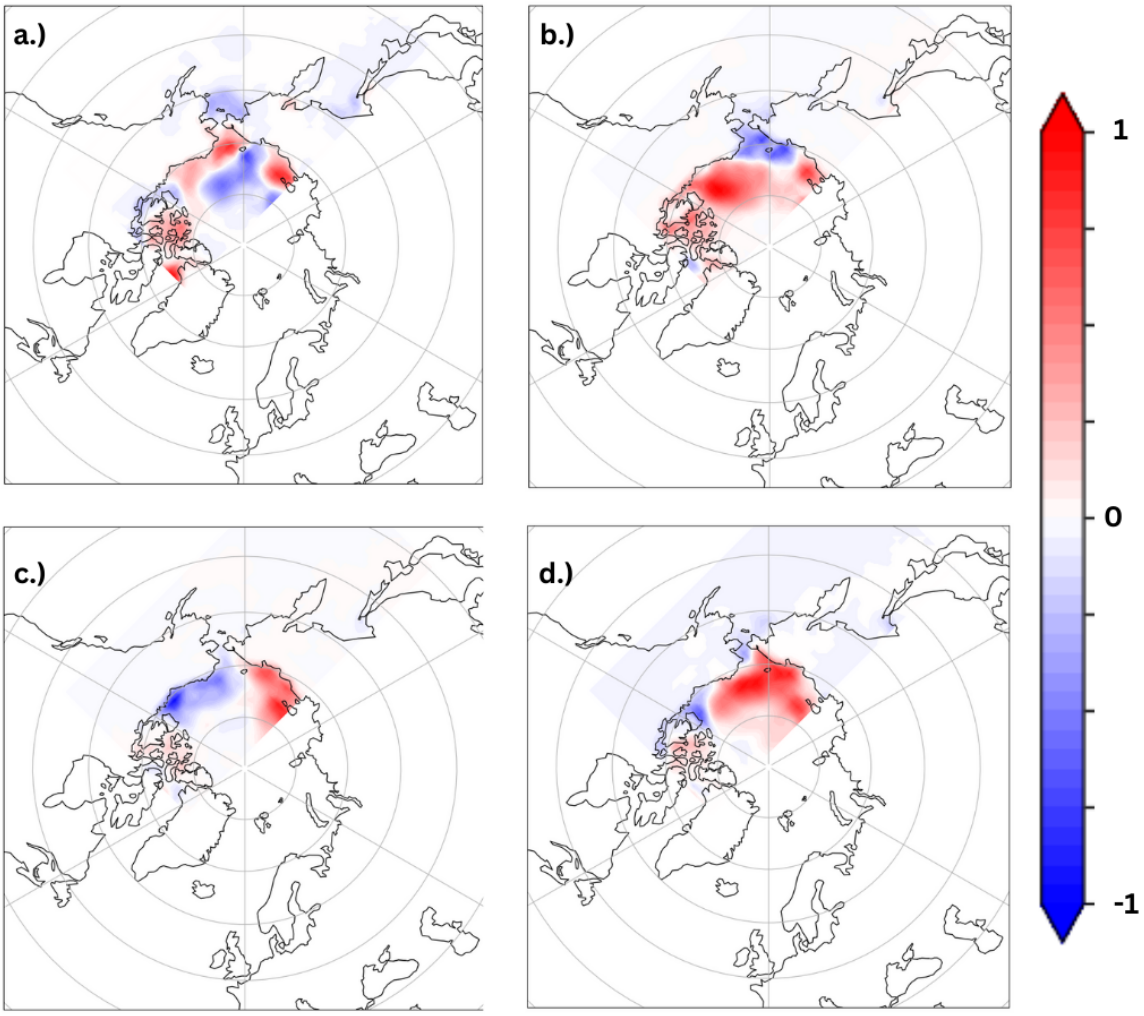


Figure 4.7: Normalized principal component timeseries 1-4 (a-d) projected onto daily change in sea ice concentration anomalies. The PCs are taken from the multivariate EOF of summer daily change in sea ice concentration and daily mean 2-m temperature anomalies in the Pacific region. Reds indicate that the sea ice directly varies with sea ice and blues indicate indirect variation.



Figure 4.8: Diagram depicting a proposed mechanism for how warm temperatures could be associated with sea ice gain via transport. The warm temperatures in the Bering Sea could be the warm sector of a surface cyclone. The winds associated with this cyclone then draws sea ice into the Bering Sea.

JJA Atlantic Significant Height of Wind Waves

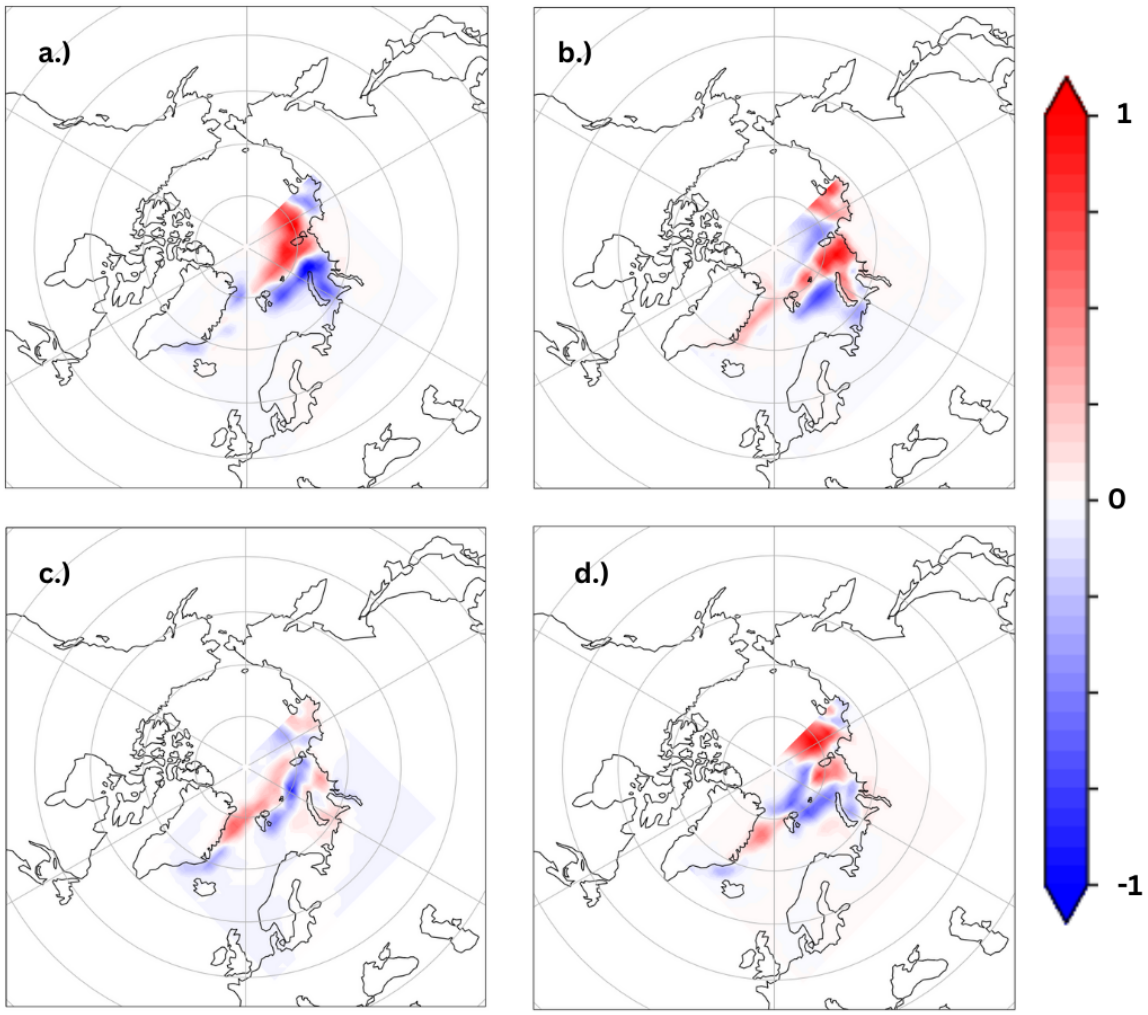


Figure 4.9: Normalized principal component timeseries 1-4 (a-d) projected onto daily change in sea ice concentration anomalies. The PCs are taken from the multivariate EOF of summer daily change in sea ice concentration and daily mean significant height of wind wave anomalies in the Atlantic region. Reds indicate that the sea ice directly varies with sea ice and blues indicate indirect variation.

JJA Atlantic Mean Surface Latent Heat Flux

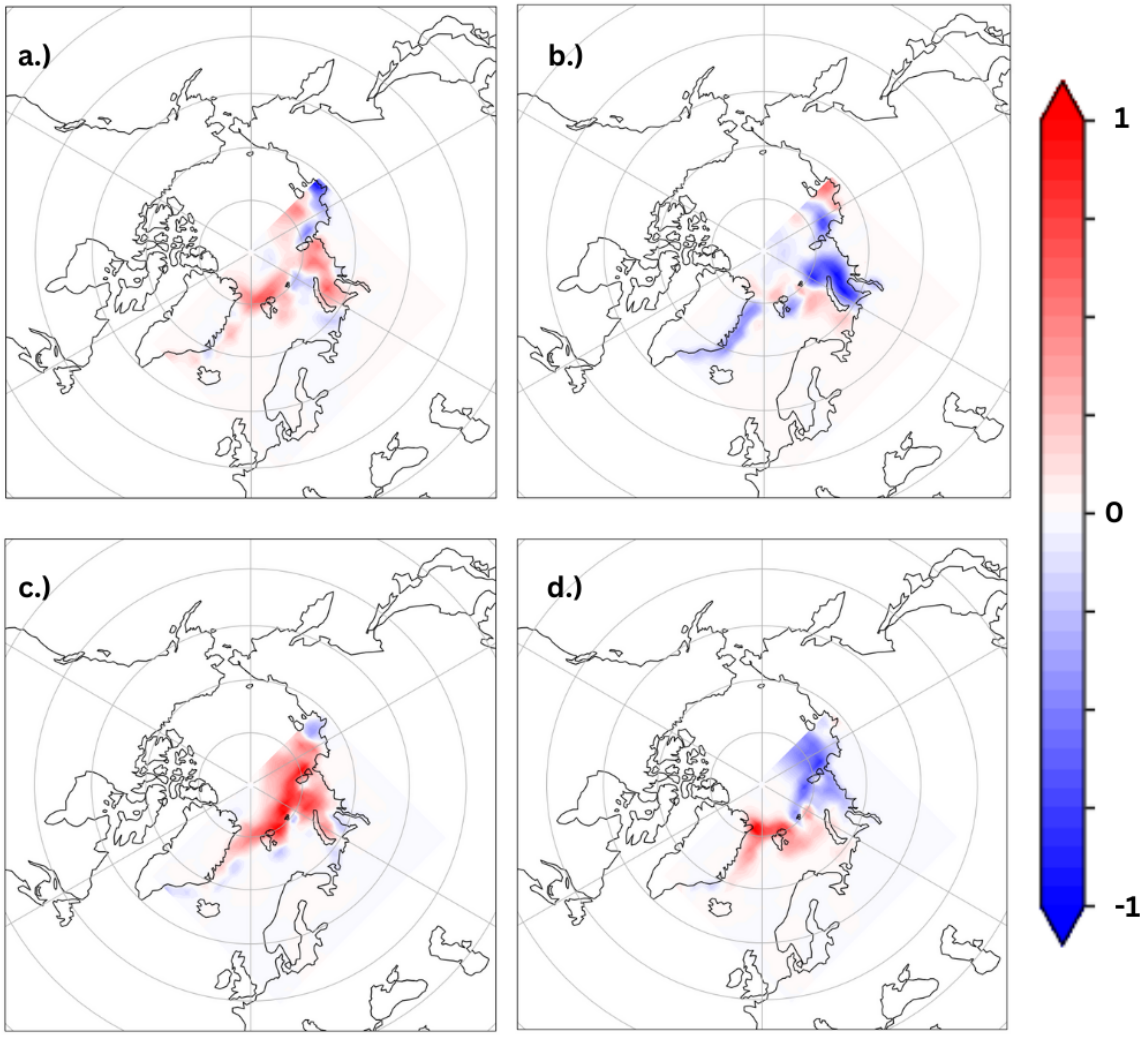


Figure 4.10: Normalized principal component timeseries 1-4 (a-d) projected onto daily change in sea ice concentration anomalies. The PCs are taken from the multivariate EOF of summer daily change in sea ice concentration and daily mean surface latent heat flux anomalies in the Atlantic region. Reds indicate that the sea ice directly varies with sea ice and blues indicate indirect variation.

JJA Atlantic 2-m Temperature

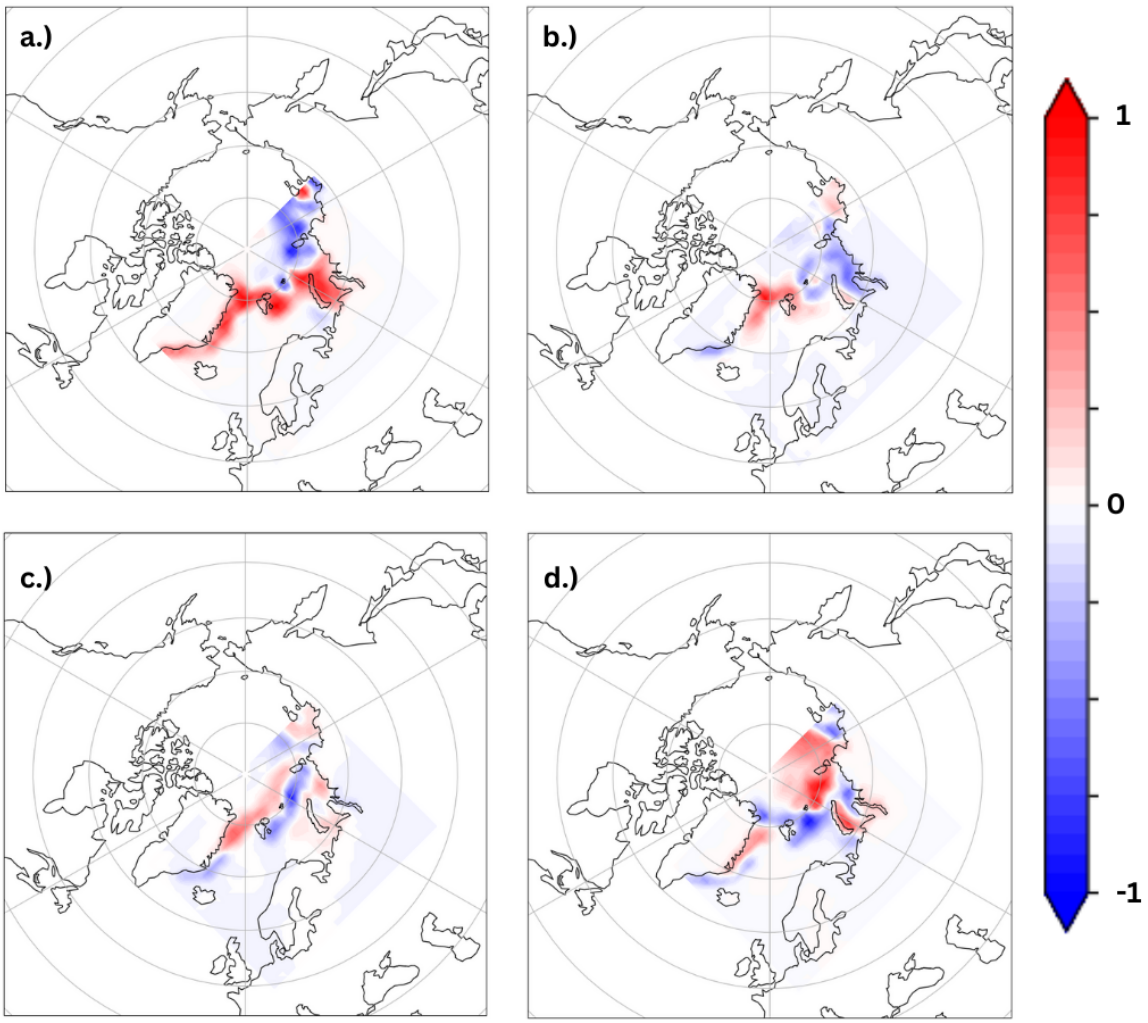


Figure 4.11: Normalized principal component timeseries 1-4 (a-d) projected onto daily change in sea ice concentration anomalies. The PCs are taken from the multivariate EOF of summer daily change in sea ice concentration and daily mean 2-m temperature anomalies in the Atlantic region. Reds indicate that the sea ice directly varies with sea ice and blues indicate indirect variation.

DJF Pacific Significant Height of Wind Waves

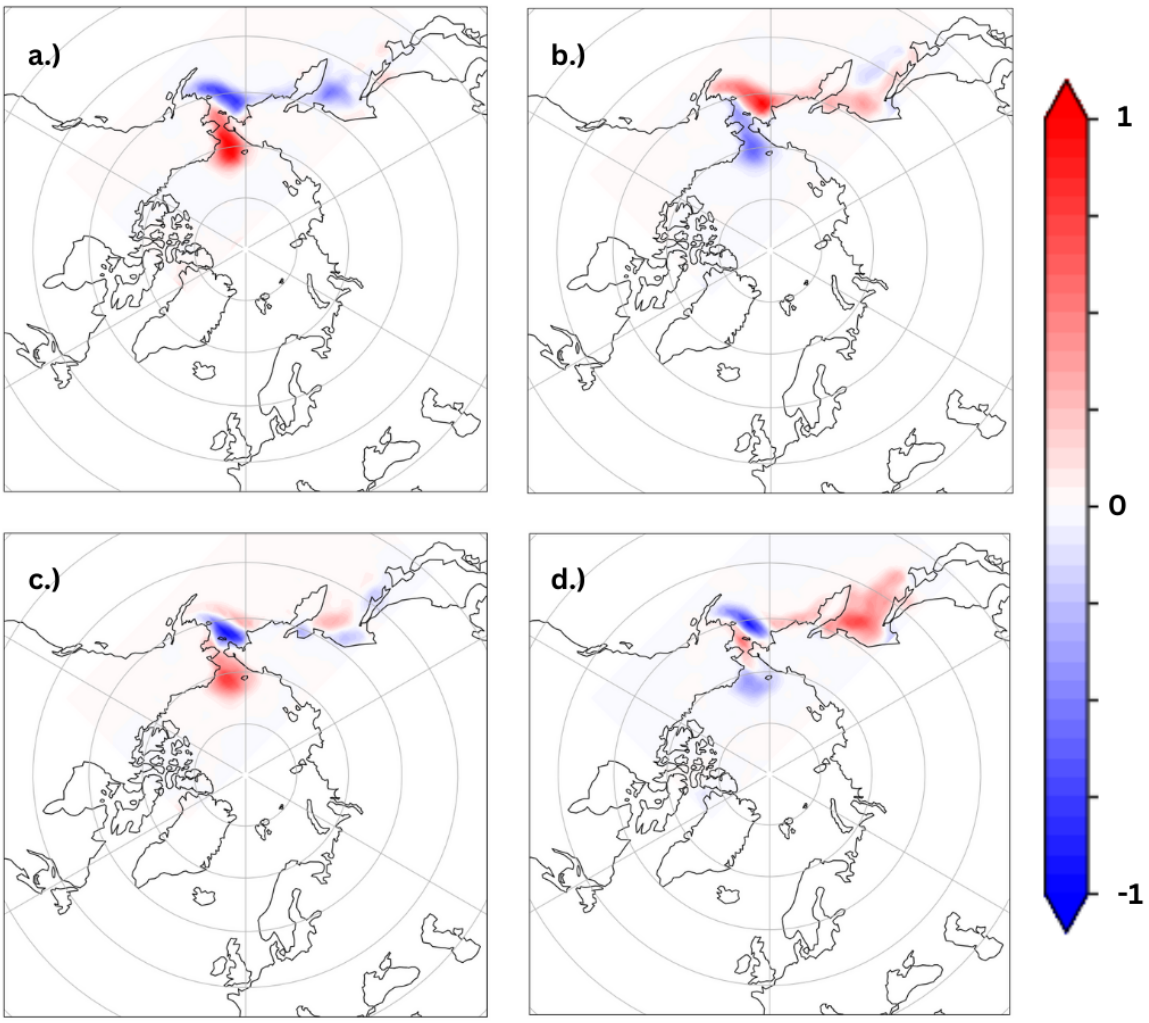


Figure 4.12: Normalized principal component timeseries 1-4 (a-d) projected onto daily change in sea ice concentration anomalies. The PCs are taken from the multivariate EOF of winter daily change in sea ice concentration and daily mean significant height of wind wave anomalies in the pacific region. Reds indicate that the sea ice directly varies with sea ice and blues indicate indirect variation.

DJF Pacific Mean Surface Latent Heat Flux

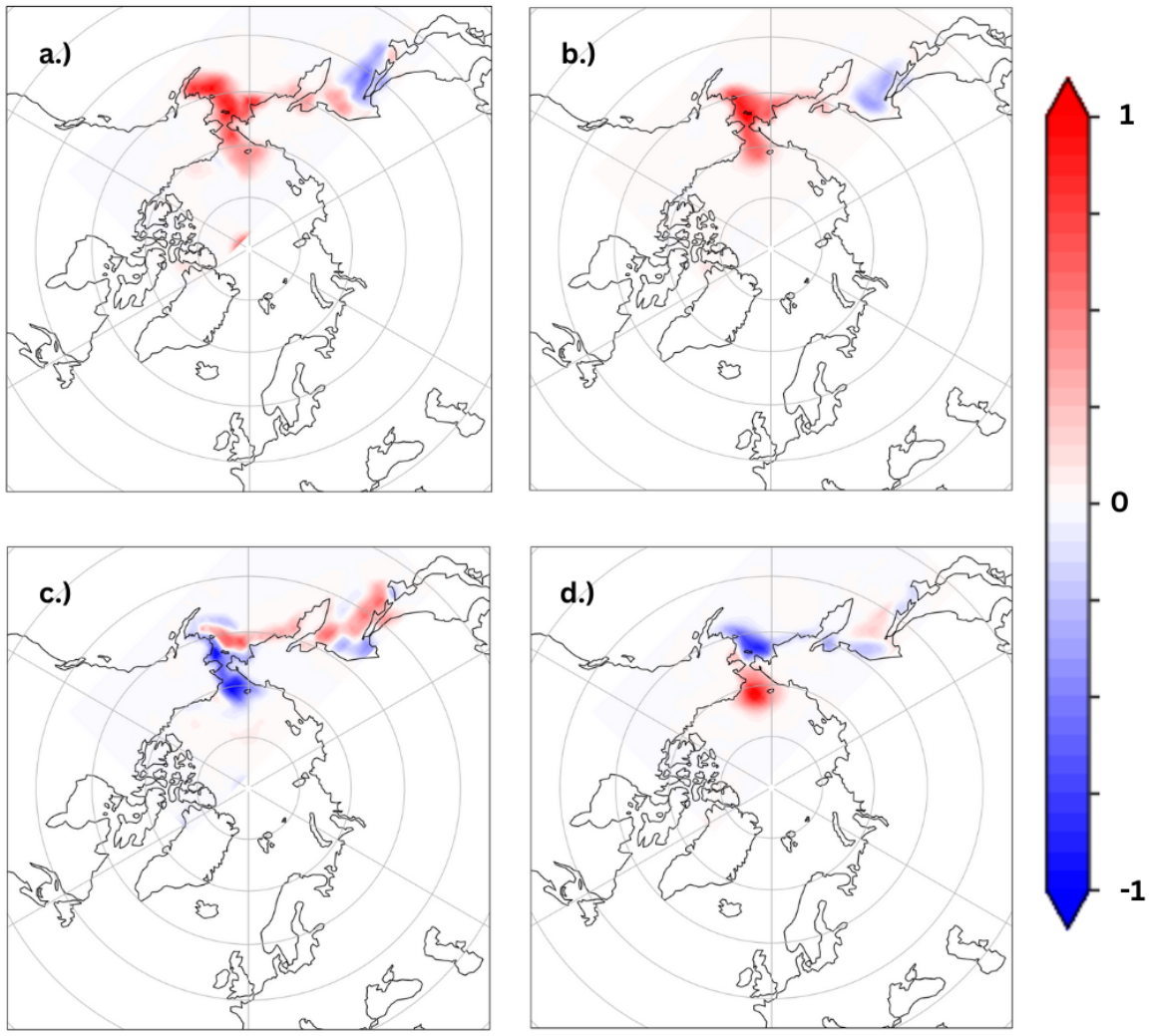


Figure 4.13: Normalized principal component timeseries 1-4 (a-d) projected onto daily change in sea ice concentration anomalies. The PCs are taken from the multivariate EOF of winter daily change in sea ice concentration and daily mean of mean surface latent heat flux anomalies in the pacific region. Reds indicate that the sea ice directly varies with sea ice and blues indicate indirect variation.

DJF Pacific 2-m Temperature

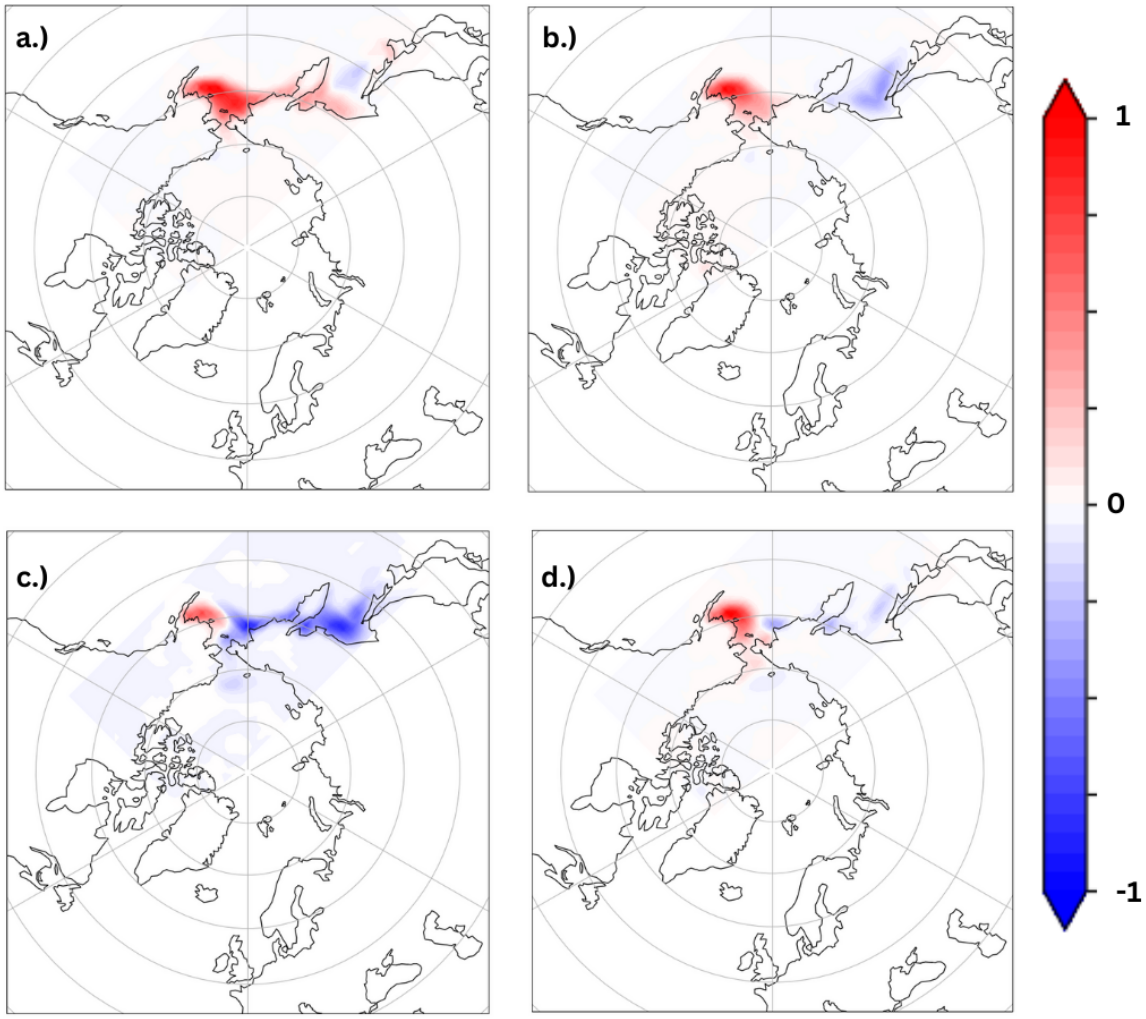


Figure 4.14: Normalized principal component timeseries 1-4 (a-d) projected onto daily change in sea ice concentration anomalies. The PCs are taken from the multivariate EOF of winter daily change in sea ice concentration and daily mean 2-m temperature anomalies in the pacific region. Reds indicate that the sea ice directly varies with sea ice and blues indicate indirect variation.

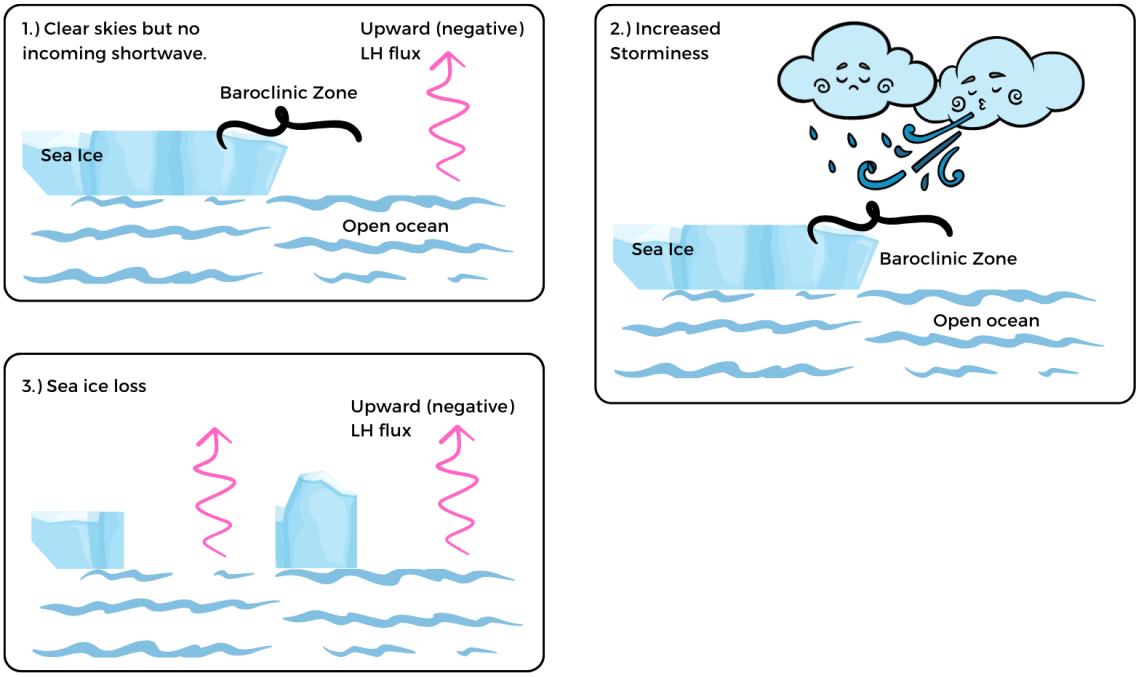


Figure 4.15: Schematic depicting the proposed mechanism for sea ice loss associated with negative latent heat fluxes in winter. In the winter, clear skies are not associated with increased solar radiation but there are still upward LH fluxes over regions of open ocean. The difference in temperature between the open ocean and sea ice is a baroclinic zone that can lead to increased storminess. Those storms can then further break up the sea ice through both winds and LH.

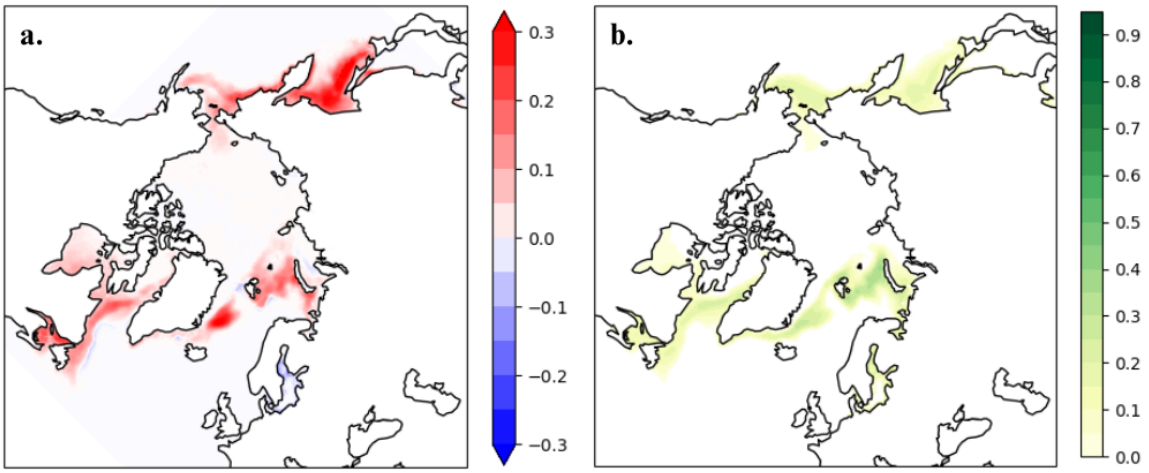


Figure 4.16: Composite difference of winter (djf) sea ice concentration for high versus low sea ice years (a). Standard deviation of winter (djf) sea ice concentration (b).

DJF Atlantic Significant Height of Wind Waves

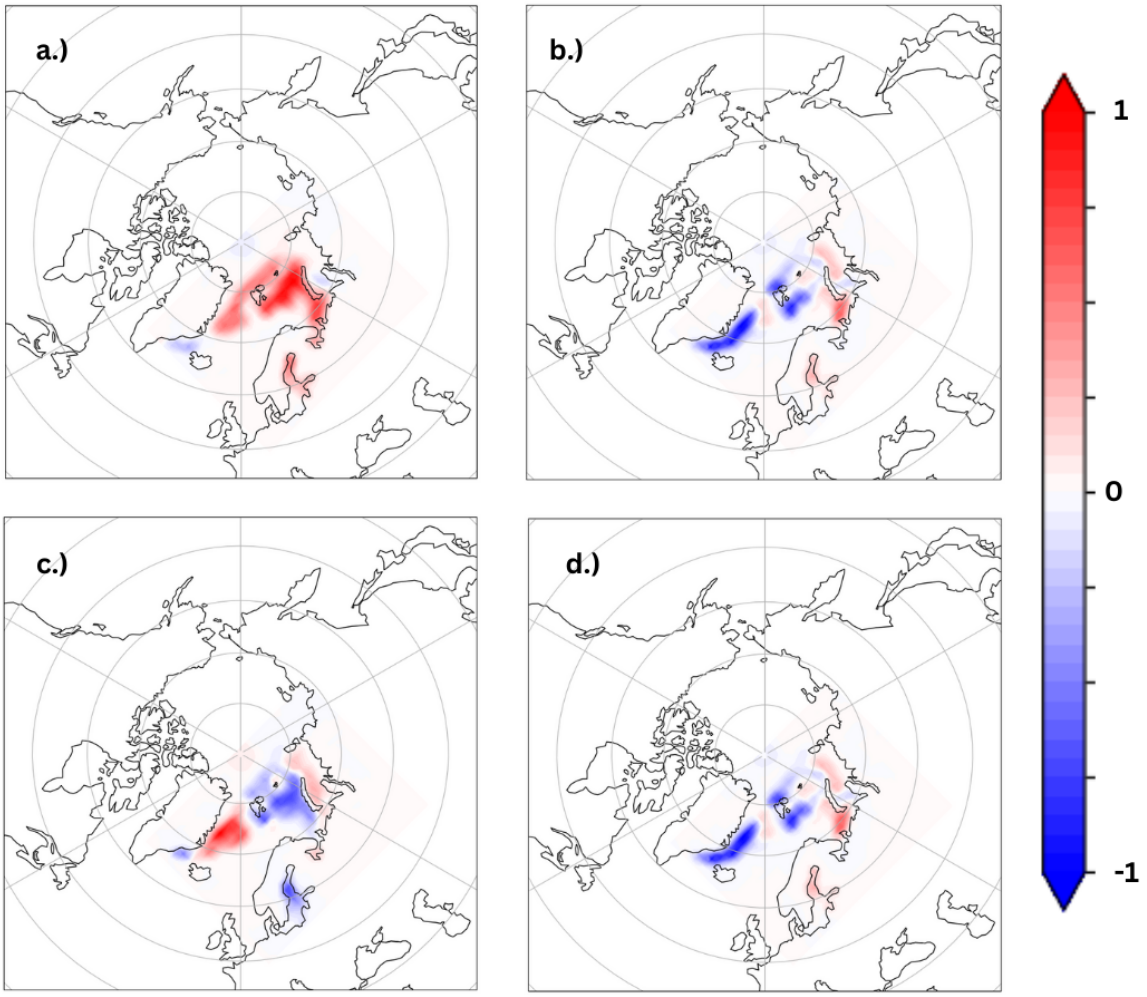


Figure 4.17: Normalized principal component timeseries 1-4 (a-d) projected onto daily change in sea ice concentration anomalies. The PCs are taken from the multivariate EOF of winter daily change in sea ice concentration and daily mean significant height of wind wave anomalies in the Atlantic region. Reds indicate that the sea ice directly varies with sea ice and blues indicate indirect variation.

DJF Atlantic Mean Surface Latent Heat Flux

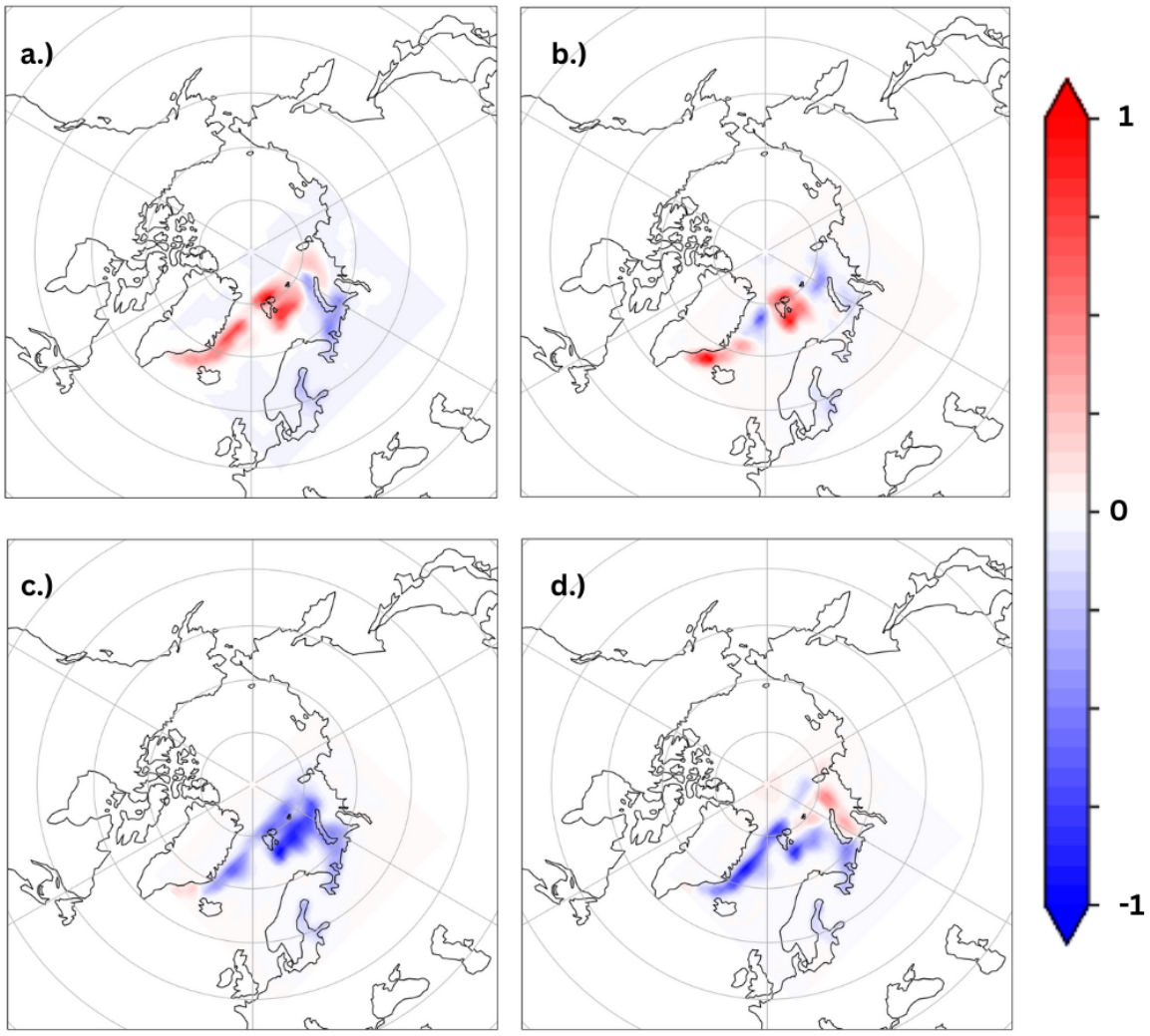


Figure 4.18: Normalized principal component timeseries 1-4 (a-d) projected onto daily change in sea ice concentration anomalies. The PCs are taken from the multivariate EOF of winter daily change in sea ice concentration and daily mean of mean surface latent heat flux anomalies in the Atlantic region. Reds indicate that the sea ice directly varies with sea ice and blues indicate indirect variation.

DJF Atlantic 2-m Temperature

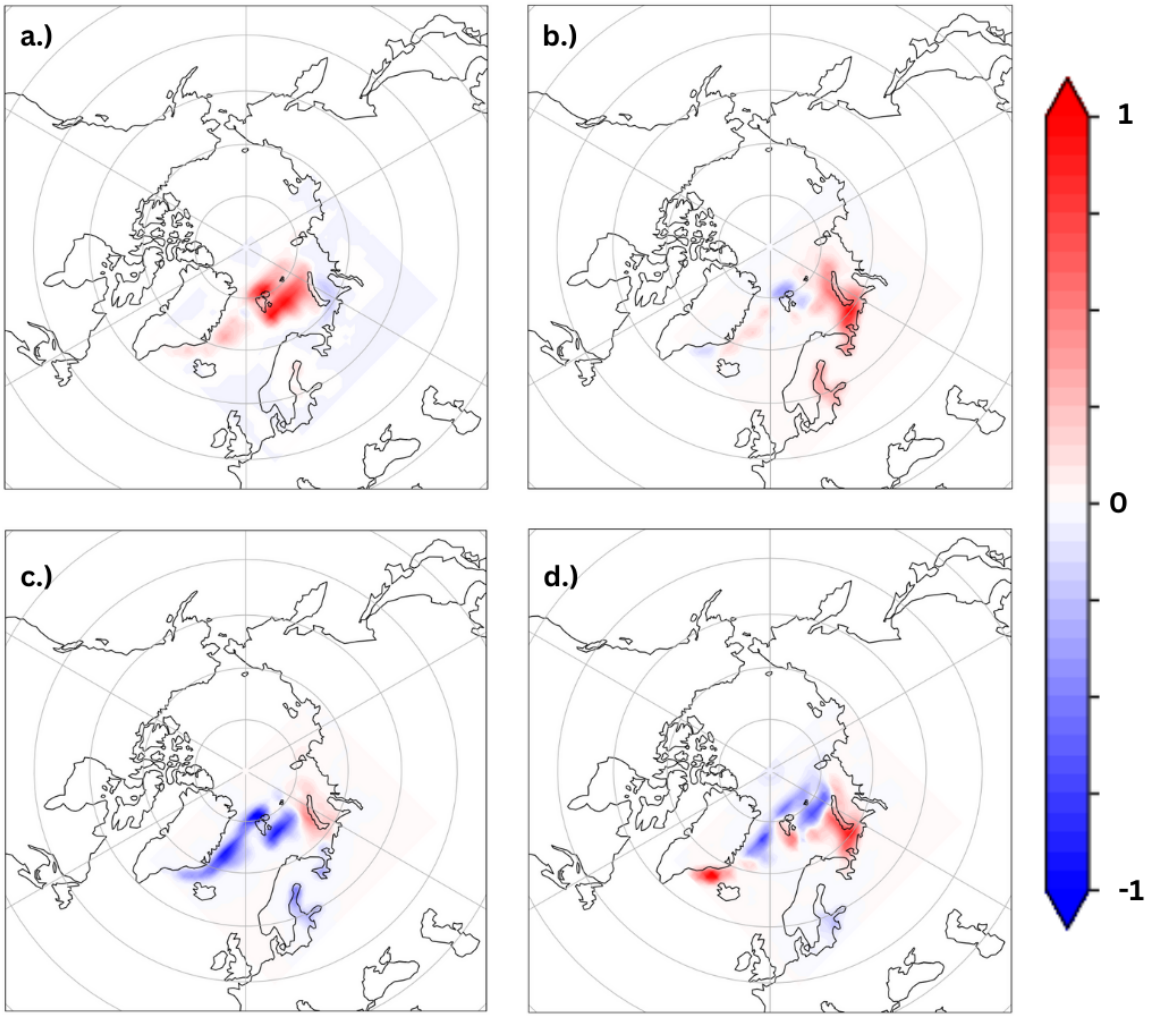


Figure 4.19: Normalized principal component timeseries 1-4 (a-d) projected onto daily change in sea ice concentration anomalies. The PCs are taken from the multivariate EOF of winter daily change in sea ice concentration and daily mean 2-m temperature anomalies in the Atlantic region. Reds indicate that the sea ice directly varies with sea ice and blues indicate indirect variation.

JJA Pacific Combined

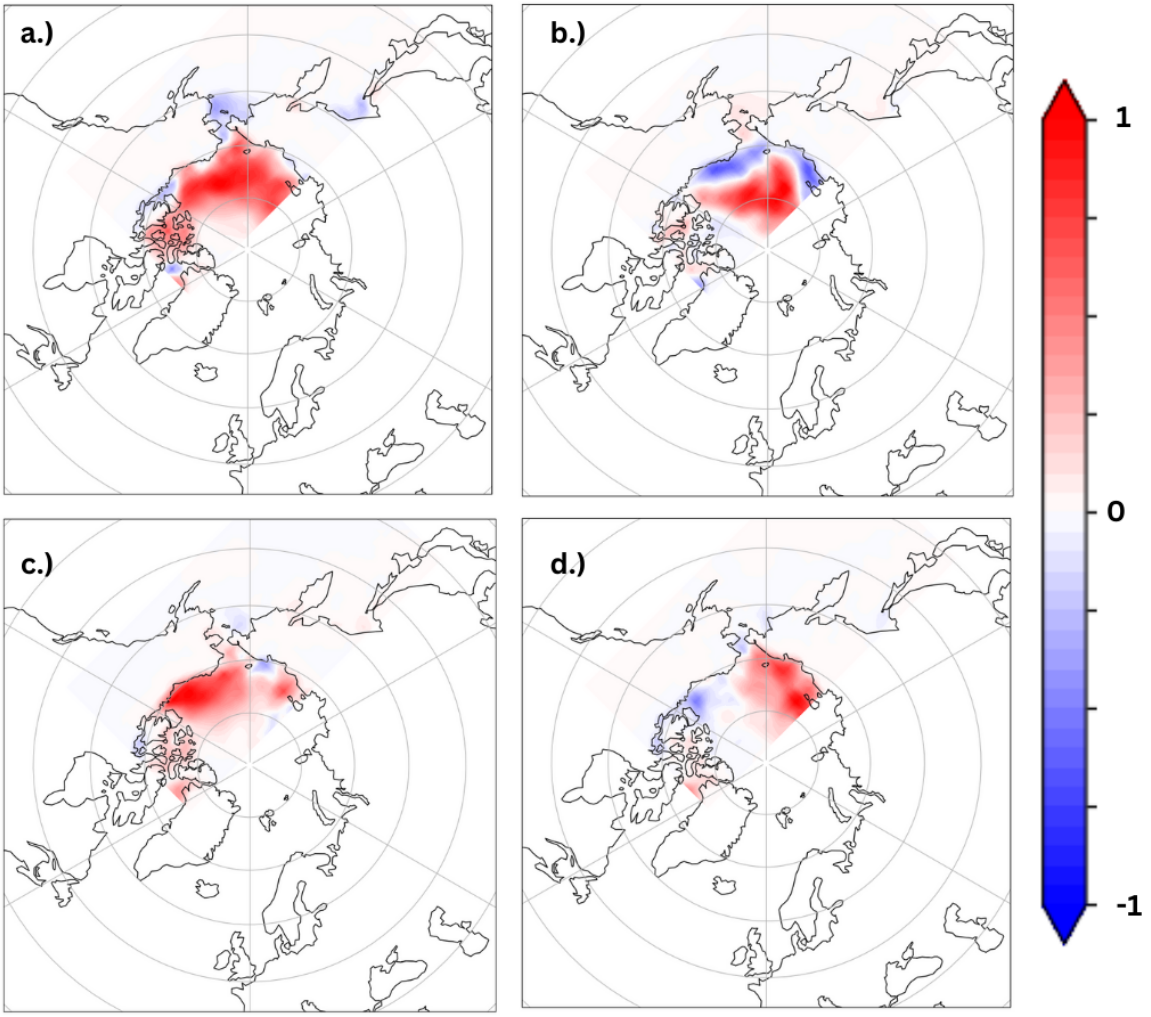


Figure 4.20: Normalized principal component timeseries 1-4 (a-d) projected onto daily change in sea ice concentration anomalies. The PCs are taken from the multivariate EOF of summer daily change in sea ice concentration, daily mean 2-m temperature anomalies, daily mean significant height of wind wave anomalies, and daily mean surface latent heat flux in the Pacific region. Reds indicate that the sea ice directly varies with sea ice and blues indicate indirect variation.

JJA Atlantic Combined

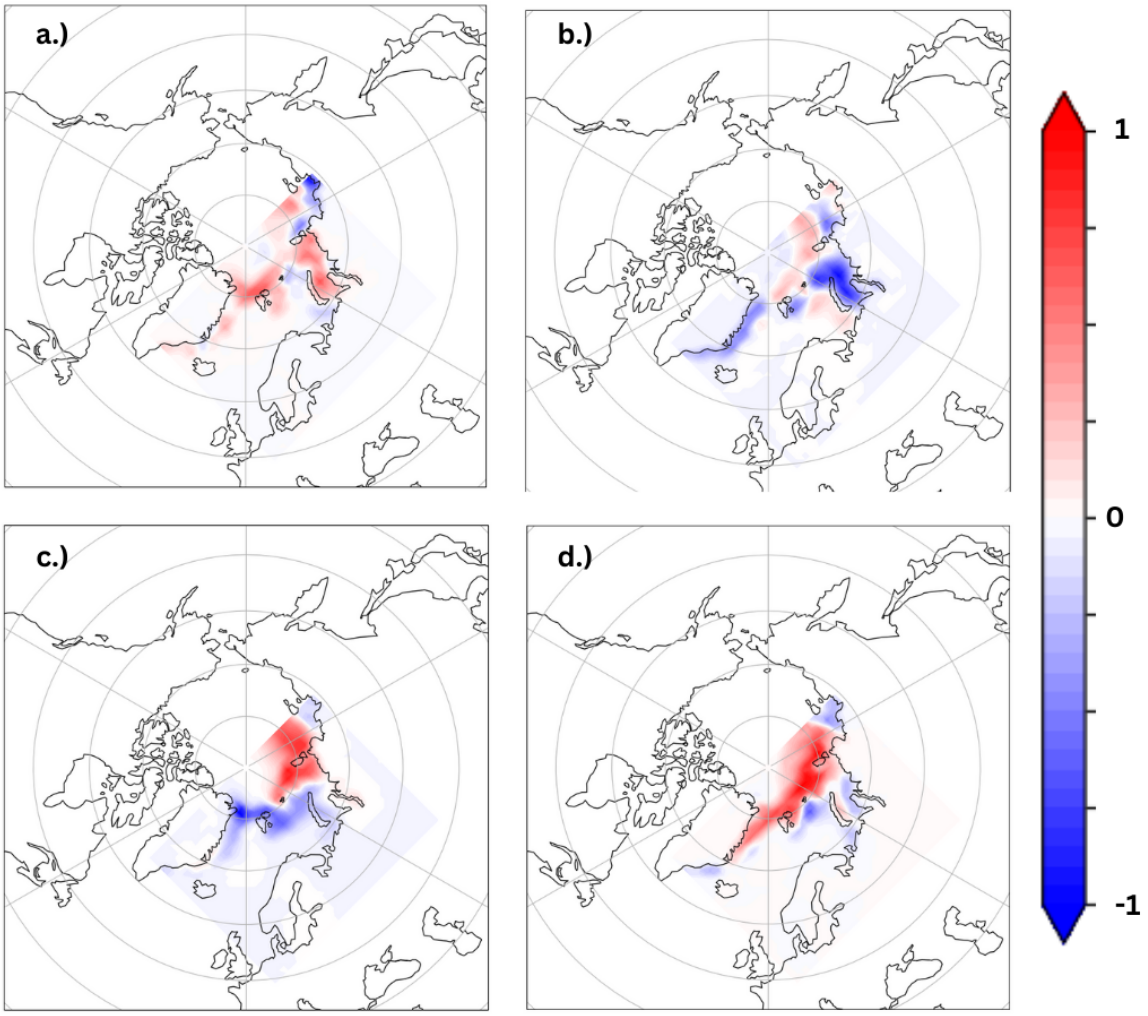


Figure 4.21: Normalized principal component timeseries 1-4 (a-d) projected onto daily change in sea ice concentration anomalies. The PCs are taken from the multivariate EOF of summer daily change in sea ice concentration, daily mean 2-m temperature anomalies, daily mean significant height of wind wave anomalies, and daily mean surface latent heat flux in the Atlantic region. Reds indicate that the sea ice directly varies with sea ice and blues indicate indirect variation.

DJF Pacific Combined

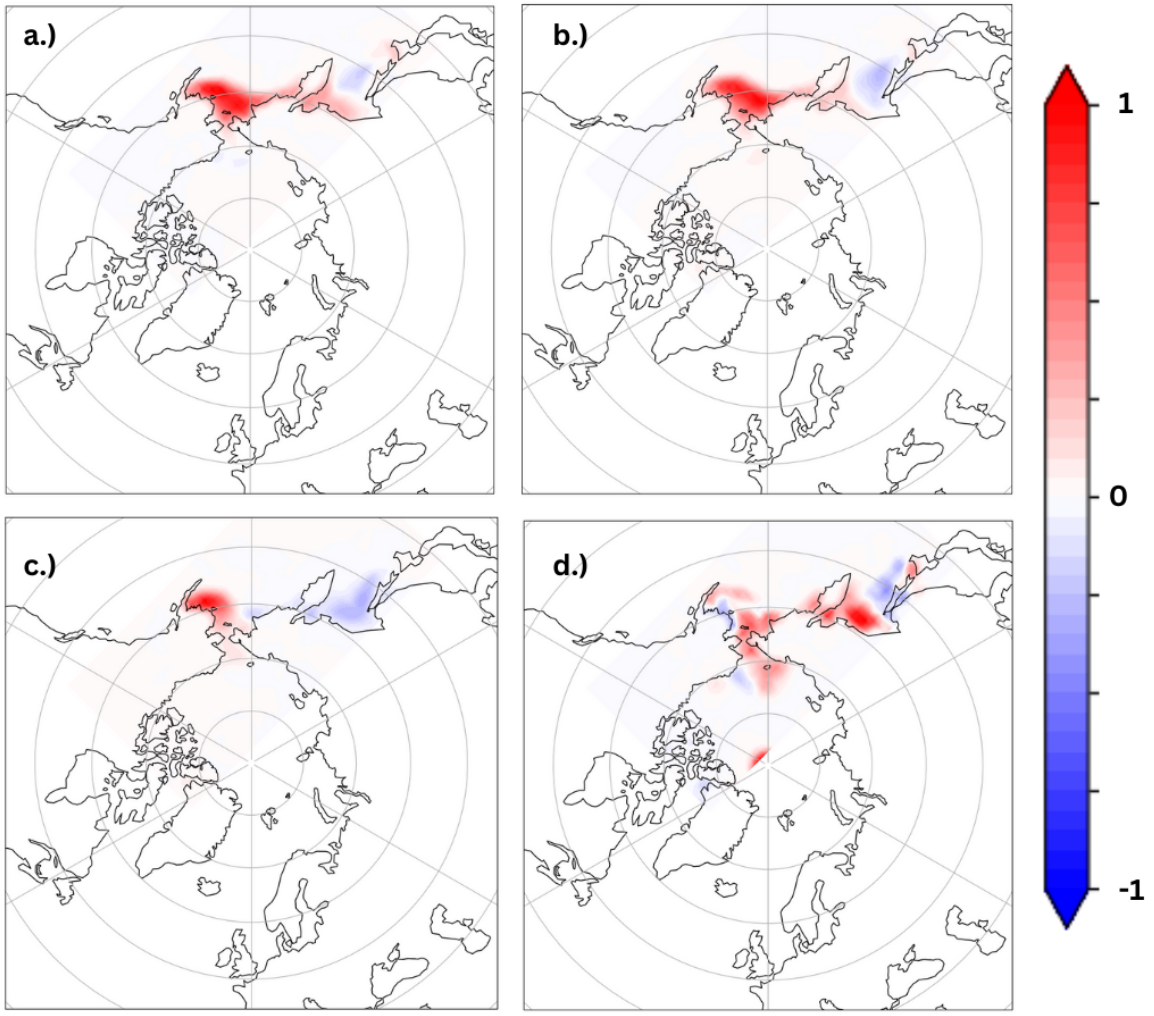


Figure 4.22: Normalized principal component timeseries 1-4 (a-d) projected onto daily change in sea ice concentration anomalies. The PCs are taken from the multivariate EOF of winter daily change in sea ice concentration, daily mean 2-m temperature anomalies, daily mean significant height of wind wave anomalies, and daily mean surface latent heat flux in the Pacific region. Reds indicate that the sea ice directly varies with sea ice and blues indicate indirect variation.

DJF Atlantic Combined

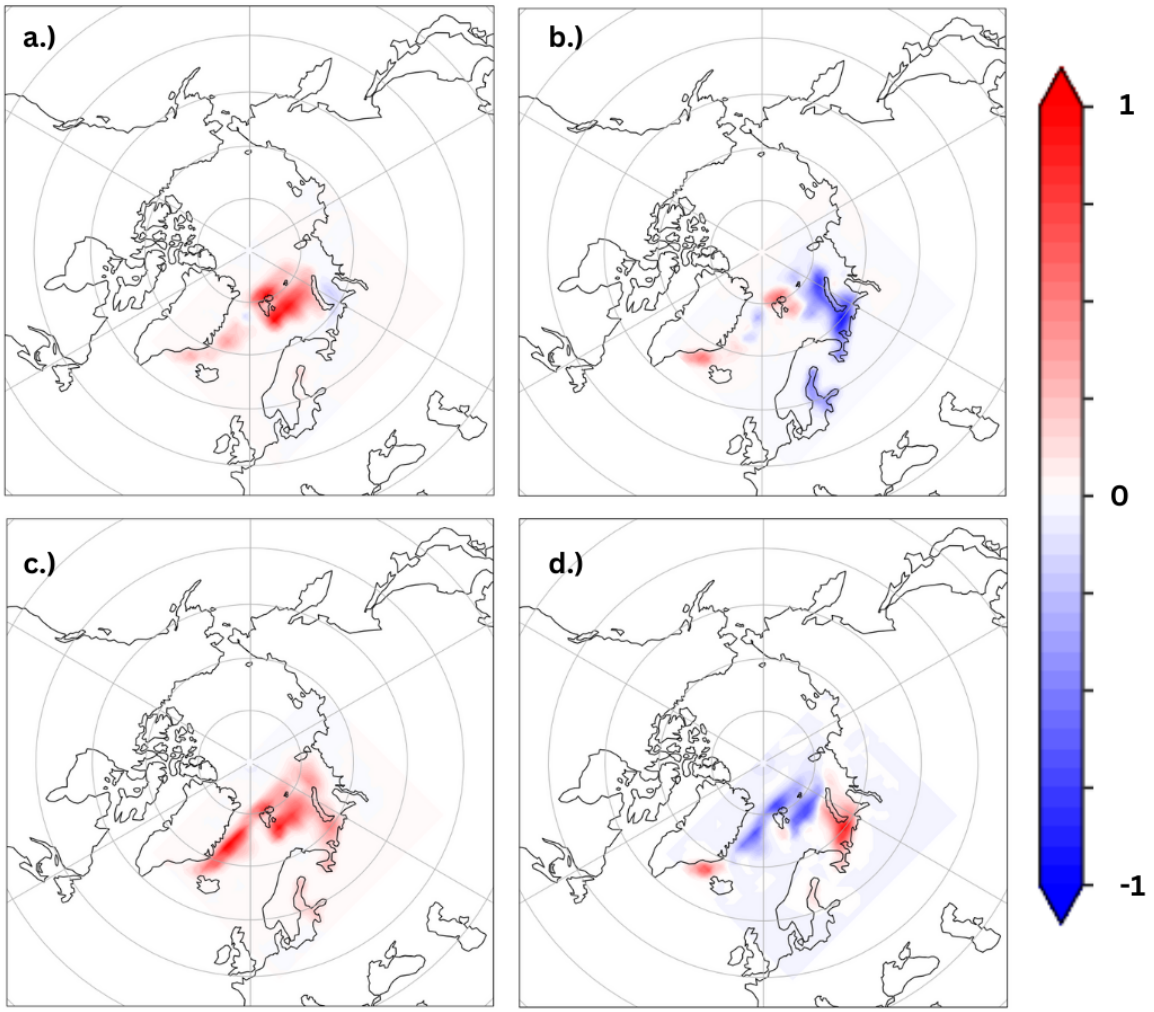


Figure 4.23: Normalized principal component timeseries 1-4 (a-d) projected onto daily change in sea ice concentration anomalies. The PCs are taken from the multivariate EOF of winter daily change in sea ice concentration, daily mean 2-m temperature anomalies, daily mean significant height of wind wave anomalies, and daily mean surface latent heat flux in the Atlantic region. Reds indicate that the sea ice directly varies with sea ice and blues indicate indirect variation.

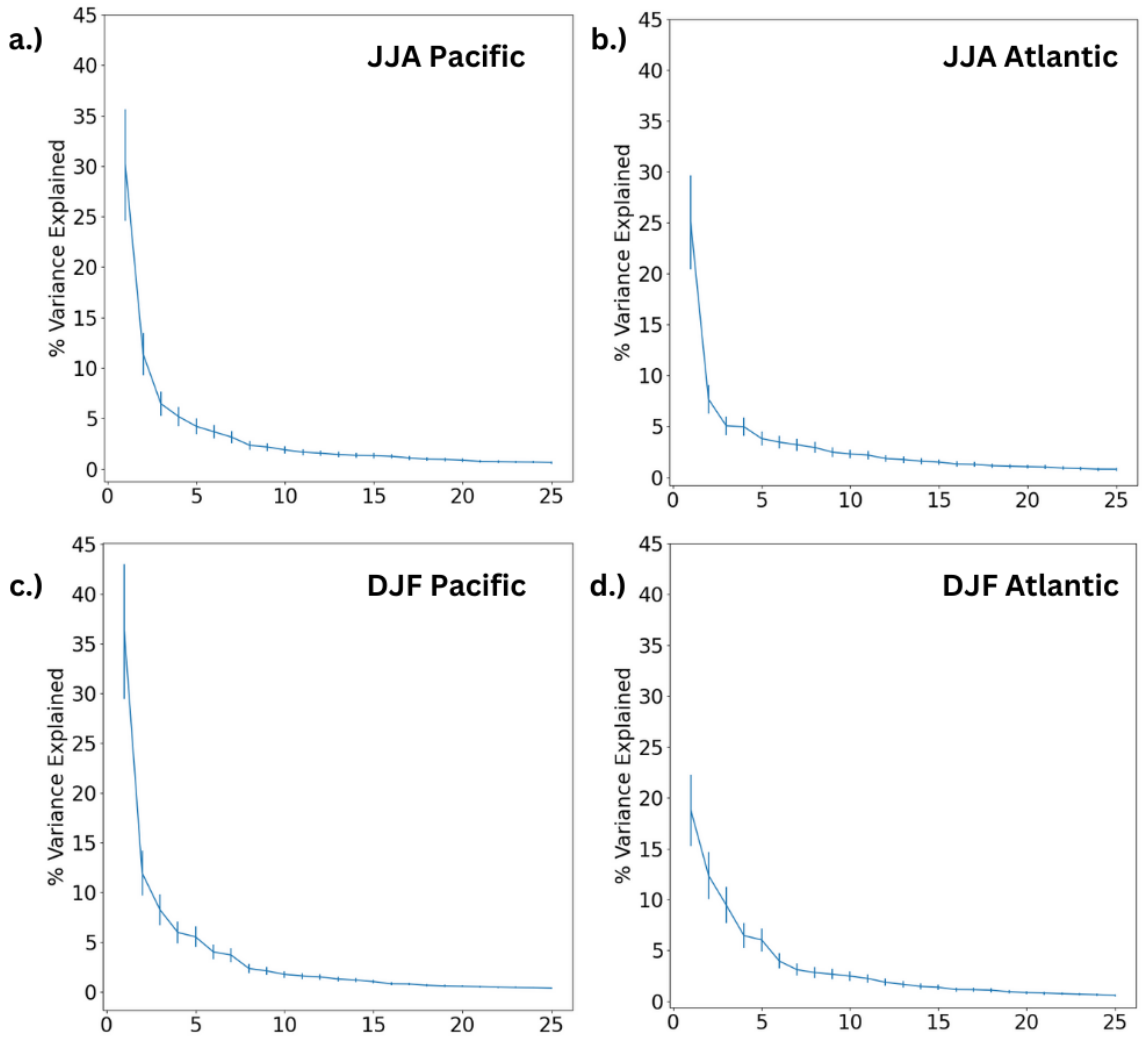


Figure 4.24: Percent variance explained versus mode of variability for combined multivariate EOFs by season and region. Error bars are calculated as North et al. (1982)

DJF No 2-m Temperature

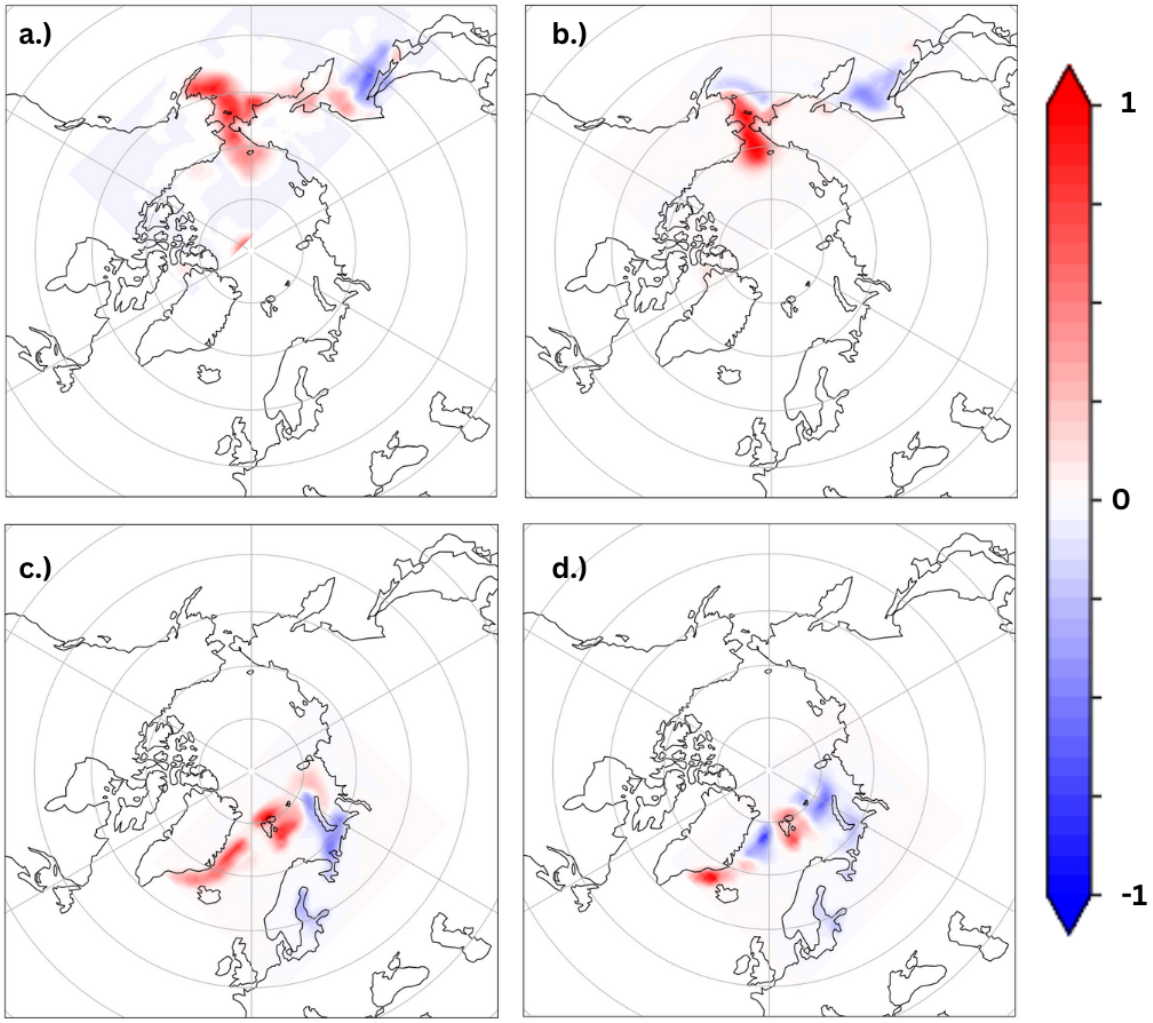


Figure 4.25: Normalized principal component timeseries 1 and 2 projected onto daily change in sea ice concentration anomalies in the Pacific (a and b) and Atlantic (c and d) regions. The PCs are taken from the multivariate EOF of winter daily change in sea ice concentration, daily mean significant height of wind wave anomalies, and daily mean surface latent heat flux. Reds indicate that the sea ice directly varies with sea ice and blues indicate indirect variation.

Chapter 5

One Dimensional Model

The purpose of these experiments is to quantify whether typical ocean waves are capable of significantly affecting sea ice floes in the MIZ. Since current climate models do not allow for these types of interactions between ocean waves and sea ice, we construct a one dimensional, beam bending model. This model will provide a better understanding of what properties of sea ice floes and ocean waves most affect the waves' ability to fracture sea ice.

There were a few caveats with the FEA solver used in this analysis. The solver is constructed to solve for static loads on structures such as buildings or bridges, not ice floes hundreds of meters long. Consequently, implementing multiple floes and forcings dynamically required manual updates is inefficient. The FEA solver is proprietary software, creating a wrapper for those updates is a task beyond the scope of this project. These inefficiencies limit the number of floes analyzed and the frequency of time sampling here. Additionally, in the following experiments all internal stresses are always found to be zero and the solver consistently warned that the Young's and Shear moduli were large. These warning support our assumption that the sea ice is brittle along its thickness axis, as discussed in Chapter 2. Other limitations that may affect these results are: 1.) waves equally act on the entire width of the floe 2.) ocean waves are normal to the ice floe and 3.) wave dispersion is zero.

Experiment 1 (Table 2.3) is the baseline. Most notably, there is sufficient force to fracture the sea ice in all ten floes and the maximum displacement of each floe exceeds ice thickness (Figure 5.1 a). Additionally, there is sufficient forcing in x at each floe boundary at multiple time steps to cause ridging (Figure 5.1 b). Wherever an arrow is present in Figure 5.1, the internal, horizontal forces exceed the material threshold for buckling. The direction of the arrow indicates the direction of the force. For ridging to occur, the internal

forces must exceed the buckling threshold under compression. In this experiment, ocean waves in this model are able to penetrate the MIZ with sufficient energy to fracture sea ice floes.

The first factor we vary is floe size. With L = 100 m (Experiment 2) there is still sufficient force from the waves to cause fracture in each floe (Figure 5.2 a). Vertical displacement of the floes tends to be less than 1 m, meaning that rafting is unlikely but there are sufficient forcings to result in ridging (Figure 5.2 b). Rafting can occur if floe displacement exceeds its thickness. When floe size is reduced to 10 m (Experiment 3), displacement becomes larger and the fracture threshold is exceeded more often than for smaller L (Figure 5.2 c). The initial displacement of nearly 8 m seems unlikely to be physically realized given the fact that the floe is likely to be fractured (Figure 5.2 c). Figure 5.2 d predominately indicates ridging. Consider floes 5 and 6, with end points at 50, 60, and 70 m, at the first time step, indicated in dark blue in Figure 5.2 d. The $\hat{x}$ force at 50 m is positive and negative at 70 m indicating compression where the floes' shared boundary, at 60 m. When this signal is present, it is likely that ridging would occur. Otherwise, when there is sufficient force but not the compression signal, ridging is still possible, but where it occurs is indeterminate.

In Experiment 4 we remove the slam force from our calculations. Excluding the slam force does not appreciably change the results from baseline (Figure 5.3). We attribute this lack of change to the magnitude of the drag force. The drag force is generally two orders of magnitude larger than the slam force.

We also note that $F_{drag} \propto L$, which helps to contextualize our results from Experiments 2 and 3. Increasing L to 100 m has little effect on whether or not the floe would fracture. Even though $F_{buoyancy} \propto L^2$, for the floe sizes in these experiments, $F_{buoyancy}$ is the same order of magnitude as F_{drag} or less in the case of L = 10 m. When L = 500 m (not shown), $F_{buoyancy} \approx 10^6$ kN but $F_{drag} \approx 10^5$ kN and the wave has little effect on sea ice.

This dependence on L over other factors for whether or not the sea ice will fracture is highlighted by the results for Experiments 5-10 that vary sea ice thickness (Figure 5.4),

wavelength (Figure 5.5), and wave amplitude (Figure 5.6). Varying sea ice thickness while maintaining its characteristic size has little to no effect on the wave's ability to cause ridging or rafting (Figure 5.4 b) but it does affect displacement and fracture (Figure 5.4 a). When the sea ice thickness is 0.5 m or less, fracture occurs less often than when the sea ice is thicker. This counter intuitive result likely comes from two compounding effects: first that $F_{drag} \propto h$ and secondly that the thinner ice experiences less vertical displacement. Even though proportionally the sea ice displaces nearly twice its thickness for $h <= 0.5$, which allows for ridging and rafting, the e^{kz} term in F_{drag} will be smaller, reducing the overall vertical forcing in.

Decreasing the wavelength from 100m to 50m increases the frequency of fracture but does not have a large effect on ridging or rafting (Figure 5.5). Lowering wavelength even further, from 50 m to 10 m, produces displacements and forces too large for the model to calculate and is only solved for the first three time steps. Vertical displacement approaching 160 m (Figure 5.5 c) is not physically plausible, the results suggest that waves are depositing most or all of its energy in the first few floes and not propagating further. Additionally, when wavelength is varied in the experiments, frequency is held constant, so as to not complicate the results but this is not necessarily physically realistic. Smaller wavelengths are likely to be associated with shorter periods. The relationship between wave frequency and sea ice is discussed in more detail below.

Varying wave amplitude from 3 to 5 m does not have a significant effect on ridging, rafting, or fracture (Figure 5.6). The main difference between the two experiments is that increasing the amplitude increases the sea ice displacement (Figure 5.6). Increasing the wave amplitude causes more energetic reactions in the sea ice, but since the ice can fracture with less energetic waves the increase does not result in more fracture based on our constrained model. The baseline amplitude of 3 m is chosen because it represents the lower end of wave heights associated with Arctic storms and 5 m represents the high end of that range (Stopa et al. 2016). Fundamentally, these results suggest that ocean waves associated

with strong surface winds are capable of causing fracture indicating that there may be some threshold wave height value where ocean waves transition from not being able to fracture sea ice to being able to.

In final set of experiments we vary wave frequency and attenuation factor since wave attenuation is a function of frequency. When $f = 0.45$ and $a = 10^{-4}$, the model becomes unsolvable after two time steps because of the enormous values for both displacement and total force (Figure 5.7). This is a similar scenario as to $\lambda = 10$ in Experiment 9. In experiment 12, $f = 0.3$ and $a = 10^{-3}$, there is only sufficient forcing to fracture the sea ice in the first seven floes (Figure 5.7). We also note that the initial displacement in that experiment is non-physical but represents highly dynamic sea ice reactions to the ocean wave.

Our primary goal with these experiments is to determine whether ocean waves can fracture sea ice in the MIZ. The question of whether sea ice will fracture appears to be primarily dependent on floe size, frequency, and attenuation factor. We propose that the ratio of F_{drag} to $F_{buoyancy}$ may determine whether the sea ice will fracture. That is, if $\frac{F_{drag}}{F_{buoyancy}} \gg 1$, then the sea ice will fracture, otherwise it will not.

Because F_{drag} and $F_{buoyancy}$ share several terms their ratio can be simplified:

$$\frac{F_{drag}}{F_{buoyancy}} = \frac{1}{2}\frac{\rho_{sw} C_d L h u|u|}{\rho_{sw} g L^2 h} = \frac{1}{2}\frac{C_d u|u|}{gL} \tag{1}$$

$$= \frac{1}{2}\frac{C_d 2\pi^2 H^2 f^2}{gL} e^{-2ax} e^{2kz} sin(kx - \omega t)|sin(kx - \omega t)|. \tag{2}$$

For this factor, we assume the sine terms are at their maxima of one. We also assume that $z = 0$, and that both g and π^2 are approximately 10. Then (2) becomes

$$\approx \frac{C_d H^2 f^2}{L} e^{-2ax}. \tag{3}$$

While the efficacy of this factor in climate model parameterizations is beyond the scope of this work, we present a few calculations to support our conclusion in Table 5.1. The values in Table 5.1 show that in all cases where $\frac{F_{drag}}{F_{buoyancy}} \gg 1$ and there is a corresponding experiment in Table 2.3, the ocean waves cause sea ice fracture. The same is true for

$\frac{F_{drag}}{F_{buoyancy}} \ll 1$ and no sea ice fracture. When the ratio is close to one, it is not immediately clear whether there is fracture. In the cases present in Table 5.1, when the ratio is close to 1 there is sea ice fracture in the corresponding experiments. However, since the ratio does not depend on sea ice thickness, all cases in Figure 5.4 would return a value of 4.5 but when $h \leq 0.5$ m fracture is limited.

In summary, ocean waves resulting from strong surface winds are able to fracture sea ice and cause ridging and rafting for hundreds of meters into the MIZ. This result is in line with some observational studies of sea ice (Asplin et al. 2012). The most energetic waves, those with shorter wavelengths and higher frequencies, seem to be the most limited in their ability to affect large areas of sea ice. Longer wavelength and lower frequency waves appear to have more of a net effect on the sea ice because of their lower attenuation factor, allowing them to penetrate more than a kilometer into the ice in this model. While more work is needed to determine if the relationship between F_{drag} and $F_{buoyancy}$ is an effective tool for parameterization of sea ice floes in climate models, results here support continued work in this area. As discussed in detail in Chapter 3, improving model performance in these small spatial and temporal scales is key for improving their overall representation of sea ice.

$F_{drag}/F_{buoyancy}$ Calculations							
	L	C_d	H	f	a	x	$\frac{F_{drag}}{F_{buoyancy}}$
1	50	2.5×10^3	3	0.1	10^{-5}	0	4.5
2	100	2.5×10^3	3	0.1	10^{-5}	0	2.25
3	500	2.5×10^3	3	0.1	10^{-5}	0	0.45
4	50	2.5×10^3	1	0.1	10^{-5}	0	0.5
5	50	2.5×10^3	5	0.1	10^{-5}	0	11.8
6	50	2.5×10^3	3	0.3	10^{-4}	0	40.5
7	50	2.5×10^3	3	0.3	10^{-4}	10 km	5.48
8	50	2.5×10^3	3	0.45	10^{-3}	0	91
9	50	2.5×10^3	3	0.45	10^{-3}	3 km	0.23

Table 5.1: Values used to calculate $F_{drag}/F_{buoyancy}$ for different sea ice and ocean wave properties. The far right column shows the calculated ratio and is shaded in red if the ratio indicates that the sea ice will not fracture, green if the sea ice will fracture, and light green if the ratio is indeterminate but the corresponding experiment in Table 2.3 indicates sea ice fracture. There were no cases where the ratio is indeterminate but the corresponding experiment indicated no fracture.

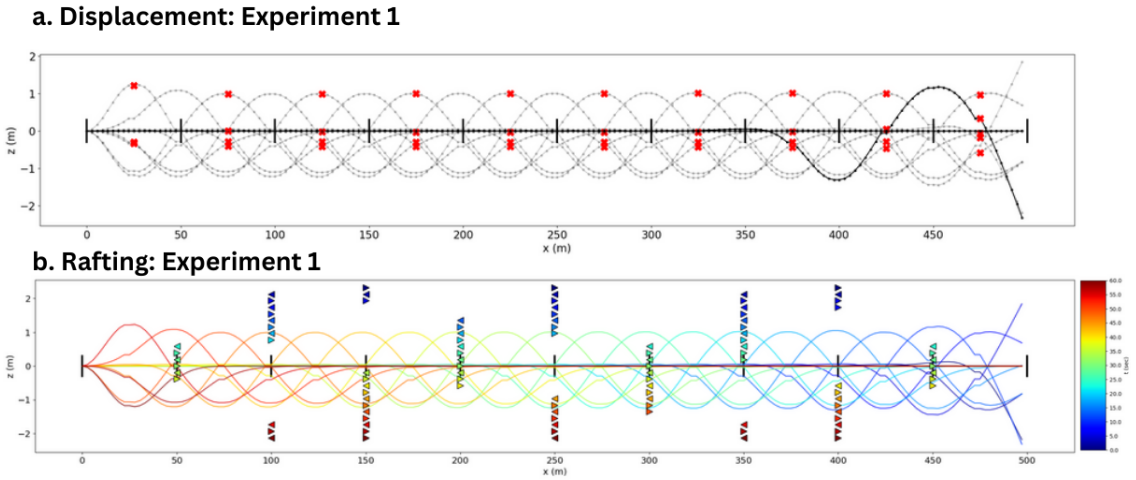


Figure 5.1: Displacement of sea ice floes from the one dimensional sea ice model forced by a single ocean wave. The displacement results from each time step (a) is plotted in black with the time of largest displacement highlighted. Locations where the shear force exceeds the fracture threshold are marked by red x's. In (b), colors correspond to the time step. Locations where the shear force in $\hat{x}$ exceeds the ridging threshold are marked by arrowheads pointing in the direction the force is acting. The boundaries between sea ice floes are shown with vertical black lines. Both plots correspond to experiment 1 in Table 2.3.

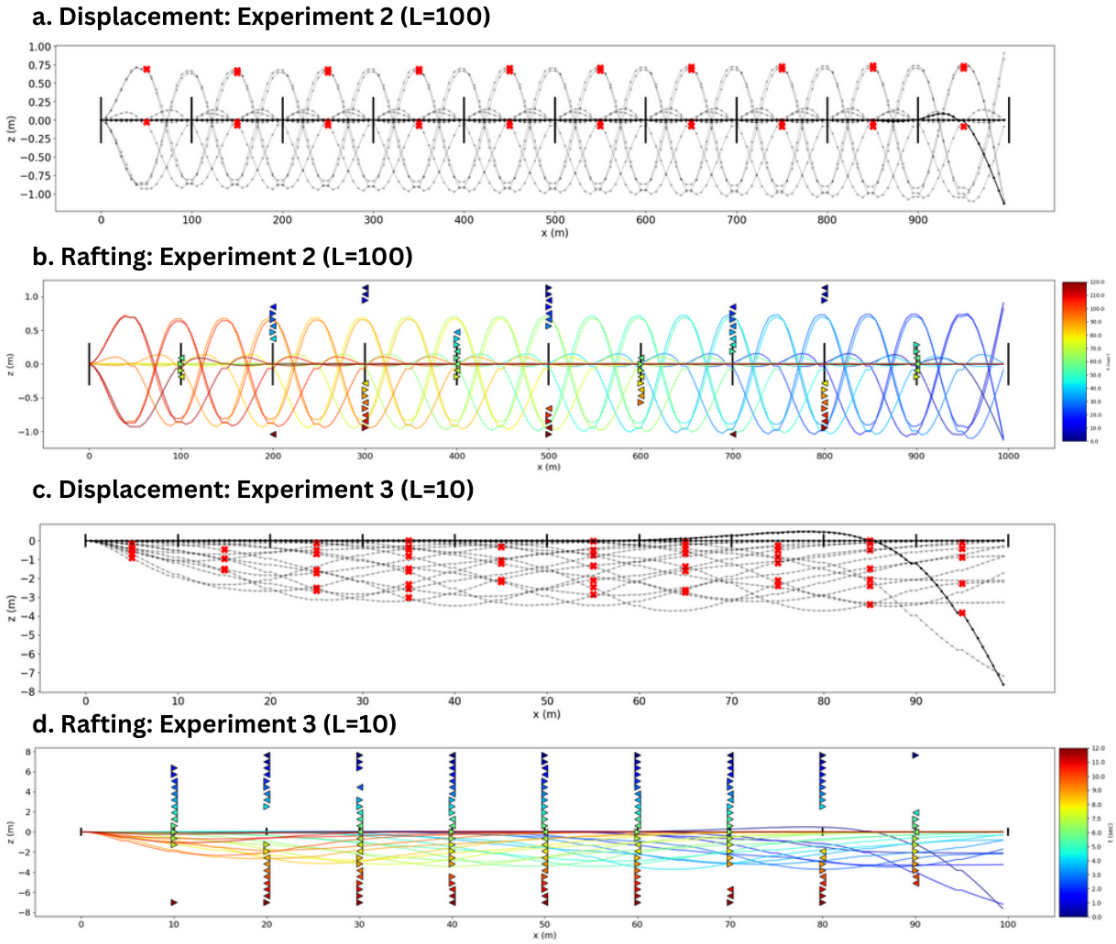


Figure 5.2: Displacement of sea ice floes from the one dimensional sea ice model forced by a single ocean wave. The displacement results from each time step (a and c) is plotted in black with the time of largest displacement highlighted. Locations where the shear force exceeds the fracture threshold are marked by red x's. In (b) and (d), colors correspond to the time step. Locations where the shear force in $\hat{x}$ exceeds the ridging threshold are marked by arrowheads pointing in the direction the force is acting. The boundaries between sea ice floes are shown with vertical black lines. Plots (a) and (b) correspond to experiment 2 in Table 2.3, and plots (c) and (d) to experiment 3.

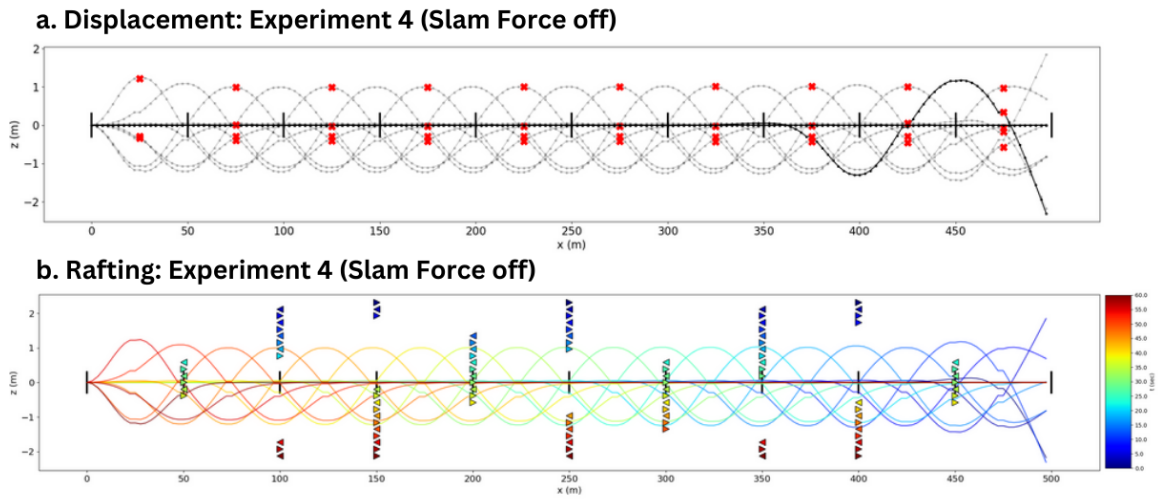


Figure 5.3: Displacement of sea ice floes from the one dimensional sea ice model forced by a single ocean wave. The displacement results from each time step (a) is plotted in black with the time of largest displacement highlighted. Locations where the shear force exceeds the fracture threshold are marked by red x's. In (b), colors correspond to the time step. Locations where the shear force in $\hat{x}$ exceeds the ridging threshold are marked by arrowheads pointing in the direction the force is acting. The boundaries between sea ice floes are shown with vertical black lines. Both plots correspond to experiment 4 in Table 2.3.

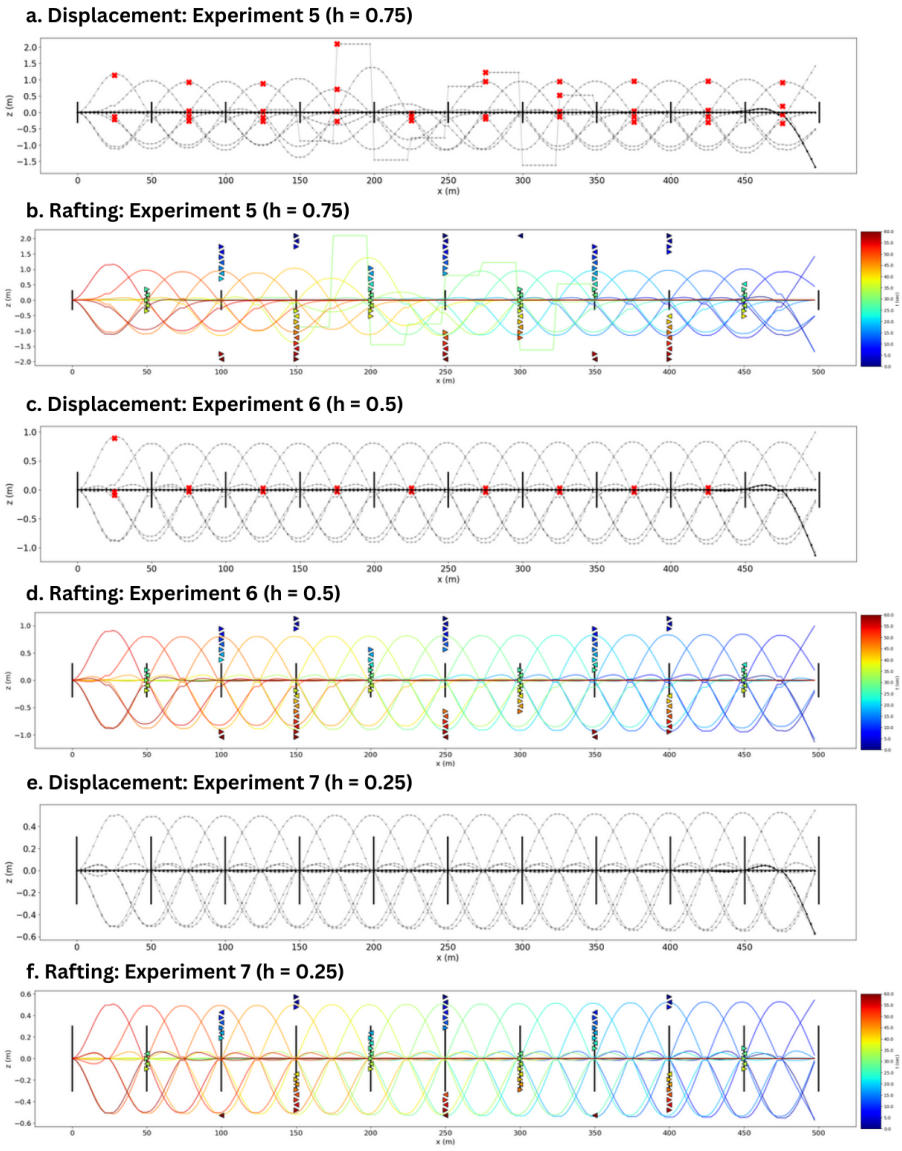


Figure 5.4: Displacement of sea ice floes from the one dimensional sea ice model forced by a single ocean wave. The displacement results from each time step (a, c, and e) is plotted in black with the time of largest displacement highlighted. Locations where the shear force exceeds the fracture threshold are marked by red x's. In (b), (d) and (f), colors correspond to the time step. Locations where the shear force in $\hat{x}$ exceeds the ridging threshold are marked by arrowheads pointing in the direction the force is acting. The boundaries between sea ice floes are shown with vertical black lines. Plots (a) and (b) correspond to experiment 5 in Table 2.3, plots (c) and (d) to experiment 6, and plots (e) and (f) to experiment 7.

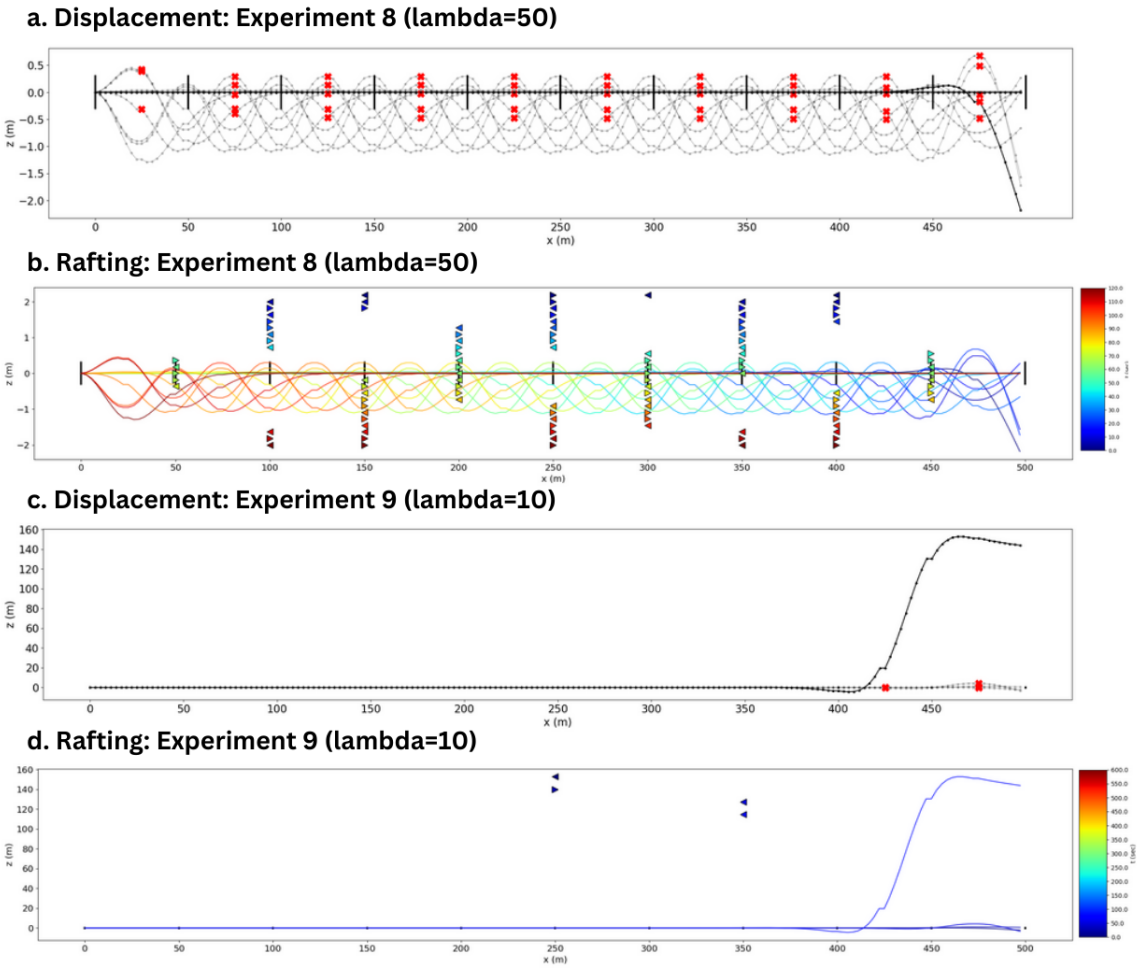


Figure 5.5: Displacement of sea ice floes from the one dimensional sea ice model forced by a single ocean wave. The displacement results from each time step (a and c) is plotted in black with the time of largest displacement highlighted. Locations where the shear force exceeds the fracture threshold are marked by red x's. In (b) and (d), colors correspond to the time step. Locations where the shear force in $\hat{x}$ exceeds the ridging threshold are marked by arrowheads pointing in the direction the force is acting. The boundaries between sea ice floes are shown with vertical black lines. Plots (a) and (b) correspond to experiment 8 in Table 2.3, and plots (c) and (d) to experiment 9.

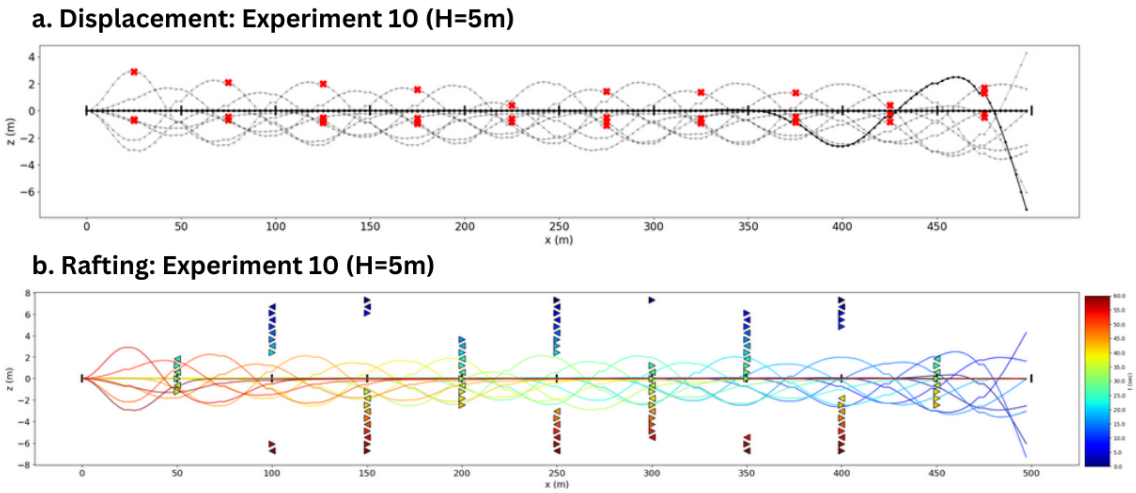


Figure 5.6: Displacement of sea ice floes from the one dimensional sea ice model forced by a single ocean wave. The displacement results from each time step (a) is plotted in black with the time of largest displacement highlighted. Locations where the shear force exceeds the fracture threshold are marked by red x's. In (b), colors correspond to the time step. Locations where the shear force in $\hat{x}$ exceeds the ridging threshold are marked by arrowheads pointing in the direction the force is acting. The boundaries between sea ice floes are shown with vertical black lines. Both plots correspond to experiment 10 in Table 2.3.

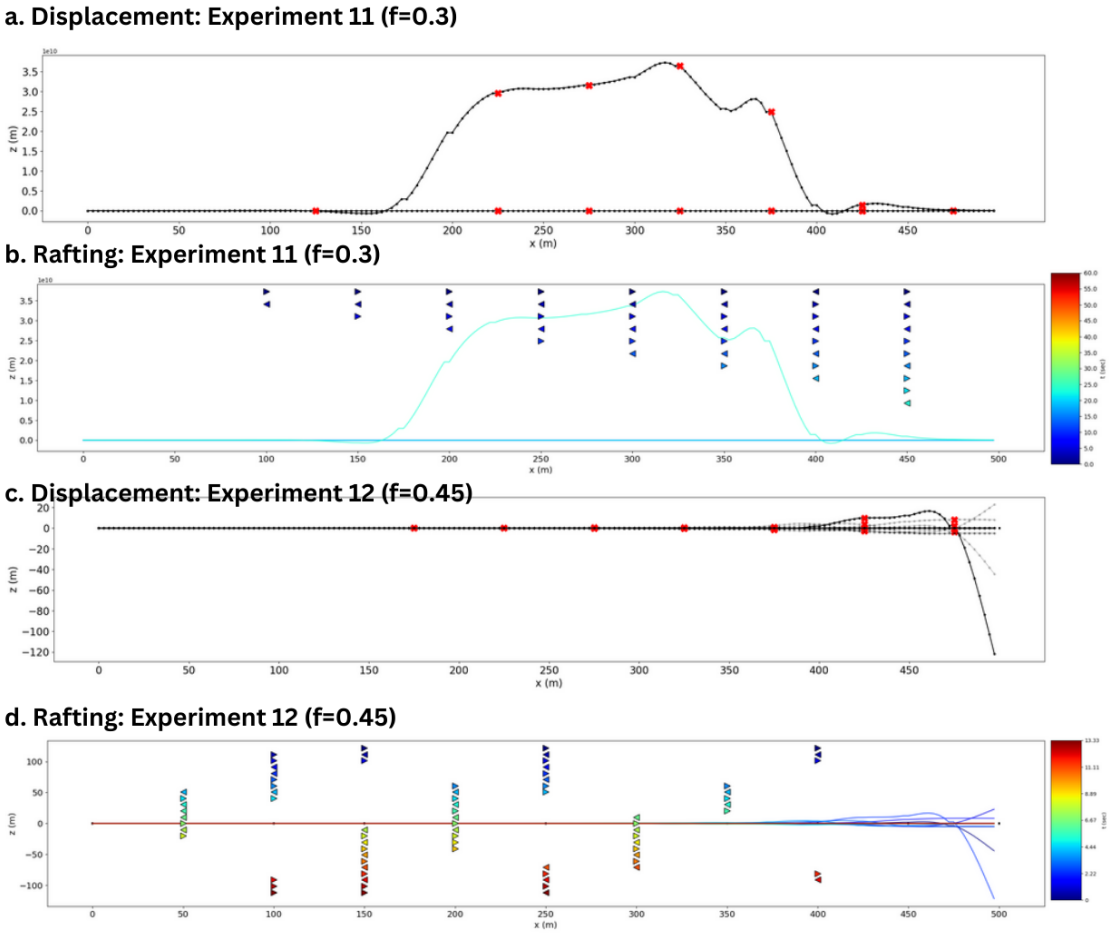


Figure 5.7: Displacement of sea ice floes from the one dimensional sea ice model forced by a single ocean wave. The displacement results from each time step (a and c) is plotted in black with the time of largest displacement highlighted. Locations where the shear force exceeds the fracture threshold are marked by red x's. In (b) and (d), colors correspond to the time step. Locations where the shear force in $\hat{x}$ exceeds the ridging threshold are marked by arrowheads pointing in the direction the force is acting. The boundaries between sea ice floes are shown with vertical black lines. Plots (a) and (b) correspond to experiment 11 in Table 2.3, and plots (c) and (d) to experiment 12.

Chapter 6

Conclusions

The goal of this dissertation is to determine what causes VRILEs and subseasonal sea ice changes more generally. Of the three known mechanisms for these sea ice changes, atmospheric heat transport, ocean heat transport via up-welling, and ocean wave dynamics, we focus our attention on ocean wave dynamics and, to a lesser degree, atmospheric heat transport. Focus is given to ocean wave dynamics because of the lack of representation of coupled sea ice and ocean wave dynamics in climate models, specifically CESM2. We choose to focus on ocean wave dynamics because atmospheric heat and moisture transport is well represented in CESM2 (Benedict et al. 2019; Song et al. 2021; Karwat et al. 2024). Since that is the case but, as we demonstrate in Chapter 3, CESM2 does a poor job of representing VRILEs, it suggests that one or both of the ocean mechanisms are important to form VRILEs. Since coupled ocean and sea ice models assume that ocean waves are not capable of affecting sea ice beyond the edge of the MIZ and thus ignore their effects entirely we test that assumption.

Our first approach is to qualify how well VRILEs are captured in CESM2, both in the LENS and in S2S reforecasts. CESM2 LENS does not generally simulate significant changes in sea ice at timescales below 20 days (Figure 3.3) and when VRILEs are identified using the same methods as in observations, the VRILEs are approximately an order of magnitude too small (Figure 3.6). However, even though these events are far too small, they are associated with surface cyclones even though they miss the full atmospheric signal associated with observed VRILEs in ERA5 (Figures 3.8 and 3.9). These conclusions are mirrored in the reforecast case studies. The reforecasts underestimate sea ice loss even though they reasonably represent the associated surface cyclones (Figures 3.11, 3.13, 3.15, and 3.17). Additionally, Arctic surface cyclones tracks in CESM2 LENS and ERA5 show

broad alignment of the two datasets, consistent with other, more detailed, studies on Arctic cyclones in (Priestley et al. 2020) and poleward moisture transport in CESM2 LENS (Benedict et al. 2019).

A conclusion from the above results is that CESM2 is not a practical tool for studying VRILEs in its current form. Secondarily, because CESM2 represents surface cyclones well in both LENS and S2S data, we propose that the anemic sea ice responses are not due to a lack of atmospheric thermodynamic forcing but rather due to a lack of ocean forcing. Whether that missing mechanism is ocean thermodynamics or wave dynamics is indeterminable from these results. However, the fact that ocean wave dynamics effecting sea ice are missing entirely from CESM2 prompt further investigation of that mechanism.

The second approach taken to understand the mechanisms behind short timescale sea ice loss is statistical. With this approach we find that between 2-m temperature, significant height of wind waves, and mean surface latent heat flux, warm 2-m temperature anomalies have the strongest associations with wintertime subseasonal sea ice loss (Figures 4.22 and 4.23), followed by surface latent heat flux and significant height of wind waves (Figure 4.25). In the summertime, surface latent heat flux has the strongest associations with sea ice loss followed by significant height of wind waves (Figures 4.20 and 4.21).

At first glance these results seem incongruent with those from the comparative analysis. In the comparative analysis, we see weak sea ice responses to surface cyclones, the most likely source for heat transport, and in the multivariate EOFs, there is a strong covariance of latent heat anomalies and changes in sea ice concentration. If those atmospheric thermodynamic effects are important for sea ice loss then why is the sea ice response in CESM2 so small? There are several potential answers to that question. The data analyzed using multivariate EOFs are filtered to remove the climate trend and seasonal cycle by subtracting the linear trend and monthly climatological mean values from the data. Processing the data in this manner retains signals with a period of approximately 30 days or less. Therefore LH having a stronger covariance with daily changes in sea ice extent than significant height

of ocean waves may be indicating a strong relationship between sea ice and LH at those longer time scales but not necessarily on the scale of days for VRILEs. Another possibility is that the heating terms work more efficiently once ocean waves have physically broken up the ice floes. That is, the LH is what actually causes sea ice loss, thus its prominence in the EOF analysis, but its effectiveness is dependent on the ocean waves. If that is the case, then the lack of sea ice loss in CESM2 LENS could be related to the floes being too large to be affected by the atmospheric heating terms.

Surface cyclones are known to affect sea ice on average differently at different times of the year (Finocchio and Doyle 2021; Intrieri et al. 2002; Kriegsmann and Brümmer 2014). In the summer, a cyclone interacts with the sea ice, its two primary effects are to decrease the net surface shortwave flux and increase the sensible heat flux (Finocchio and Doyle 2021). The earlier in the melt season, there is a greater importance to the shortwave flux decreasing sea ice melt. While clouds from surface cyclones still reduce the surface shortwave flux later in the summer, it loses its ties to decreased melt in July and August (Finocchio et al. 2020). However, regardless of season the increase in sensible heat flux from the cyclone is unlikely to be sufficient to cause significant ice loss for a VRILE (Finocchio and Doyle 2021).

While it has been previously assumed that ocean waves do not play a significant role in ice floe distribution, the one dimensional experiments lends support to their importance. Of particular interest is the sea ice response to the waves with relatively long periods and wavelengths. Consider two waves that are identical, save for their wavelength and period, where one has a short period and wavelength and the other a long period and wavelength. These two waves are capable of transferring the same amount of energy to the sea ice. Because the attenuation factor is much stronger for the short period wave, that energy will be confined to the sea ice edge. But the attenuation factor for the long period wave is orders of magnitude less than the short period wave. It is these long period waves that are capable of penetrating deep into the MIZ, easily over a kilometer by these estimates, and will likely

have the largest net effect on the sea ice. The effect of the high frequency wave is limited to the sea ice edge. Though if these high frequency waves are continuously generated near the sea ice edge they could have a compounding effect.

Currently, models assume that floe size is a constant. However, research is being done to introduce floe size distributions into parameterization schemes (Bateson et al. 2020; Hwang and Wang 2022). Investigating the effects of including floe size distributions and incorporating the ratio of F_{drag} to $F_{buoyancy}$ for determining the effects of ocean waves on those floes is a key area of future work. This includes evaluating changes to the model's performance in capturing subseasonal sea ice processes, sea ice extent interannual variability, and VRILE size, location, and associated atmospheric conditions. Sea ice transport may also be significantly affected by those factors.

The relative importance of ocean heat transport via vertical mixing is not evaluated here and therefore could be an important factor. Further work is necessary to quantify both the importance of this effect and its representation in coupled models. Ocean boundary layer mixing can be an important factor for sea ice loss, as seen with the Great Arctic Cyclone of 2012 (Zhang et al. 2013) but it remains to be seen if it is generally a strong driver. Additionally it must be determined whether climate models accurately represent surface wind driven mixing compared to observations.

At the outset of this research, our primary goal was to determine which of the proposed mechanisms for VRILE formation has the greatest affect on sea ice. After approaching the problem from multiple perspectives, it seems that these effects cannot be easily disentangled and are likely interdependent. Figure 6.1 presents a diagram of these three processes working in tandem to produce the sea ice loss observed in VRILEs. This is proposed as a general process for VRILEs in all seasons with the caveat that sensible heat flux from the cyclone may play a more important role in winter VRILEs than summer based on the importance of 2-m temperature anomalies in winter subseasonal sea ice processes discussed in Chapter 4.

What is clear is that subseasonal sea ice dynamics are complicated and deeply coupled to both atmospheric and ocean processes. It is also clear that there is much room to grow in model representation of these processes. Improved model performance is important not only for the improvement of general climate model representation and prediction of the Arctic, but for forecast tools for ocean vessels traversing the rapidly changing region.

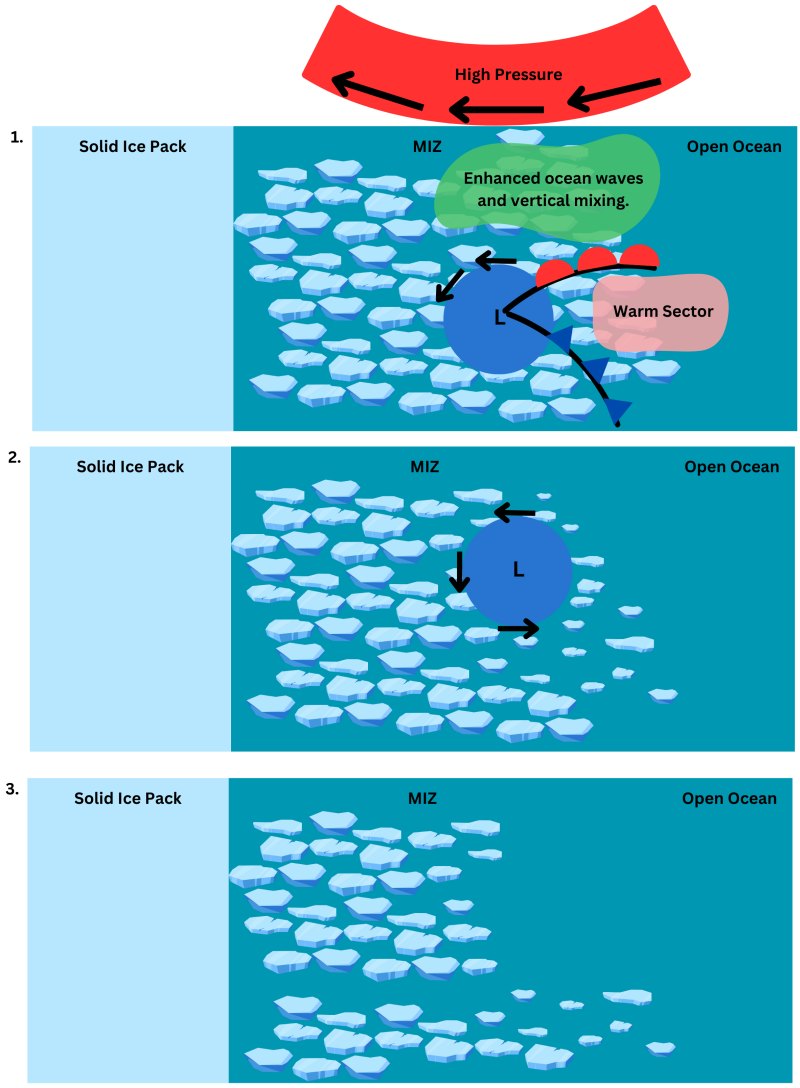


Figure 6.1: Schematic depicting the proposed mechanisms for the formation of VRILEs. First, a surface cyclone and a high pressure region set up across the MIZ. The winds from the pressure gradient create a region of enhanced ocean waves and ocean vertical mixing. Additionally, the cyclone's warm sector represents a region of enhanced sensible heat fluxes. As the cyclone moves through the MIZ (2), the floes in the regions highlighted in (1) are reduced in size. This reduction make transport out of the MIZ by the cyclone's winds easier, resulting in the large sea ice loss in panel (3). The smaller floes can also be further melted by the cyclone's warm sector.

Bibliography

Aizawa, T. and H. Tanaka, 2016: Axisymmetric structure of the long lasting summer arctic cyclones. *Polar Science*, **10 (3)**, 192–198.

Aizawa, T., H. Tanaka, and M. Satoh, 2014: Rapid development of arctic cyclone in june 2008 simulated by the cloud resolving global model nicam. *Meteorology and Atmospheric Physics*, **126**, 105–117.

Årthun, M., T. Eldevik, L. Smedsrud, Ø. Skagseth, and R. Ingvaldsen, 2012: Quantifying the influence of atlantic heat on barents sea ice variability and retreat. *Journal of Climate*, **25 (13)**, 4736–4743.

Asplin, M. G., R. Galley, D. G. Barber, and S. Prinsenberg, 2012: Fracture of summer perennial sea ice by ocean swell as a result of arctic storms. *Journal of Geophysical Research: Oceans*, **117 (C6)**.

Asplin, M. G., R. Scharien, B. Else, S. Howell, D. G. Barber, T. Papakyriakou, and S. Prinsenberg, 2014: Implications of fractured arctic perennial ice cover on thermodynamic and dynamic sea ice processes. *Journal of Geophysical Research: Oceans*, **119 (4)**, 2327–2343.

Barnhart, K. R., C. R. Miller, I. Overeem, and J. E. Kay, 2016: Mapping the future expansion of arctic open water. *Nature Climate Change*, **6 (3)**, 280.

Barros, R., 2002: Finite element modelling of floating pier units in personal computers. *WIT Transactions on The Built Environment*, **62**.

Bateson, A. W., D. L. Feltham, D. Schröder, L. Hosekova, J. K. Ridley, and Y. Aksenov, 2020: Impact of sea ice floe size distribution on seasonal fragmentation and melt of arctic sea ice. *The Cryosphere*, **14 (2)**, 403–428.

Bateson, A. W., D. L. Feltham, D. Schröder, Y. Wang, B. Hwang, J. K. Ridley, and Y. Aksenov, 2022: Sea ice floe size: its impact on pan-arctic and local ice mass and required model complexity. *The Cryosphere*, **16 (6)**, 2565–2593.

Benedict, J. J., A. C. Clement, and B. Medeiros, 2019: Atmospheric blocking and other large-scale precursor patterns of landfalling atmospheric rivers in the north pacific: A cesm2 study. *Journal of Geophysical Research: Atmospheres*, **124 (21)**, 11 330–11 353.

Bi, H., et al., 2020: Arctic multiyear sea ice variability observed from satellites: a review. *Journal of oceanology and limnology*, **38 (4)**, 962–984.

Blanchard-Wrigglesworth, E., M. Webster, L. Boisvert, C. Parker, and C. Horvat, 2022: Record arctic cyclone of january 2022: Characteristics, impacts, and predictability. *Journal of Geophysical Research: Atmospheres*, **127 (21)**, e2022JD037 161.

Blunden, J. and D. S. Arndt, 2012: State of the climate in 2011. *Bulletin of the American Meteorological Society*, **93 (7)**, S1–S282.

Bouchat, A. and B. Tremblay, 2017: Using sea-ice deformation fields to constrain the mechanical strength parameters of geophysical sea ice. *Journal of Geophysical Research: Oceans*, **122 (7)**, 5802–5825.

Bryson, R. A., 1965: Air masses, streamlines, and the boreal forest. *Geogr. Bull*, **8**, 228–269.

Burgard, C. and D. Notz, 2017: Drivers of arctic ocean warming in cmip5 models. *Geophysical Research Letters*, **44 (9)**, 4263–4271.

Cai, L., V. A. Alexeev, J. Zhang, and J. E. Walsh, 2023: Persistent impact of winter atmospheric circulation anomalies on arctic sea ice. *Environmental Research Communications*, **5 (10)**, 101 002.

Caian, M., T. Koenigk, R. Döscher, and A. Devasthale, 2018: An interannual link between arctic sea-ice cover and the north atlantic oscillation. *Climate dynamics*, **50**, 423–441.

Cavalieri, D. J. and C. L. Parkinson, 2012: Arctic sea ice variability and trends, 1979–2010. *The Cryosphere*, **6 (4)**, 881–889.

Cavallo, S. M., M. E. Frank, and C. M. Bitz, ????: Sea ice loss in association with arctic cyclones. *In preparation*.

Cavallo, S. M. and G. J. Hakim, 2009: Potential vorticity diagnosis of a tropopause polar cyclone. *Monthly Weather Review*, **137 (4)**, 1358–1371.

Cavallo, S. M. and G. J. Hakim, 2010: Composite structure of tropopause polar cyclones. *Monthly Weather Review*, **138 (10)**, 3840–3857.

Cavallo, S. M. and G. J. Hakim, 2013: Physical mechanisms of tropopause polar vortex intensity change. *Journal of the atmospheric sciences*, **70 (11)**, 3359–3373.

Cavallo, S. M., W. C. Skamarock, and N. Szapiro, 2016: Extended range predictions over the arctic with the model for the prediction across scales (mpas). *DRI meeting for seasonal prediction*, Monterey, CA, Naval Research Labratory.

Chan, P., et al., 2017: Multicentennial record of labrador sea primary productivity and sea-ice variability archived in coralline algal barium. *Nature communications*, **8 (1)**, 1–10.

Chang, X., W. Liu, G. Zuo, Y. Dou, and Y. Li, 2021: Research on ultrasonic-based investigation of mechanical properties of ice. *Acta Oceanologica Sinica*, **40**, 97–105.

Clancy, R., C. M. Bitz, E. Blanchard-Wrigglesworth, M. C. McGraw, and S. M. Cavallo, 2022: A cyclone-centered perspective on the drivers of asymmetric patterns in the atmosphere and sea ice during arctic cyclones. *Journal of Climate*, **35 (1)**, 73–89.

Cointe, R. and J.-L. Armand, 1987: Hydrodynamic impact analysis of a cylinder.

Collins III, C. O., W. E. Rogers, A. Marchenko, and A. V. Babanin, 2015: In situ measurements of an energetic wave event in the arctic marginal ice zone. *Geophysical Research Letters*, **42 (6)**, 1863–1870.

Comiso, J. C., 2012: Large decadal decline of the arctic multiyear ice cover. *Journal of Climate*, **25 (4)**, 1176–1193.

Crawford, A. D. and M. C. Serreze, 2016: Does the summer arctic frontal zone influence arctic ocean cyclone activity? *Journal of Climate*, **29 (13)**, 4977–4993.

Curcic, M. and B. K. Haus, 2020: Revised estimates of ocean surface drag in strong winds. *Geophysical Research Letters*, **47 (10)**, e2020GL087 647.

Curry, J., J. Schramm, and E. Ebert, 1993: Impact of clouds on the surface radiation balance of the arctic ocean. *Meteorology and Atmospheric Physics*, **51 (3-4)**, 197–217.

Dahlke, S., N. E. Hughes, P. M. Wagner, S. Gerland, T. Wawrzyniak, B. Ivanov, and M. Maturilli, 2020: The observed recent surface air temperature development across svalbard and concurring footprints in local sea ice cover. *International Journal of Climatology*, **40 (12)**, 5246–5265.

Danabasoglu, G., et al., 2020: The community earth system model version 2 (cesm2). *Journal of Advances in Modeling Earth Systems*, **12 (2)**, e2019MS001 916.

Day, J. J. and K. I. Hodges, 2018: Growing land-sea temperature contrast and the intensification of arctic cyclones. *Geophysical Research Letters*, **45 (8)**, 3673–3681.

Day, J. J., M. M. Holland, and K. I. Hodges, 2018: Seasonal differences in the response of arctic cyclones to climate change in cesm1. *Climate Dynamics*, **50 (9)**, 3885–3903.

Dempsey, J., R. Adamson, and S. Mulmule, 1999: Scale effects on the in-situ tensile strength and fracture of ice. part ii: First-year sea ice at resolute, nwt. *International journal of fracture*, **95 (1)**, 347–366.

DeRepentigny, P., A. Jahn, M. M. Holland, and A. Smith, 2020: Arctic sea ice in two configurations of the cesm2 during the 20th and 21st centuries. *Journal of Geophysical Research: Oceans*, **125 (9)**, e2020JC016 133.

Deser, C. and H. Teng, 2008: Evolution of arctic sea ice concentration trends and the role of atmospheric circulation forcing, 1979–2007. *Geophysical Research Letters*, **35 (2)**.

Deser, C., J. E. Walsh, and M. S. Timlin, 2000: Arctic sea ice variability in the context of recent atmospheric circulation trends. *Journal of Climate*, **13 (3)**, 617–633.

Ding, Q., et al., 2017: Influence of high-latitude atmospheric circulation changes on summertime arctic sea ice. *Nature Climate Change*, **7 (4)**, 289–295.

Ding, Q., et al., 2019: Fingerprints of internal drivers of arctic sea ice loss in observations and model simulations. *Nature Geoscience*, **12 (1)**, 28–33.

Dobrynin, M., J. Murawsky, and S. Yang, 2012: Evolution of the global wind wave climate in cmip5 experiments. *Geophysical Research Letters*, **39 (18)**.

Docquier, D. and T. Koenigk, 2021: Observation-based selection of climate models projects arctic ice-free summers around 2035. *Communications Earth & Environment*, **2 (1)**, 144.

Docquier, D., T. Koenigk, R. Fuentes-Franco, M. P. Karami, and Y. Ruprich-Robert, 2021: Impact of ocean heat transport on the arctic sea-ice decline: a model study with ec-earth3. *Climate Dynamics*, **56 (5)**, 1407–1432.

Durkalec, A., C. Furgal, M. W. Skinner, and T. Sheldon, 2015: Climate change influences on environment as a determinant of indigenous health: Relationships to place, sea ice, and health in an inuit community. *Social science & medicine*, **136**, 17–26.

DuVivier, A. K., M. M. Holland, J. E. Kay, S. Tilmes, A. Gettelman, and D. A. Bailey, 2020: Arctic and antarctic sea ice mean state in the community earth system model version 2 and the influence of atmospheric chemistry. *Journal of Geophysical Research: Oceans*, **125 (8)**, e2019JC015 934.

Dzerdzeevskii, B., 1945: Tsirkuliatsionnye skhemy v troposfere tsentral'noi arktiki. *Izdatel'svo Akad. Nauk*.

Eady, E. T., 1949: Long waves and cyclone waves. *Tellus*, **1 (3)**, 33–52.

Eicken, H., A. L. Lovecraft, and M. L. Druckenmiller, 2009: Sea-ice system services: A framework to help identify and meet information needs relevant for arctic observing networks. *ARCTIC*, **62 (2)**, 119–136.

Eliassen, A. and E. Kleinschmidt, 1957: Handbuch der physik. vol. 48. Springer-Verlag.

England, M., A. Jahn, and L. Polvani, 2019: Nonuniform contribution of internal variability to recent arctic sea ice loss. *Journal of Climate*, **32 (13)**, 4039–4053.

Farrell, B., 1985: Transient growth of damped baroclinic waves. *Journal of the atmospheric sciences*, **42 (24)**, 2718–2727.

Fetterer, F. K., W. N. Knowles, M. S. Meier, and A. K. Windnagel., 2017: *Sea Ice Index, Version 3*, boulder, Colorado USA. NSIDC: National Snow and Ice Data Center. Accessed: April 1, 2019.

Finocchio, P. M. and J. D. Doyle, 2021: Summer cyclones and their association with short-term sea ice variability in the pacific sector of the arctic. *Frontiers in Earth Science*, **9**, 738 497.

Finocchio, P. M., J. D. Doyle, and D. P. Stern, 2022: Accelerated sea ice loss from late summer cyclones in the new arctic. *Journal of Climate*, **35 (23)**, 7751–7769.

Finocchio, P. M., J. D. Doyle, D. P. Stern, and M. G. Fearon, 2020: Short-term impacts of arctic summer cyclones on sea ice extent in the marginal ice zone. *Geophysical Research Letters*, **47 (13)**, e2020GL088 338.

Gettelman, A., et al., 2019: The whole atmosphere community climate model version 6 (waccm6). *Journal of Geophysical Research: Atmospheres*, **124 (23)**, 12 380–12 403.

Graham, R. M., et al., 2019: Winter storms accelerate the demise of sea ice in the atlantic sector of the arctic ocean. *Scientific Reports*, **9 (1)**, 1–16.

Guest, P., P. O. G. Persson, S. Wang, M. Jordan, Y. Jin, B. Blomquist, and C. Fairall, 2018: Low-level baroclinic jets over the new arctic ocean. *Journal of Geophysical Research: Oceans*, **123 (6)**, 4074–4091.

Hakim, G. J., 2000: Climatology of coherent structures on the extratropical tropopause. *Monthly weather review*, **128 (2)**, 385–406.

Hayden, E. E. and L. W. O'Neill, 2024: Processes contributing to bering sea temperature variability in the late twentieth and early twenty-first century. *Journal of Climate*, **37 (1)**, 41–58.

Hemer, M. A., J. Katzfey, and C. E. Trenham, 2013: Global dynamical projections of surface ocean wave climate for a future high greenhouse gas emission scenario. *Ocean Modelling*, **70**, 221–245.

Hersbach, H., et al., 2019: Global reanalysis: goodbye era-interim, hello era5. 17–24, doi: 10.21957/vf291hehd7, URL `https://www.ecmwf.int/node/19027`.

Hersbach, H., et al., 2020: The era5 global reanalysis. *Quarterly Journal of the Royal Meteorological Society*, **146 (730)**, 1999–2049.

Hirdaris, S., et al., 2014: Loads for use in the design of ships and offshore structures. *Ocean Engineering*, **78**, 131–174, doi:https://doi.org/10.1016/j.oceaneng.2013.09.012, URL `https://www.sciencedirect.com/science/article/pii/S0029801813003557`.

Holt, B. and S. Martin, 2001: The effect of a storm on the 1992 summer sea ice cover of the beaufort, chukchi, and east siberian seas. *Journal of Geophysical Research: Oceans*, **106 (C1)**, 1017–1032.

Hörner, T., R. Stein, and K. Fahl, 2017: Evidence for holocene centennial variability in sea ice cover based on ip25 biomarker reconstruction in the southern kara sea (arctic ocean). *Geo-Marine Letters*, **37 (5)**, 515–526.

Hoskins, B. J., M. McIntyre, and A. W. Robertson, 1985: On the use and significance of isentropic potential vorticity maps. *Quarterly Journal of the Royal Meteorological Society*, **111 (470)**, 877–946.

Hu, A., C. Rooth, R. Bleck, and C. Deser, 2002: Nao influence on sea ice extent in the eurasian coastal region. *Geophysical Research Letters*, **29 (22)**, 10–1.

Huang, J., et al., 2017: Recently amplified arctic warming has contributed to a continual global warming trend. *Nature climate change*, **7 (12)**, 875–879.

Hwang, B. and Y. Wang, 2022: Multi-scale satellite observations of arctic sea ice: new insight into the life cycle of the floe size distribution. *Philosophical Transactions of the Royal Society A*, **380 (2235)**, 20210 259.

Inoue, J. and M. E. Hori, 2011: Arctic cyclogenesis at the marginal ice zone: A contributory mechanism for the temperature amplification? *Geophysical Research Letters*, **38 (12)**.

Intrieri, J., C. Fairall, M. Shupe, P. Persson, E. Andreas, P. Guest, and R. Moritz, 2002: An annual cycle of arctic surface cloud forcing at sheba. *Journal of Geophysical Research: Oceans*, **107 (C10)**.

Japan Meteorological Agency, Japan, 2013: Jra-55: Japanese 55-year reanalysis, monthly means and variances. Research Data Archive at the National Center for Atmospheric Research, Computational and Information Systems Laboratory, Boulder CO, URL `https://doi.org/10.5065/D60G3H5B`, URL `https://doi.org/10.5065/D60G3H5B`.

Karwat, A., C. L. Franzke, J. G. Pinto, S.-S. Lee, and R. Blender, 2024: Northern hemisphere extratropical cyclone clustering in era5 reanalysis and the cesm2 large ensemble. *Journal of Climate*, **37 (4)**, 1347–1365.

Kay, J. E., et al., 2015: The community earth system model (cesm) large ensemble project: A community resource for studying climate change in the presence of internal climate variability. *Bulletin of the American Meteorological Society*, **96 (8)**, 1333–1349.

Kay, J. E., et al., 2022: Less surface sea ice melt in the cesm2 improves arctic sea ice simulation with minimal non-polar climate impacts. *Journal of Advances in Modeling Earth Systems*, **14 (4)**, e2021MS002 679.

Keen, A., et al., 2021: An inter-comparison of the mass budget of the arctic sea ice in cmip6 models. *The Cryosphere*, **15 (2)**, 951–982.

Knol, M., P. Arbo, P. Duske, S. Gerland, M. Lamers, O. Pavlova, A. D. Sivle, and S. Tronstad, 2018: Making the arctic predictable: The changing information infrastructure of arctic weather and sea ice services. *Polar Geography*, **41 (4)**, 279–293.

Knudsen, E. M., Y. J. Orsolini, T. Furevik, and K. I. Hodges, 2015: Observed anomalous atmospheric patterns in summers of unusual arctic sea ice melt. *Journal of Geophysical Research: Atmospheres*, **120 (7)**, 2595–2611.

Kolling, H. M., R. Stein, K. Fahl, K. Perner, and M. Moros, 2018: New insights into sea ice changes over the past 2.2 kyr in disko bugt, west greenland. *arktos*, **4 (1)**, 1–20.

Kosaka, Y. and S.-P. Xie, 2013: Recent global-warming hiatus tied to equatorial pacific surface cooling. *Nature*, **501 (7467)**, 403–407.

Kriegsmann, A. and B. Brümmer, 2014: Cyclone impact on sea ice in the central arctic ocean: a statistical study. *The Cryosphere*, **8 (1)**, 303.

Kwok, R., 2000: Recent changes in arctic ocean sea ice motion associated with the north atlantic oscillation. *Geophysical Research Letters*, **27 (6)**, 775–778.

Kwok, R., 2018: Arctic sea ice thickness, volume, and multiyear ice coverage: losses and coupled variability (1958–2018). *Environmental Research Letters*, **13 (10)**, 105 005.

Kwok, R. and G. Cunningham, 2010: Contribution of melt in the beaufort sea to the decline in arctic multiyear sea ice coverage: 1993–2009. *Geophysical Research Letters*, **37 (20)**.

Kwok, R. and D. A. Rothrock, 1999: Variability of fram strait ice flux and north atlantic oscillation. *Journal of Geophysical Research: Oceans*, **104 (C3)**, 5177–5189.

Lammert, A., B. Brümmer, and L. Kaleschke, 2009: Observation of cyclone-induced inertial sea-ice oscillation in fram strait. *Geophysical Research Letters*, **36 (10)**.

Lawrence, D. M., et al., 2019: The community land model version 5: Description of new features, benchmarking, and impact of forcing uncertainty. *Journal of Advances in Modeling Earth Systems*, **11 (12)**, 4245–4287.

Lind, S., R. B. Ingvaldsen, and T. Furevik, 2018: Arctic warming hotspot in the northern barents sea linked to declining sea-ice import. *Nature Climate Change*, **8 (7)**, 634.

Lindsay, R. and A. Schweiger, 2015: Arctic sea ice thickness loss determined using subsurface, aircraft, and satellite observations. *The Cryosphere*, **9 (1)**, 269–283.

Lindsey, R., 2009: Climate variability: Arctic oscillation. URL `https://www.climate.gov/news-features/understanding-climate/climate-variability-arctic-oscillation#:~:text=The%20AOs%20positive%20phase%20is,northern%20Pacific%20and%20Atlantic%20Oceans.`, URL `https://www.climate.gov/news-features/understanding-climate/climate-variability-arctic-oscillation#:~:text=The%20AOs%20positive%20phase%20is,northern%20Pacific%20and%20Atlantic%20Oceans.`

Lindsey, R. and L. Dahlman, 2009: Climate variability: North atlantic oscillation. URL `https://www.climate.gov/news-features/understanding-climate/climate-variability-north-atlantic-oscillation`, URL `https://www.climate.gov/news-features/understanding-climate/climate-variability-north-atlantic-oscillation`.

Lovecraft, A. L., C. Meek, and H. Eicken, 2013: Connecting scientific observations to stakeholder needs in sea ice social–environmental systems: the institutional geography of northern alaska. *Polar Geography*, **36 (1-2)**, 105–125.

Luo, B., D. Luo, L. Wu, L. Zhong, and I. Simmonds, 2017: Atmospheric circulation patterns which promote winter arctic sea ice decline. *Environmental Research Letters*, **12 (5)**, 054 017.

Mahoney, A., 2018: Landfast sea ice in a changing arctic. *Arctic report card*, **99**.

Markus, T., J. C. Stroeve, and J. Miller, 2009: Recent changes in arctic sea ice melt onset, freezeup, and melt season length. *Journal of Geophysical Research: Oceans*, **114 (C12)**.

Meredith, M., et al., 2019: Polar regions. *IPCC Special Report on the Ocean and Cryosphere in a Changing Climate*.

Mesquita, M. d. S., D. E. Atkinson, I. Simmonds, K. Keay, and J. Gottschalck, 2009: New perspectives on the synoptic development of the severe october 1992 nome storm. *Geophysical Research Letters*, **36 (13)**.

Mesquita, M. S., D. E. Atkinson, and K. I. Hodges, 2010: Characteristics and variability of storm tracks in the north pacific, bering sea, and alaska. *Journal of Climate*, **23 (2)**, 294–311.

Meylan, M. H., L. G. Bennetts, J. Mosig, W. Rogers, M. Doble, and M. A. Peter, 2018: Dispersion relations, power laws, and energy loss for waves in the marginal ice zone. *Journal of Geophysical Research: Oceans*, **123 (5)**, 3322–3335.

Msadek, R., G. Vecchi, M. Winton, and R. Gudgel, 2014: Importance of initial conditions in seasonal predictions of arctic sea ice extent. *Geophysical Research Letters*, **41 (14)**, 5208–5215.

Neu, U., et al., 2013: Imilast: A community effort to intercompare extratropical cyclone detection and tracking algorithms. *Bulletin of the American Meteorological Society*, **94 (4)**, 529–547.

Nicolaus, M., et al., 2022: Overview of the mosaic expedition: Snow and sea ice. *Elem Sci Anth*, **10 (1)**, 000 046.

Nishii, K., H. Nakamura, and Y. J. Orsolini, 2015: Arctic summer storm track in cmip3/5 climate models. *Climate Dynamics*, **44 (5-6)**, 1311–1327.

North, G. R., T. L. Bell, R. F. Cahalan, and F. J. Moeng, 1982: Sampling errors in the estimation of empirical orthogonal functions. *Monthly weather review*, **110 (7)**, 699–706.

Notz, D., 2014: Sea-ice extent and its trend provide limited metrics of model performance. *The Cryosphere*, **8 (1)**, 229–243.

Notz, D. and S. Community, 2020: Arctic sea ice in cmip6. *Geophysical Research Letters*, **47 (10)**, e2019GL086 749.

Notz, D. and J. Stroeve, 2016: Observed arctic sea-ice loss directly follows anthropogenic co2 emission. *Science*, **354 (6313)**, 747–750.

Notz, D. and J. Stroeve, 2018: The trajectory towards a seasonally ice-free arctic ocean. *Current Climate Change Reports*, **4 (4)**, 407–416.

Ogi, M., I. G. Rigor, M. G. McPhee, and J. M. Wallace, 2008: Summer retreat of arctic sea ice: Role of summer winds. *Geophysical Research Letters*, **35 (24)**.

Ogi, M. and J. M. Wallace, 2007: Summer minimum arctic sea ice extent and the associated summer atmospheric circulation. *Geophysical Research Letters*, **34 (12)**.

Ogi, M., K. Yamazaki, and J. M. Wallace, 2010: Influence of winter and summer surface wind anomalies on summer arctic sea ice extent. *Geophysical Research Letters*, **37 (7)**.

Olonscheck, D., T. Mauritsen, and D. Notz, 2019: Arctic sea-ice variability is primarily driven by atmospheric temperature fluctuations. *Nature Geoscience*, **12 (6)**, 430–434.

Overeem, I., R. S. Anderson, C. W. Wobus, G. D. Clow, F. E. Urban, and N. Matell, 2011: Sea ice loss enhances wave action at the arctic coast. *Geophysical Research Letters*, **38 (17)**.

Overland, J. E. and M. Wang, 2010: Large-scale atmospheric circulation changes are associated with the recent loss of arctic sea ice. *Tellus A: Dynamic Meteorology and Oceanography*, **62 (1)**, 1–9.

Park, H., E. Watanabe, Y. Kim, I. Polyakov, K. Oshima, X. Zhang, J. S. Kimball, and D. Yang, 2020: Increasing riverine heat influx triggers arctic sea ice decline and oceanic and atmospheric warming. *Science advances*, **6 (45)**, eabc4699.

Parkinson, C. L. and J. C. Comiso, 2013: On the 2012 record low arctic sea ice cover: Combined impact of preconditioning and an august storm. *Geophysical Research Letters*, **40 (7)**, 1356–1361.

Peng, G. and W. N. Meier, 2018: Temporal and regional variability of arctic sea-ice coverage from satellite data. *Annals of Glaciology*, **59 (76pt2)**, 191–200.

Perovich, D. K., J. A. Richter-Menge, K. F. Jones, and B. Light, 2008: Sunlight, water, and ice: Extreme arctic sea ice melt during the summer of 2007. *Geophysical Research Letters*, **35 (11)**.

Phillips, A. S., C. Deser, and J. Fasullo, 2014: Evaluating modes of variability in climate models. *Eos, Transactions American Geophysical Union*, **95 (49)**, 453–455.

Pierrehumbert, R. and K. Swanson, 1995: Baroclinic instability. *Annual review of fluid mechanics*, **27 (1)**, 419–467.

Priestley, M. D., D. Ackerley, J. L. Catto, K. I. Hodges, R. E. McDonald, and R. W. Lee, 2020: An overview of the extratropical storm tracks in cmip6 historical simulations. *Journal of Climate*, **33 (15)**, 6315–6343.

Reed, R. J. and B. A. Kunkel, 1960: The arctic circulation in summer. *Journal of Meteorology*, **17 (5)**, 489–506.

Richter, J. H., et al., 2022: Subseasonal earth system prediction with cesm2. *Weather and Forecasting*, **37 (6)**, 797–815.

Rigor, I. G., J. M. Wallace, and R. L. Colony, 2002: Response of sea ice to the arctic oscillation. *Journal of Climate*, **15 (18)**, 2648–2663.

Roberts, M. J., et al., 2020: Sensitivity of the atlantic meridional overturning circulation to model resolution in cmip6 highresmip simulations and implications for future changes. *Journal of Advances in Modeling Earth Systems*, **12 (8)**, e2019MS002 014.

Rodgers, K. B., et al., 2021: Ubiquity of human-induced changes in climate variability. *Earth System Dynamics*, **12 (4)**, 1393–1411.

Rosenblum, E. and I. Eisenman, 2017: Sea ice trends in climate models only accurate in runs with biased global warming. *Journal of Climate*, **30 (16)**, 6265–6278.

Rudeva, I., S. K. Gulev, I. Simmonds, and N. Tilinina, 2014: The sensitivity of characteristics of cyclone activity to identification procedures in tracking algorithms. *Tellus A: Dynamic Meteorology and Oceanography*, **66 (1)**, 24 961.

Saha, S., et al., 2014: The ncep climate forecast system version 2. *Journal of climate*, **27 (6)**, 2185–2208.

Sallila, H., S. L. Farrell, J. McCurry, and E. Rinne, 2019: Assessment of contemporary satellite sea ice thickness products for arctic sea ice. *The Cryosphere*, **13 (4)**, 1187–1213.

Sarpkaya, T., 1977: In-line and transverse forces on cylinders in oscillatory flow at high reynolds numbers. *Journal of ship Research*, **21 (04)**, 200–216.

Schreiber, E. A. and M. C. Serreze, 2020: Impacts of synoptic-scale cyclones on arctic sea-ice concentration: A systematic analysis. *Annals of Glaciology*, **61 (82)**, 139–153.

Screen, J. A., I. Simmonds, and K. Keay, 2011: Dramatic interannual changes of perennial arctic sea ice linked to abnormal summer storm activity. *Journal of Geophysical Research: Atmospheres*, **116 (D15)**.

Sepp, M. and J. Jaagus, 2011: Changes in the activity and tracks of arctic cyclones. *Climatic Change*, **105 (3-4)**, 577–595.

Serreze, M., J. Box, R. Barry, and J. Walsh, 1993: Characteristics of arctic synoptic activity, 1952–1989. *Meteorology and Atmospheric Physics*, **51 (3-4)**, 147–164.

Serreze, M. C., 1995: Climatological aspects of cyclone development and decay in the arctic. *Atmosphere-Ocean*, **33 (1)**, 1–23, doi:10.1080/07055900.1995.9649522, URL `https://doi.org/10.1080/07055900.1995.9649522`.

Serreze, M. C. and A. P. Barrett, 2008: The summer cyclone maximum over the central arctic ocean. *Journal of Climate*, **21 (5)**, 1048–1065.

Serreze, M. C., F. Carse, R. G. Barry, and J. C. Rogers, 1997: Icelandic low cyclone activity: Climatological features, linkages with the nao, and relationships with recent changes in the northern hemisphere circulation. *Journal of Climate*, **10 (3)**, 453–464.

Serreze, M. C., A. H. Lynch, and M. P. Clark, 2001: The arctic frontal zone as seen in the ncep–ncar reanalysis. *Journal of Climate*, **14 (7)**, 1550–1567.

Simmonds, I., C. Burke, and K. Keay, 2008: Arctic climate change as manifest in cyclone behavior. *Journal of Climate*, **21 (22)**, 5777–5796.

Simmonds, I. and K. Keay, 2009: Extraordinary september arctic sea ice reductions and their relationships with storm behavior over 1979–2008. *Geophysical Research Letters*, **36 (19)**.

Simmonds, I. and I. Rudeva, 2012: The great arctic cyclone of august 2012. *Geophysical research letters*, **39 (23)**.

Solomon, S., D. Qin, M. Manning, K. Averyt, and M. Marquis, 2007: *Climate change 2007-the physical science basis: Working group I contribution to the fourth assessment report of the IPCC*, Vol. 4. Cambridge university press.

Song, J.-N., G. Fu, Y. Xu, Z.-Y. Han, Q.-Z. Sun, and H. Wang, 2021: Assessment of the capability of cmip6 global climate models to simulate arctic cyclones. *Advances in Climate Change Research*, **12 (5)**, 660–676.

Squire, V., 2007: Of ocean waves and sea-ice revisited. *Cold Regions Science and Technology*, **49 (2)**, 110–133.

Squire, V. A., 2020: Ocean wave interactions with sea ice: A reappraisal. *Annual Review of Fluid Mechanics*, **52**, 37–60.

Steele, M., W. Ermold, and J. Zhang, 2008: Arctic ocean surface warming trends over the past 100 years. *Geophysical Research Letters*, **35 (2)**.

Stephenson, S. R. and L. C. Smith, 2015: Influence of climate model variability on projected arctic shipping futures. *Earth's Future*, **3 (11)**, 331–343.

Stephenson, S. R., L. C. Smith, L. W. Brigham, and J. A. Agnew, 2013: Projected 21st-century changes to arctic marine access. *Climatic Change*, **118 (3-4)**, 885–899.

Stopa, J. E., F. Ardhuin, and F. Girard-Ardhuin, 2016: Wave climate in the arctic 1992–2014: Seasonality and trends. *The Cryosphere*, **10 (4)**, 1605–1629.

Stroeve, J., E. Blanchard-Wrigglesworth, V. Guemas, S. Howell, F. Massonnet, and S. Tietsche, 2015: Improving predictions of arctic sea ice extent. *Earth and Space Science*, **96**, 11.

Stroeve, J., A. Frei, J. McCREIGHT, and D. Ghatak, 2008: Arctic sea-ice variability revisited. *Annals of Glaciology*, **48**, 71–81.

Stroeve, J., M. M. Holland, W. Meier, T. Scambos, and M. Serreze, 2007: Arctic sea ice decline: Faster than forecast. *Geophysical research letters*, **34 (9)**.

Stroeve, J. and D. Notz, 2018: Changing state of arctic sea ice across all seasons. *Environmental Research Letters*, **13 (10)**, 103 001.

Stroeve, J. C., M. C. Serreze, M. M. Holland, J. E. Kay, J. Malanik, and A. P. Barrett, 2012: The arctic's rapidly shrinking sea ice cover: a research synthesis. *Climatic Change*, **110 (3-4)**, 1005–1027.

Szapiro, N. and S. Cavallo, 2018: Tpvtrack v1. 0: A watershed segmentation and overlap correspondence method for tracking tropopause polar vortices. *Geoscientific Model Development*, **11 (12)**, 5173–5187.

Tanaka, H., A. Yamagami, and S. Takahashi, 2012: The structure and behavior of the arctic cyclone in summer analyzed by the jra-25/jcdas data. *Polar Science*, **6 (1)**, 55–69.

Tao, W., J. Zhang, and X. Zhang, 2017: The role of stratosphere vortex downward intrusion in a long-lasting late-summer arctic storm. *Quarterly Journal of the Royal Meteorological Society*, **143 (705)**, 1953–1966.

Thomson, J. and W. E. Rogers, 2014: Swell and sea in the emerging arctic ocean. *Geophysical Research Letters*, **41 (9)**, 3136–3140.

Thorndike, A. S., D. A. Rothrock, G. A. Maykut, and R. Colony, 1975: The thickness distribution of sea ice. *Journal of Geophysical Research*, **80 (33)**, 4501–4513.

Tilling, R., N. Kurtz, M. Bagnardi, A. Petty, and R. Kwok, 2020: Detection of melt ponds on arctic summer sea ice from icesat-2. *Geophysical Research Letters*, **47 (23)**, e2020GL090 644.

Valkonen, E., J. Cassano, and E. Cassano, 2021: Arctic cyclones and their interactions with the declining sea ice: A recent climatology. *Journal of Geophysical Research: Atmospheres*, **126 (12)**, e2020JD034 366.

Van den Dool, H., S. Saha, and A. Johansson, 2000: Empirical orthogonal teleconnections. *Journal of Climate*, **13 (8)**, 1421–1435.

Wadhams, P., 1981: The ice cover in the greenland and norwegian seas. *Reviews of geophysics*, **19 (3)**, 345–393.

Walker, G. T., 1923: Correlation in seasonal variation of weather. viii: A preliminary study of world weather. *Memoirs of India Meteorological Department*, **24**, 75–131.

Wang, M. and J. E. Overland, 2009: A sea ice free summer arctic within 30 years? *Geophysical research letters*, **36 (7)**.

Wang, X., J. Liu, and H. Liu, 2024: Seasonal variability of arctic mid-level clouds and the relationships with sea ice from 2003 to 2022: A satellite perspective. *Remote Sensing*, **16 (1)**, 202.

Watanabe, E., J. Wang, A. Sumi, and H. Hasumi, 2006: Arctic dipole anomaly and its contribution to sea ice export from the arctic ocean in the 20th century. *Geophysical research letters*, **33 (23)**.

Wei, L., T. Qin, P. Uotila, T. Vihma, B. Cheng, et al., 2016: Analyses of summer cyclone activities over the arctic ocean. *The 26th International Ocean and Polar Engineering Conference*, International Society of Offshore and Polar Engineers.

Xie, Z., Y. Ha, Y. Zhu, Y. Hu, and Z. Zhong, 2024: Impact of arctic sea ice on the boreal summer intraseasonal oscillation. *Climate Dynamics*, 1–19.

Yamazaki, A., J. Inoue, K. Dethloff, M. Maturilli, and G. König-Langlo, 2015: Impact of radiosonde observations on forecasting summertime arctic cyclone formation. *Journal of Geophysical Research: Atmospheres*, **120 (8)**, 3249–3273.

Zhang, J., R. Lindsay, A. Schweiger, and M. Steele, 2013: The impact of an intense summer cyclone on 2012 arctic sea ice retreat. *Geophysical Research Letters*, **40 (4)**, 720–726.

Zhang, X., J. E. Walsh, J. Zhang, U. S. Bhatt, and M. Ikeda, 2004: Climatology and interannual variability of arctic cyclone activity: 1948–2002. *Journal of climate*, **17 (12)**, 2300–2317.